


Doctoral Dissertation
Doctoral Program in Electrical, Electronics and Communications Engineering
(34.th cycle)

Theory and modelization of Quantum Cascade Laser dynamics: comb formation, field structures and feedback-based imaging

Carlo Silvestri
* * * * * *

Supervisors
Prof. Mariangela Gioannini
Prof. Massimo Brambilla
Dr. Lorenzo Columbo

Politecnico di Torino

I hereby declare that, the contents and organisation of this dissertation constitute my own original work and does not compromise in any way the rights of third parties, including those relating to the security of personal data.

. . . . . .

Carlo Silvestri

Turin,

Summary

This work concerns about the study of the Quantum Cascade Lasers' dynamics from theoretical and numerical point of view, by exploring different aspects of this vast field of study.
Firstly, the self-generation of optical frequency combs by exploiting these devices in the Fabry-Perot (FP) configuration has been studied by introducing the Effective Semiconductor Maxwell-Bloch Equations (ESMBEs), a model which encompasses the main features of semiconductors materials and includes in the case of FP cavity the Spatial-Hole Burning (SHB). The simulation study based on the integration of the ESMBEs has allowed the reproduction of relevant experimental achievements and the highlight of the role of some parameters such as the linewidth enhancement factor. Furthermore, this model has been retrieved for the case of ring Quantum Cascade Laser, and also in this case a simulation study has been performed.
The case of ring QCL have also been studied by introducing a reduced model based on a single master equation. This model, which is valid in the hypotheses of fast carriers and near threshold operation, presents a shorter simulation time, and showed an agreement with the ESMBEs results also for values of the current relevantly above the laser threshold.
The ring QCL with an optical injected field has also been considered and numerically studied, achieving the reproduction of experimentally found regimes such as temporal solitons and Turing rolls.
The last part of the work is dedicated to the study of a Terahertz (THZ)- QCL in presence of optical feedback, in a self-mixing interferometry setup which is combined with a probing-type microscopy technique, in order to produce a system for the nano-imaging of resonant materials, called Self-Detection scattering type near field optical microscopy (SD s-SNOM). A theoretical study based on the Lang-Kobayashi Equations and a simulation analysis of this setup have been performed in order to explore the possibility to retrieve the dielectric properties of materials with phonon resonances in the THZ region with a resolution far beyond the diffraction limit.

Acknowledgements

At the end of this particularly hard journey, I would like to thank the people that helped me to complete it. In particular, I want to thank with big gratitude Dr. Lorenzo Columbo, which followed me during these three years and from which I learned so many things. Special thanks to prof. Massimo Brambilla, whose help and approach was indispensable for me to achieve the results that I obtained during my doctoral period. I also want to thank prof. Mariangela Gioannini, who gave me the possibility to start this fascinating journey and helped me to develop an engineering approach.
I would like to thank also prof. Paolo Bardella, for the interesting conversations and all his help during these years, and my friend and colleague Amin, for the clever support and his precious kindness.
I thank my parents for the continuous support that I received from them during the difficult moments of my PhD.
In the end, I want to mention my girlfriend Sevgim, for the amazing love that she showed me, that was fundamental for me to complete this work with happiness and peace. Seni çok seviyorum prensesim.

Contents

List of Figures

Chapter 1

Introduction

The aim of this chapter is to introduce general aspects of background knowledge that will be largely used in the following part of the work. Firstly, in section 1.1 we review the main characteristics of Quantum Cascade Laser (QCL), a semiconductor laser to whom this work is dedicated. We will consider its cavity, the electronics transitions and the materials that are exploited to realize this device.
Furthermore, in section 1.2 the topic of Optical Frequency Combs (OFC) will be treated. The dynamics of these emission regimes and its self-generation by QCLs we will treat in detail in Chapters 2-3.
The last section is dedicated to a brief review of the Self-Detection scattering type near-field optical microscopy (SD s-SNOM), a nanoscopy technique exploiting QCLs in the region of Terahertz for imaging and material analysis, which is characterized by the absence of a detector: the laser itself is used as detector and therefore the theoretical study related to this part concerns the dynamics of QCLs in presence of optical feedback.

1.1 Quantum Cascade Lasers

Semiconductor lasers are solid state lasers which exploit as active medium a semiconductor material. Few semiconductors (for example PbSSe and PbSnSe) can give lasing in the mid-Infrared (mid-IR) spectral region ($\lambda > 2\mu$m), and this lack is related to the relevance of the Auger effect in this spectral range. However, these devices based on Pb alloys present some consistent disadvantages. In fact their typical low output power (<0.1mW), the operation temperature <100K and their relevant cost (tens of thousands dollars) make them a problematic solution for the emission in the mid-IR.
Conventional laser diodes are based on electronic transitions between conduction band and valence band of the semiconductor, therefore they exploit interband transitions. This implies one fundamental limit: the energy of the emitted photons must

correspond to the energy gap of the material or energy separation between the confined states of the Quantum Well in conduction band and valence band.
QCLs differ from conventional lasers because their operation is not due to interband, but to intraband electronic transitions, i.e. transitions between confined states of the quantum wells in the conduction band only, named *subbands*. In Fig.

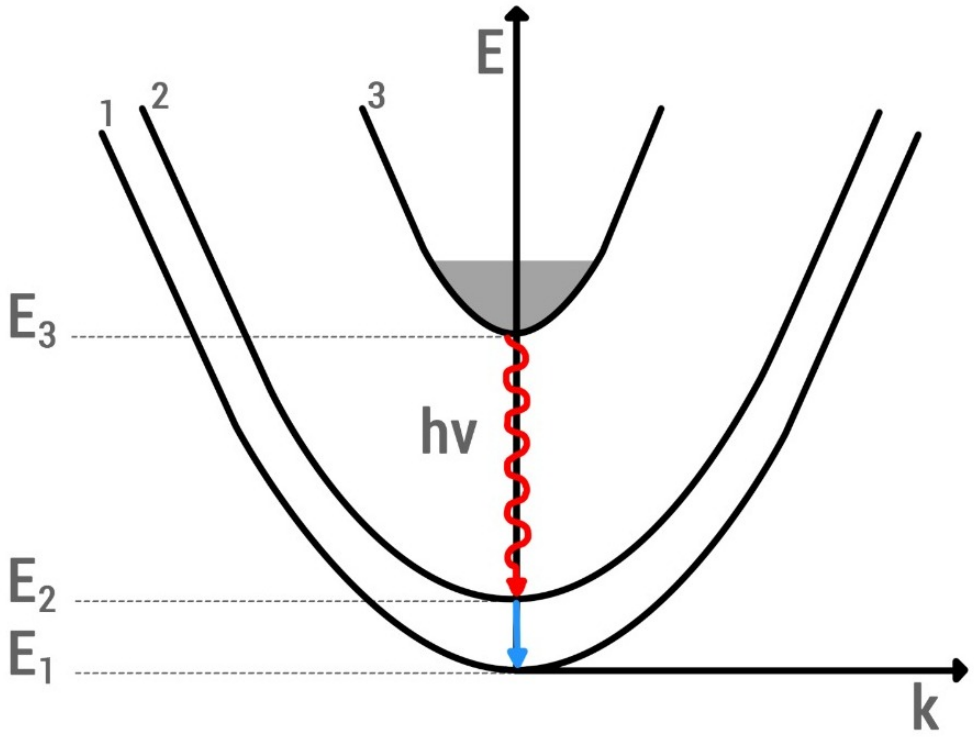

Figure 1.1: Energy as a function of the the wavenumber k for a typical set of confined states in the conduction band, characterizing a QCL. E_n are the values of the energy corresponding to the bottom of the n-th subband, for n=1,2,3; $\hbar\nu$ is the energy of the photon generated in the electronic transition between the state 3 and the state 2.

1.1 a set of subbands typical for a QCL is shown. In this scheme the energy as a function of the wavenumber k is represented and this scheme consists of three subbands, named with the integer numbers n=1,2,3 and whose lowest value of the energy is E_n. All these confined states occur in the conduction band, therefore the transitions between these states do not involve holes but only electrons. For this reason QCL is defined as a unipolar device. In Fig. 1.1 we schematize an electronic transition between the subbands 3 and 2, with the emission of a photon with energy $\hbar\nu$ (red arrow) corresponding to $\Delta E_{32}=E_3-E_2$. Conversely, the transition between the states 2 and 1 (blue curve) does not involve the emission of a photon but it

is due to a scattering process between electron and phonon. These processes are necessary in order to empty the subband 2 and achieve the population inversion between the states 3 and 2, necessary for the lasing. They will be analized more in the detail in the following.
In order to obtain the scheme with subbands it is necessary to have an active medium composed by several stages, each of them made of an heterostructure. An

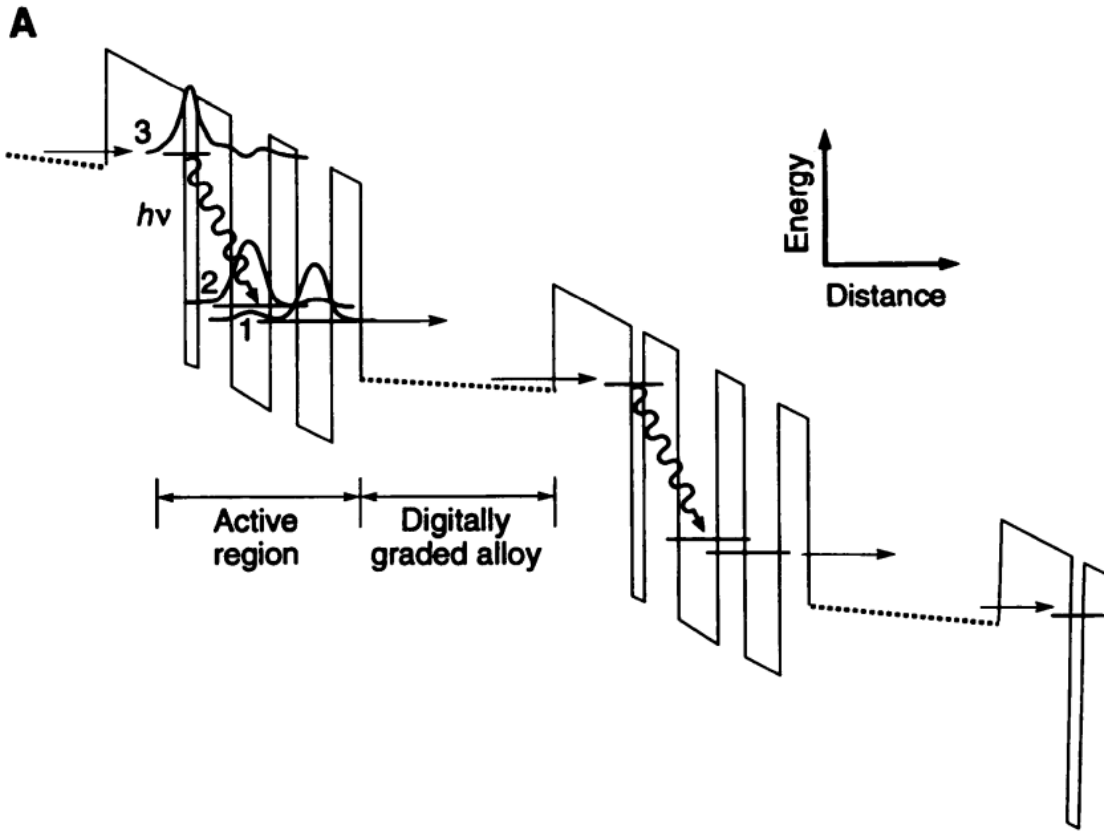

Figure 1.2: Conduction band energy diagram of a portion of section of a QCL, composed by an injector and an active region. Reproduced from [18].

example of a conduction band energy diagram of a part of a QCL is shown in Fig. 1.2. In this scheme, which is reproduced from [18] and corresponds to the first QCL realized in 1994, two main regions are underlined: an active region where we have the formation of the subbands, represented also in the figure with the numbers 1,2 and 3, and the adjacent region which is named injector. In the active region electronic transition occurs (from 3 to 2) and also the electron in 2 is rapidly transferred to the state 1 with the emission of a phonon, accessing then the following injection region via resonant tunneling process with some efficiency [18]. In order to create the quantum confinement and have therefore the subbands, each layer of the

quantum wells has a thickness of few nanometers. This is a cascading scheme which is replied for tens of stages, typically between 25 and 50. These heterostructures are built by exploiting specific techniques. The most important and used one is the Molecular Beam Epitaxy (MBE), which allows of the deposition of a sequence of extra-thin layers of considered materials.
In this way the transition energies are fully controlled by the quantum confinement, so that it is possible to engineer a structure which will allow emission at a given frequency, i.e. the frequency can be chosen via layers' thickness control. For this reason QCLs can emit in frequency ranges that normally are not achievable with other types of semiconductor lasers, as the mid-IR and the THz ranges.
Furthermore, they can be exploited in several types of different applications, such as free space communication [67], [66], [41], [15], material and molecular analysis and spectroscopy [19], [14], interferometry [22], metrology [58] and nonlinear optics [75], in both mid-IR and THz regions.
In the following part of this chapter we will review in more detail some peculiar characteristics of QCLs that we mentioned in this introductory part about this class of semiconductor lasers.

1.1.1 Laser cavity and electronic transitions in QCL

Let us consider again the scheme with three subbands shown in Fig. 1.1. We remind that only electrons are involved in the transitions between these confined states, since the subbands are created in the conduction band. This implies that recombination phenomena involving holes, as Auger effect, are not present in the operation of a QCL. Furthermore, the presence of defects in the active medium of the laser, which are responsible of recombination processes between holes and electrons, does not influence the efficiency of the laser. For this reason QCLs have a cavity length generally greater than conventional laser diodes (typically few millimeters).

A representation of a QCL cavity is shown in Fig.1.3, where all the components are named. The active region is made of the sequence of quantum wells, organized in injector-emitter stages. The optical confinement is achieved through an etched ridge (lateral confinement) and dielectric layers (vertical confinement).
Let us focus now on the phenomena involving electrons occurring in each unit of the active region of the QCL, referring to the confinement states relation dispersion shown in Fig. 1.1. The electronic transitions from the subband 3 to 2 and from 2 to 1 can be accompanied by the emission of a longitudinal optical (LO) phonon, with different relaxation time: typically few picoseconds in the first case and few tenths of picosecond in the second [18]. This enables a fast emptying of the state 2, and therefore the achievement of the population inversion. Typically the energy difference between the states 2 and 1 ΔE_{21} is chosen to correspond to the typical value of the energy of LO phonons in the considered material (few tens of meV).

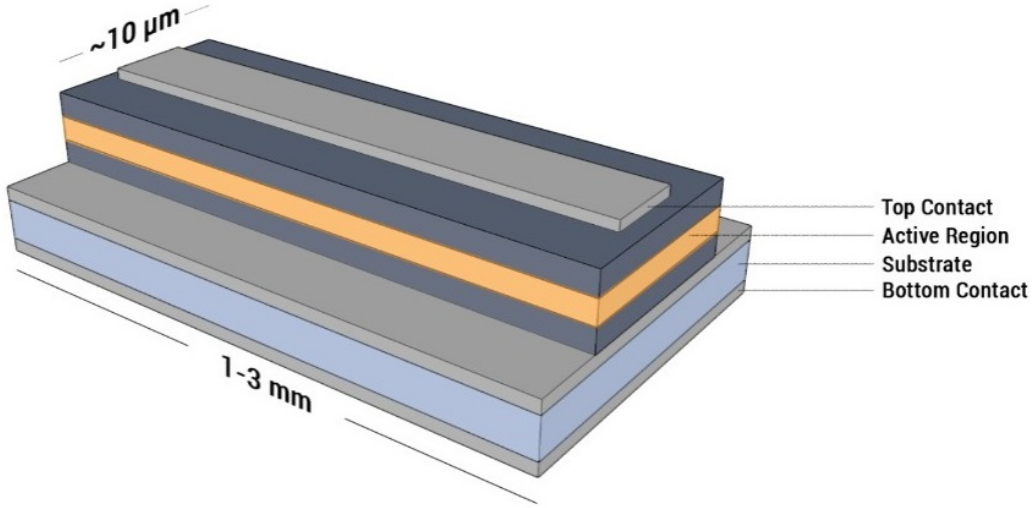

Figure 1.3: Schematic representation of a QCL cavity.

1.1.2 Materials

The choice of the material for building the heterostructure of a QCL is extremely relevant in order to select the energies of the transitions and therefore the energy of the emitted photon and the efficiency of the scattering processes. For this reason in the engineering process of a QCL active region some factors are considered. First of all the Quantum Well depth is a relevant factor in the material choice. In fact large conduction band offset is necessary for good confinement of electrons in upper laser level (state 3 in Fig. 1.1), in order to avoid for example electron escape due to thermal process or tunneling in presence of high applied fields, which can effect the efficiency of the device. The second parameter which is relevant in the choice of the material is the effective mass of the electrons. In fact from Quantum Mechanics theory it is possible to prove that the energy the intersubband transitions depends on the effective mass, such as the intersubband dipole matrix element, which is greater as the effective mass is lower.
The QCL heterostructure systems are based on III-V group semiconductors, mainly on GaAs-AlGaAs or GaAs-AlAs quantum wells with substrate made of GaAs, InGaAs-AlInAs or InGaAs-AlAsSb quantum wells with InP substrates, InAs-AlSb with InP or GaSb substrates. This last combination is very convenient since it presents a very large energy offset and low effective mass of electron, but it has the disadvantage that the exact position of lateral minima in the conduction band is unknown, factor that can reduce the efficiency of the laser device.

1.1.3 Single-mode QCL and linewidth enhancement factor

The possibility to have the emission frequency in the mid-IR and in the THz, and therefore a vast range of tunability, makes this class of devices very appealing and large studied in both these spectral ranges.
The CW operation of QCL in mid-IR at room temperature was first achieved in [5], with emission power is in mW range. This has enabled the possibility to improve a large class of applications, specifically in the area of sensing, spectroscopy and optical communication. The improvement in the design of QCLs has brought to enhance the performances, towards the Watt power level, and wall plug-efficiency of 21% in CW operation [77].
Furthermore, QCLs present interesting quantum properties, whose investigation concerns several characteristics of these devices. An example of fundamental and intrinsic quantum fingerprint of the device is related to its linewidth.
In 1982, 20 years after the invention of diode lasers, a definitive formalization of the theory about their linewidth has been proposed, with a modification of the Schawlow-Townes (ST) equation by introducing the linewidth enhancement factor (LEF), also called α factor [26]. The α factor correctly reproduces the broadening of the linewidth interesting semiconductor lasers, which occurs because of fluctuations of the density of electrons, which imply in turn fluctuations of the refractive index, and it is correlated to the curvature of the conduction and valence band.
In 2007 a theoretical work based on a set of rate equations for a three-level system has proposed a specialized version of the ST equation for a QCL [83]. In the equation for QCL based on this model, the emission intrinsic linewidth is expressed by:

$$\delta\nu = \frac{\gamma\beta_{eff}}{4\pi(1-\epsilon)}\left[\frac{1}{I_0/I_{thr}-1}+\epsilon\right]\left(1+\alpha^2\right) \tag{1.1}$$

where γ is the inverse of the photon lifetime, β_{eff} is the effective coupling coefficient of the spontaneous emission, ϵ is a factor dependent from the lifetimes of the levels 3 (upper level of the lasing transition) and 2 (lower level of the lasing transition) and from the total relaxation time of the upper level, I_0 is the bias current of the laser, I_{thr} is the threshold value of the current and α is the LEF. This formula predicts that the linewidth of QCLs is narrower than the value that we would obtain adopting the ST formula for conventional diode lasers. The first experimental investigation aimed to verify this prediction is reported in [4]. In Fig. 1.4 the experimental data from the measurements performed in [4] are compared with the theoretical result by using Eq. 1.1: both, experimental and theoretical values follow an hyperbolic trend, but the experimental values are always slightly smaller than the theoretical ones. This result demonstrates the low phase noise characterizing the single-mode emission of QCLs, which makes them ideal for several applications, such as the study of rotovibrational transitions of molecules in the mid-IR region.

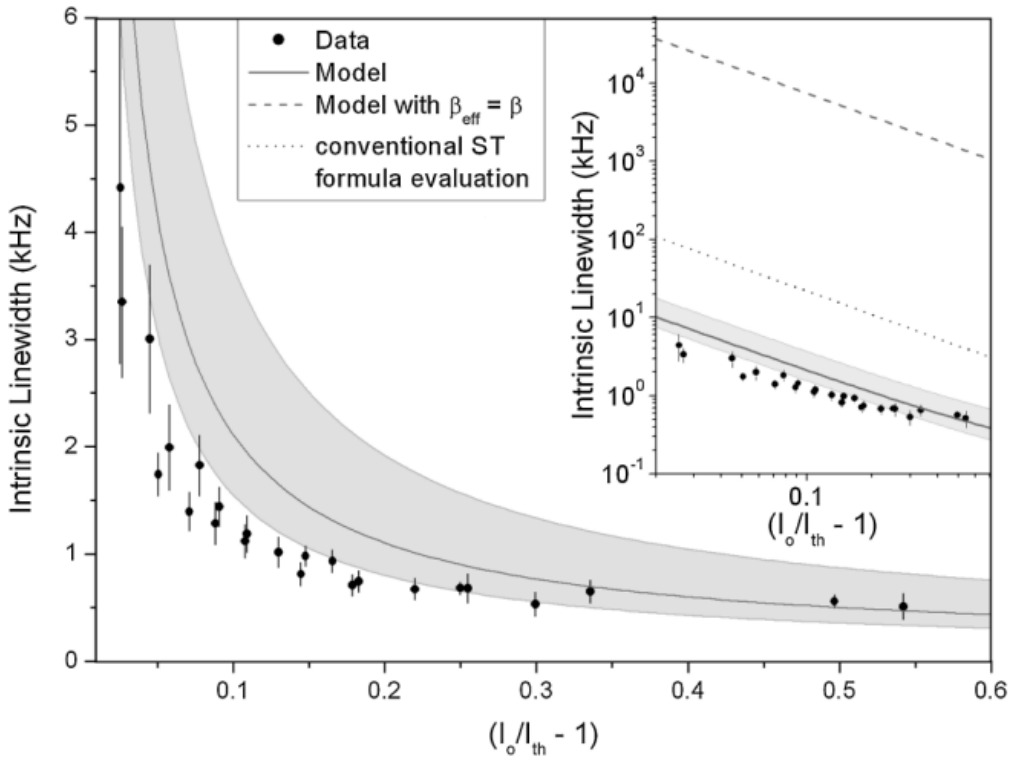

Figure 1.4: Comparison between the experimental measures of intrinsinic linewidth at different values of the bias current for a QCL, and the theoretical prediction from Eq. 1.1. Reproduced from [4].

Let us remind that in QCLs the electronic transitions are intersubband. If the subbands involved in the electronic transition are perfectly parabolic, the gain and therefore the refractive index present a symmetric profile, which corresponds to a situation similar to the atomic transitions, and therefore to a value of α close to zero. Indeed, the gain profile of QCL media is not perfectly symmetric, and therefore the value of α is not exactly zero, because of several factor, including the non perfect parabolicity of the subbands [49]. Measured values in the range 0.1-0.5 in the THz region [24], [74], and values at room temperature between 0.2 and 3 [49], [68] are reported.
We can conclude that the fact that the single-mode emission is characterized by a low phase noise, makes QCLs suitable for the emission of locked regimes characterized by low multimode phase noise, i.e. OFC. Therefore, the α factor plays an important role in the frequency combs dynamics, in both Fabry-Perot [47], [63] and ring [50], [13] devices.

1.2 Optical Frequency Combs

OFC are defined as coherent radiation characterized by a spectrum consisting of a set of lines (modes) equally spaced which present a well-defined phase relationship between each other [19], as shown in Fig. 1.5. The set of frequency characterizing

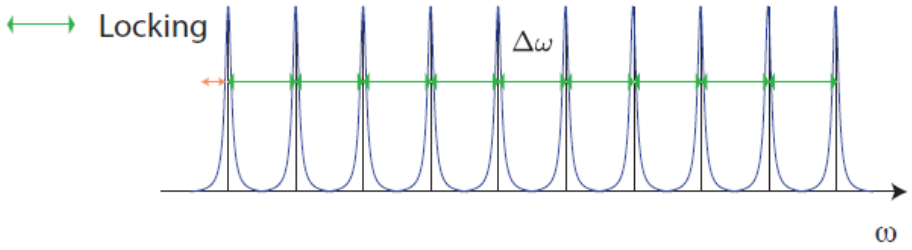

Figure 1.5: Schematic representation of an OFC whose lines are spaced of $\Delta\omega$. Reproduced from [19].

an OFC can be written as:

$$f_n = n f_{rep} + f_{off} \tag{1.2}$$

where n is an integer number, f_{rep} is the separation between two adjacent modes and f_{off} is an offset frequency.
The OFCs are different from an array of equally spaced optical lines, each of them emitted by different lasers: in fact in this last case there is absence of correlation between the noise of the individual lines.
The achievement of performing pulsed operation through passive mode-locking in QCL at room temperature resulted particularly hard, since the electron lifetime is relevantly less than the cavity roundtrip, in this class of devices. At criogenic temperature, in both mid-IR and THz QCL this type of pulsed regimes have been achieved by exploiting mode-locking.
In 2012 it has been demonstrated that QCL can act as source of OFCs [72] and the achievement of the self-generation of this regimes is due to strong nonlinearities which characterize the active region of a QCL. In particular, the short electron lifetime (about 0.29 ps in [19]) in the upper subband (state 3), implies the occurrence of a broadband four-wave mixing process [20], wider compared to interband semiconductor lasers. Furthermore, in [17] measurements of four-wave mixing for a QCL heterostructure have been performed and the final result of this study showed that the considered material has a large and resonant third-order susceptibility $\chi^{(3)}$ intrinsic of the medium. The performed measurements also show a certain agreement with the theoretical prediction obtained by exploiting a 2-level model.

The experiment, whose result is shown in Fig. 1.6, exploits two sources, a DFB

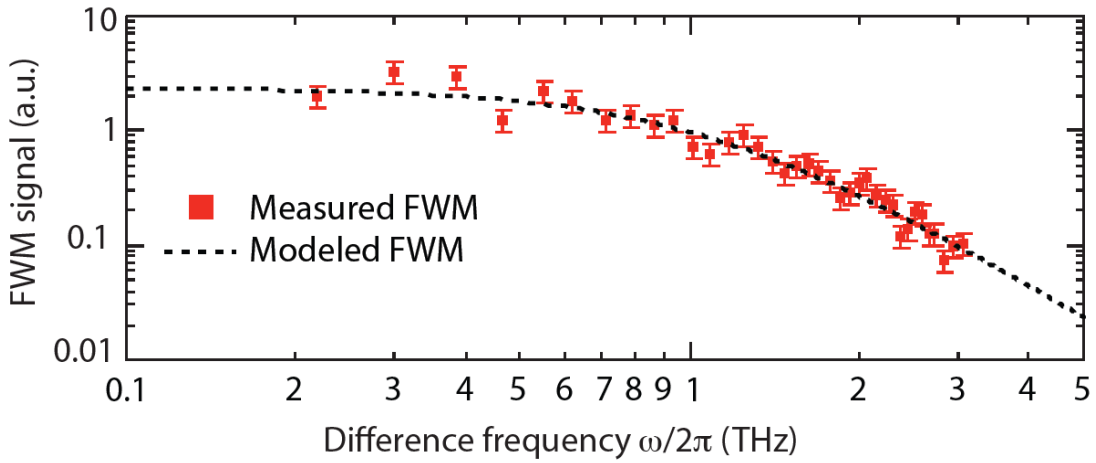

Figure 1.6: FWM signal as a function of detuning between the two sources used in the experiment (points), compared with the predictions of a two-level model (dashed lines). Reproduced from [20].

QCL and a tunable source based on difference frequency generations, whose emitted light is conveyed onto a QCL amplifier, in order to measure its four-wave mixing signal.
The main applications of OFCs generated by QCLs are in the field of spectroscopy, e.g. for environmental sensing, medical measurements, imaging for astronomy, oxymetry and security purposes. Particularly interesting is the so called Dual Comb Spectroscopy, which is important because it allows for the analysis of materials by exploiting Fourier transform spectroscopy with high resolution and fixed setup [19].
Dual comb spectroscopy exploits two coherent frequency combs, and it allows the measurement of the spectral response of a material specimen by performing a tooth-by-tooth analysis. The basic scheme of a setup for this technique, shown in Fig. 1.7, is based on two combs with different value of f_{rep} in a configuration type local oscillator-source. This typology of spectroscopy is particularly useful in the mid-IR region, where several molecules have their characteristic rotovibrational absorption lines and can be therefore detected and analyzed.
For all these reason the study of OFCs emitted by QCLs has assumed a growing relevance in the last decades from both, experimental and theoretical point of views [49]. In this work the focus is on the numerical modelling of the OFC emission by using these devices. To this topic chapter 2 and 3 are dedicated.

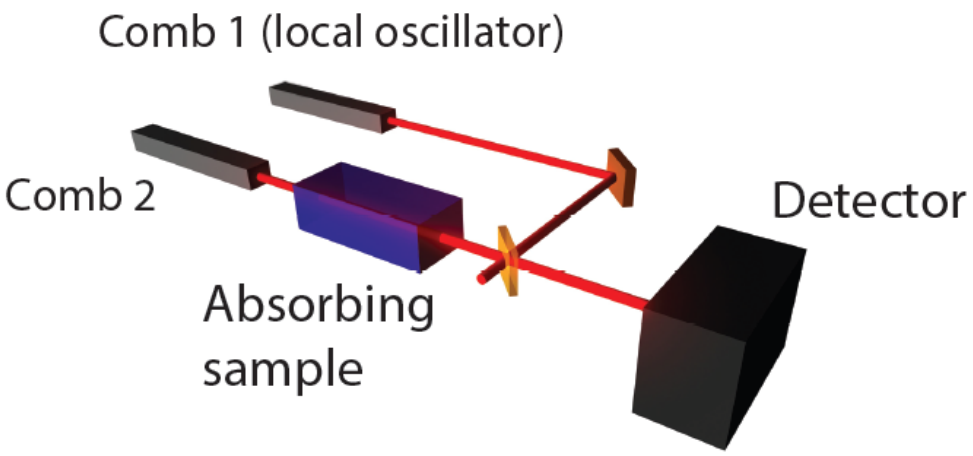

Figure 1.7: Scheme of a setup for dual comb spectroscopy. Reproduced from [19].

1.3 Self-Detection Scattering Near-Field Optical Microscopy

The second part of this work is devoted to the study of QCL in presence of optical feedback. This part is developed in Chapter 4 and it concerns a nanoscopy technique based on the combination between Self-Mixing Interferometry (SMI) and Scattering Near-Field Optical Microscopy (s-SNOM). This technique has been named SD s-SNOM and in this introductory section we give a general overview about it, in order to highlight the original results presented in Chapter 4. Therefore, first we review the fundamental aspect of SMI, underlining its advantages and main applications; then a general description of s-SNOM is presented; finally we explain the main features of the SD s-SNOM.

1.3.1 Self-Mixing Interferometry

It is very well known that the optical feedback is detrimental for the laser diode source of an optical transmitter. The light back scattered from the optical fiber or other parts of the optical communication system may lead the laser in an unstable regime characterized first by the broadening of the laser linewidth and then by the coherence collapse. In this context the optical feedback is a detrimental unwanted effect and optical isolators are often employed to suppress the optical feedback.
However in other kind of applications the light, back scattered from the target, and the way it perturbs the laser can be exploited to retrieve information about the target.
The possibility to exploit the light back-scattered from a target into the cavity of a

laser as a tool for sensing is the principle of the SMI technique. In fact the nonlinear superposition between the back-scattered field, which carries the information about the scattering target, and the field inside the cavity modifies the laser threshold, emission frequency and output optical power. By measuring these quantities modified from the feedback it is possible to retrieve information related to the target optical susceptivity, position, velocity, etc (cinematic and optical properties).
Let us consider a schematic representation of the Self-Mixing shown in Fig. 1.8. The laser has two mirrors defining the resonator with reflectivities R_1 and R_2, and

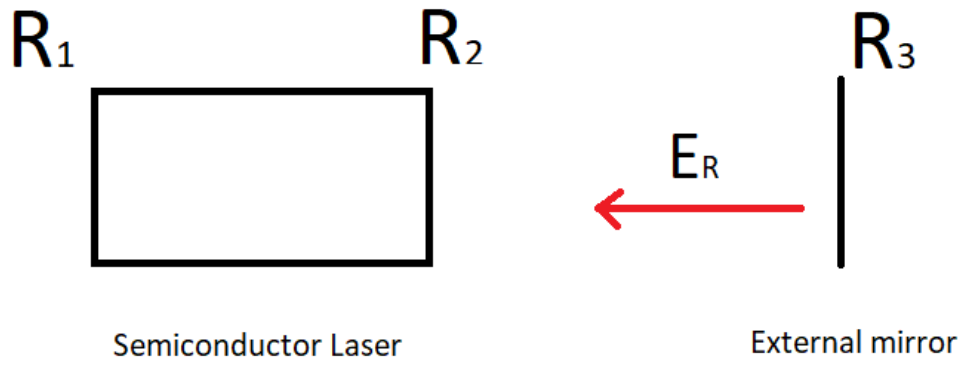

Figure 1.8: Scheme of Self-Mixing configuration. E_R is the delayed external field.

in addition the external target at distance L acts as a pure reflector with reflectivity R_3, determining the existence of an external cavity delimited by mirrors R_2 and R_3. The field is reflected from the target (pure reflection, in the following a more complex interaction will be considered) and the reflected field E_R partially re-enters into the laser cavity through the laser mirror and interferes with the intracavity field. This interference phenomenon produces a modification of the main characteristics of the lasers, as for instance the emission frequency, the output power, the voltage across the laser contacts. From the changes of these quantities it is possible to retrieve information about the target.
The theoretical description of the Self-Mixing is based on the Lang-Kobayashi (LK) model, which will be described in the following subsection.

1.3.2 Lang-Kobayashi Model

In order to properly describe the self-mixing effect in semiconductor lasers, in 1980 Lang and Kobayashi proposed a theoretical model based on modified rate equations for a single mode laser, which encompasses the effect of weak optical feedback [36].
Being a rate equation model, the dynamical variables are the electric field and the carrier density of the semiconductor laser (population inversion, in other classes of lasers). Let us consider the first variable of the model, the electric field, described by a complex function, which is assumed to be the product of a time-dependent slowly-varying envelope E(t) and an oscillating term $e^{i\omega_0 t}$, where ω_0 is the frequency of the emitted radiation in absence of optical feedback.
The rate equation for the electric field envelope is given by [36]:

$$\frac{d}{dt}E(t)e^{i\omega_0 t} = \left\{ i\omega_N(n) + \frac{1}{2}(G(n) - \Gamma_0) \right\} E(t)e^{i\omega_0 t} + \widetilde{\kappa}E(t-\tau)e^{i\omega_0(t-\tau)} \tag{1.3}$$

where $\omega_N(n)$ is the longitudinal mode frequency, expressed by $\omega_N = \frac{N\pi c}{\eta l}$. N is an integer number, c is the velocity of the light, l is the length of the laser cavity, and η is the effective refractive index of the laser medium, which has a dependence on the carriers density n. $G(n)$ is the carriers density-dependent optical gain, Γ_0 is the term related to the cavity losses. The last term in the RHS represents the reinjected field, which is weighed by the coupling coefficient $\widetilde{\kappa}$ which depends on R_2 and delayed by a time τ which corresponds to the round-trip time of the light through the external cavity and is given by:

$$\tau = \frac{2L}{c} \tag{1.4}$$

where L is the laser-target distance, i.e. the length of the external cavity.
Let us briefly review the meaning of the terms in Eq. 1.3. The first term in the right hand side of the equation for the field describes the phase-amplitude coupling. In fact it can be straightforwardly noticed that changes in the amplitude determine changes in the carrier density, which in turn cause changes in the refractive index of the medium and therefore in ω_N. The second term takes account of the stimulated emission process and the cavity losses. In conventional laser diodes rate equations these two terms are already present. The particularity of the LK equation for the field is in the third term, which encompasses the effect of the feedback, by the inclusion of a delayed electric field term, multiplied by a feedback coefficient $\widetilde{\kappa}$. This feedback coefficient is a relevant quantity in the study of self-mixing, and as we will see later also for the s-SNOM configuration (where it is a complex parameter).
We now derive the explicit expression of $\widetilde{\kappa}$, taking into account the external cavity configuration. Since $E_i e^{i\omega_0 t}$ is the incident field on the right laser mirror, with reflectivity R_2, and $E_{tr}e^{i\omega_0 t}$ is the total reflected field from the same mirror in

presence of optical feedback, we can write:

$$E_{tr}e^{i\omega_0 t} = \left[\sqrt{R_2} + (1-R_2)\sqrt{R_3}e^{-i\omega_0\tau}\right] E_i e^{i\omega_0 t} \tag{1.5}$$

The reflectivity of the right mirror in presence of feedback is:

$$r_{eff} = \frac{E_{tr}}{E_i} = \sqrt{R_2}(1 + ae^{-i\omega_0\tau}) \tag{1.6}$$

where $a = (1-R_2)\sqrt{\frac{R_3}{R_2}}$.
We can now retrieve the cavity loss in presence of feedback, using the conventional expression for laser diodes:

$$\Gamma = \Gamma_w - \frac{c}{\eta l}\ln\left[r_{eff}\sqrt{R_1}\right] = \Gamma_w - \frac{c}{\eta l}\ln\left[\sqrt{R_1 R_2}(1 + ae^{-i\omega_0\tau})\right] = \Gamma_0 - \frac{c}{\eta l}\ln(1+ae^{-i\omega_0\tau}) \tag{1.7}$$

where Γ_w is the waveguide loss and Γ_0 is the cavity loss without feedback. If we compare the total loss term with equation 1.3 we can write:

$$\frac{1}{2}\Gamma E e^{i\omega_0 t} = \frac{1}{2}\Gamma_0 E e^{i\omega_0 t} - \tilde{\kappa}E(t-\tau)e^{i\omega_0(t-\tau)} \tag{1.8}$$

and for $a \ll 1$ we have:

$$\tilde{\kappa} = \frac{c(1-R_2)\sqrt{\frac{R_3}{R_2}}}{2\eta l} = \frac{a}{\tau_c} \tag{1.9}$$

where τ_c is the laser cavity roundtrip.
The equation 1.3 for the field is accompanied by the rate equation for carrier density:

$$\frac{dn}{dt} = -\gamma n - G(n)\left|E\right|^2 + \frac{J}{ed} \tag{1.10}$$

where γ is the inverse of carrier lifetime, J is the injection current density, e is the electronic charge, d is the active region thickness and n_0 is the transparency carrier density. If we assume linear gain, we can write G(n) as [31]:

$$G(n) = G_n(n - n_o) \tag{1.11}$$

Also in this case we review the terms of Eq. 1.10: the first term of the right hand side accounts for the carriers loss, the second term describes the stimulated emission and the third term describes the pumping due to a current density J injected. Equations 1.3 and 1.10 are coupled.
It is possible to rewrite the equation 1.3 considering the typical gain of a semiconductor laser and introducing the linewidth enacemhent factor (LEF) sometimes indicated as the alpha-parameter, defined as

$$\alpha = -\frac{2\omega_{th}}{\eta_{th}}\left(\frac{\frac{\partial\eta}{\partial n}}{\frac{\partial G}{\partial n}}\right) \tag{1.12}$$

where η_{th} and ω_{th} are respectively the effective refractive index and the laser frequency at the threshold carrier density n_{th}, and including explicitly the carrier density dependence of ω_N. In [31] the calculation is developed with details. The final result is:

$$\frac{dE(t)}{dt} = \frac{1}{2}(1+i\alpha)G_n(n(t)-n_{th})E(t) + \widetilde{\kappa}E(t-\tau)e^{-i\omega_0\tau} \tag{1.13}$$

where n_{th} is the threshold carrier density.

Steady state solutions of the Lang-Kobayashi equations

Let us retrieve at this point the steady state solutions of the LK model. We will exploit the same method to retrieve the steady state solutions in presence of a complex scattering coefficient, characterizing the s-SNOM configuration. We rewrite the field $E(t)$ in terms of its modulus $E_0(t)$ and its phase $\theta(t)$:

$$E(t) = E_0(t)e^{i\theta(t)} \tag{1.14}$$

Therefore, Eq. 1.3 can be splitted in two equations for modulus and phase of the field:

$$\begin{aligned} \frac{dE_0(t)}{dt} &= \frac{1}{2}G_n(n(t)-n_{th})E_0(t) \\ &+ \widetilde{\kappa}E_0(t-\tau)cos\left(\omega_0\tau+\theta(t)-\theta(t-\tau)\right) \qquad (1.15) \\ \frac{d\phi(t)}{dt} &= \frac{\alpha}{2}G_n(n(t)-n_{th}) - \widetilde{\kappa}\frac{E_0(t-\tau)}{E_0(t)}sin\left(\omega_0\tau+\theta(t)-\theta(t-\tau)\right) \qquad (1.16) \end{aligned}$$

The solutions are retrieved by imposing the folowing conditions: $E_0(t)$=$E_0(t-\tau)$=E_s, n(t)=n_s and $\theta(t)$=(ω_s-ω_0)t into equations 1.15, 1.16 and 1.10, so that the derivatives of n(t) and E_0(t) are set to zero, and the derivative of $\theta(t)$ is set to ω_s-ω_0, where ω_s is the laser frequency at steady state.
We start from the Eq. 1.15 to retrieve the steady state carrier density:

$$\begin{aligned} 0 &= \frac{1}{2}G_n(n_s-n_{th})E_s + \widetilde{\kappa}E_s cos\left(\omega_0\tau+(\omega_s-\omega_0)t-(\omega_s-\omega_0)(t-\tau)\right) = \\ &= \frac{1}{2}G_n(n_s-n_{th})E_s + \widetilde{\kappa}E_s cos\left(\omega_s\tau\right) \qquad (1.17) \end{aligned}$$

and we obtain:

$$n_s = n_{th} - \frac{2\widetilde{\kappa}}{G_n}cos(\omega_s\tau) \tag{1.18}$$

At this point we want to express ω_s. We substitute Eq. 1.18 in the Eq. 1.16 after imposing the steady state conditions, and using $\widetilde{\beta}$=arctan(α):

$$\begin{aligned}
\omega_s - \omega_0 &= \frac{\alpha}{2} G_n \left[-\frac{2\widetilde{\kappa}}{G_n} cos(\omega_s \tau) \right] - \widetilde{\kappa} sin(\omega_s \tau) = \\
&= -\alpha \widetilde{\kappa} cos(\omega_s \tau) - \widetilde{\kappa} sin(\omega_s \tau) = \\
&= \widetilde{\kappa} \left[-tan(\widetilde{\beta}) cos(\omega_s \tau) - sin(\omega_s \tau) \right] = \\
&= -\frac{\widetilde{\kappa}}{cos(\widetilde{\beta})} \left[sin(\widetilde{\beta}) cos(\omega_s \tau) + cos(\widetilde{\beta}) sin(\omega_s \tau) \right] = \\
&= -\frac{\widetilde{\kappa}}{cos(\widetilde{\beta})} sin(\omega_s \tau + \widetilde{\beta}) \qquad (1.19)
\end{aligned}$$

Then, we obtain:

$$\omega_s = \omega_0 - \widetilde{\kappa} \sqrt{1+\alpha^2} sin\left(\omega_s \tau + \arctan(\alpha)\right) \qquad (1.20)$$

The equation 1.20 espresses the mode frequency of the laser in presence of the external cavity. As ω_s appears in the left-hand side and in the right-hand side of the equation 1.20, from a mathematical point of view, the steady-state emission frequency in presence of feedback is defined by an implicit function.
Multiplying both members of the equation 1.20 by τ and defining

$$C = \widetilde{\kappa} \tau \sqrt{1+\alpha^2} \qquad (1.21)$$

we obtain:

$$\omega_s \tau = \omega_0 \tau - C sin\left(\omega_s \tau + \arctan(\alpha)\right) \qquad (1.22)$$

Equation 1.22 is called the Phase Excess Equation. The parameter C is dimensionless and it is largely used to classify the different feedback regimes. For further details, see the next subsection.
Finally, we want to retrieve the steady state value of the photon density, and in order to do this, we substitute the expression of n_s given by Eq. 1.18 into Eq. 1.10, with $\frac{dn}{dt} = 0$:

$$P_s = |E_s|^2 = \frac{1}{G_n (n_s - n_0)} \left(\frac{J}{ed} - \frac{n_s}{\tau_s} \right) \qquad (1.23)$$

Equations 1.18,1.20 and 1.23 are the stationary solutions, also called continous wave solutions, of the LK model.

1.3.3 Feedback regimes

The feedback regimes in SMI are commonly classified according to the values for the dimensionless parameter C, defined by Eq. 1.21. In particular, intervals of values of C are defined according to the shape of the interferometric signal, which

has different characteristics for each regime. Considering the phase excess equation 1.22, we can notice that this is a trascendental equation and it can be proved that for C>1 it has multiple solutions for a fixed value of C [31].
Furthermore also the shape of the interferometric signal depends on the feedback. It can be proved that the power emitted by the semiconductor laser in presence of feedback can be expressed, in stationary condition from the LK model, as [22]:

$$P(\Phi) = P_0 \left[1 + mF(\Phi)\right] \tag{1.24}$$

where Φ is the interferometric phase given by Φ=2kL=τkc, with k=$2\pi/\lambda$, m is a modulation index, F(Φ) is a periodic modulation function of the interferometric phase and P_0 is the emitted power without reinjection of light. The modulation of the emitted power is the interferometric signal. The value of m and the shape of F(Φ) depends on the feedback parameter C.
At this point let us consider the classification of the different feedback regimes [22], [31]:

- C $\ll$ 1 - very weak feedback regime. From Eq. 1.22 we have $\omega_s \approx \omega_0$. Therefore this regime is characterized by a single emission frequency which corresponds to the frequency in absence of feedback. The modulation function F(Φ) is sinusoidal, therefore the interferometric fringes are sinusoidal.

- 0.1 < C < 1 - weak feedback regime. The interferometric fringes are distorted compared with the previous case (Fig. 1.9. a)). Also in this regime there is a single emission frequency.

- 1 < C < 4.6 - moderate feedback regime. This regime is characterized by multiple emission frequencies and interferometric signal has a sawtooth-like shape. F(Φ) is a multivalued function (Fig. 1.9. b)).

- C > 4.6 - strong feedback regime. Also in this case we have multiple frequencies. In fact F(Φ) can be five-valued (Fig. 1.9. c)). In some cases the laser enters mode-hopping regime and it is not possible to perform self-mixing measurements [22].

1.3.4 Scattering Near-Field Optical Microscopy

In this subsection we will review the main aspects related to the scattering-type s-SNOM. This is a nondestructive optical imaging technique which circumvents the diffraction limit with the aid of a sharp probing tip placed in the proximity of the material sample surface that we want to analyze. The tip, which has a near-field interaction with the specimen, is illuminated by a focused laser beam and the scattered light is collected and recorded. The processing of the detected signal enables

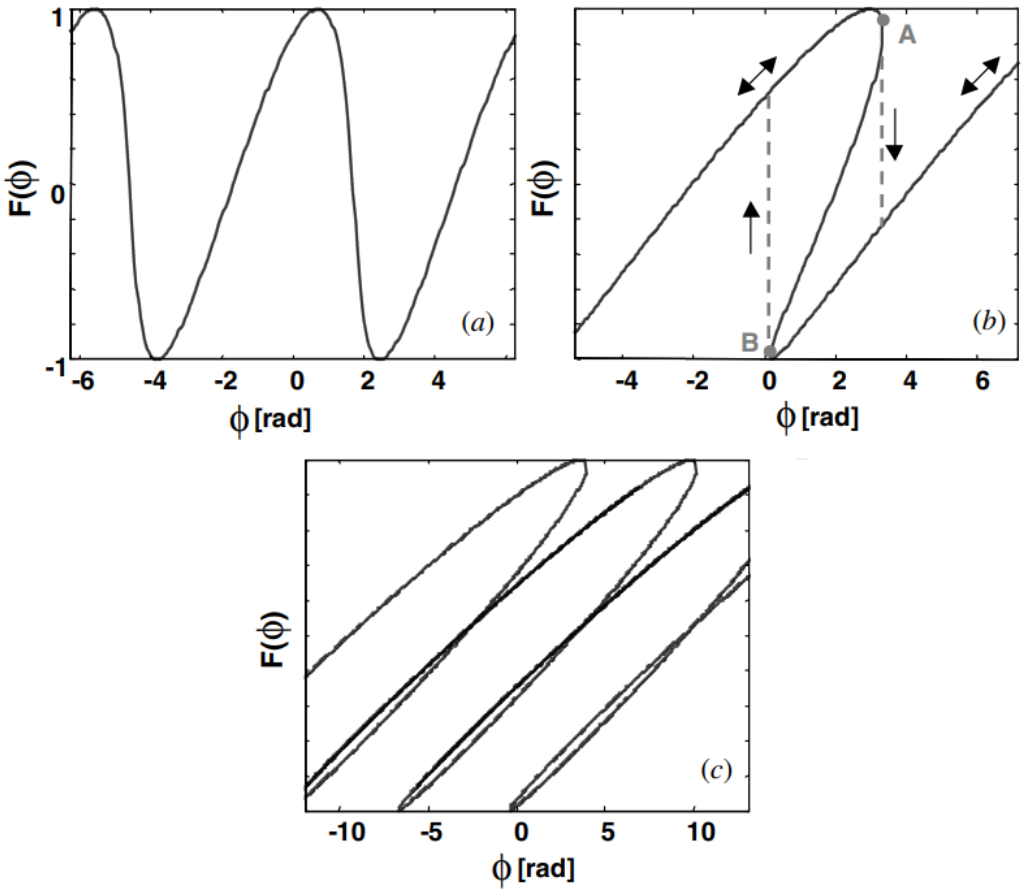

Figure 1.9: Calculated F(Φ) for different values of C. a) C=0.7; b) C=3; c) C=10. Reproduced from [22].

to retrieve information about the optical properties of the sample. The resolution is independent of the light wavelength, and is determined only by the radius of curvature of the probing tip. Therefore an optical map of the sample is achievable. Let us consider a typical setup for the s-SNOM, shown in Fig. 1.10. Even if in the shown scheme, the light source is a CO_2 laser, we remind that in this work we study an optical imaging technique based on near-field microscopy for analysis of materials in the region of Terahertz, exploiting a Quantum Cascade Laser as light source. Therefore the purpose of this paragraph is to describe the components of a generic s-SNOM setup, without proposing the actual scheme that we will be studied in the following (SD s-SNOM) which, in fact presents also fundamental differences in the detection part.
An atomic force microscope (AFM) is placed in proximity of the sample surface, and this represents the core upon which the s-SNOM setup is built. We have a piezoelectric scanner, which typically reaches nanometer precision in the x- and

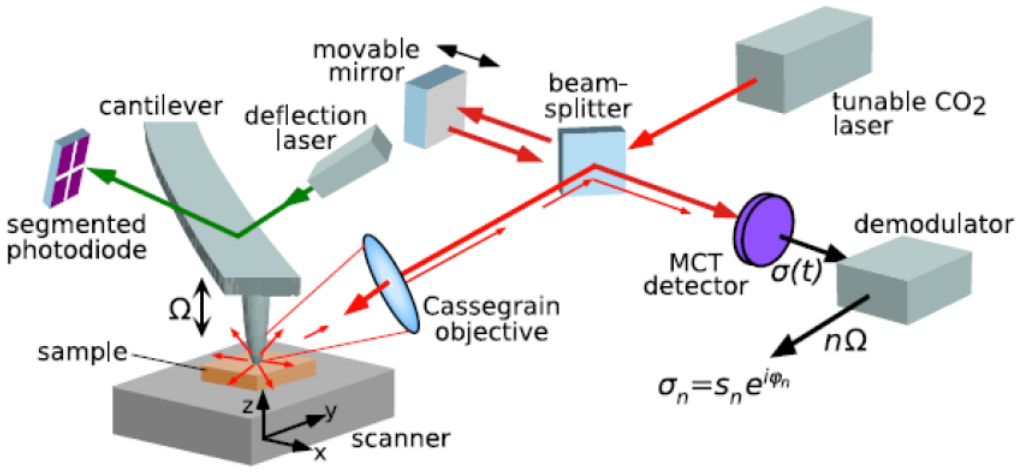

Figure 1.10: Experimental setup for s-SNOM. Reproduced from [48].

y-directions, and angstrom precision in z-direction. Another fundamental element of this core is the probing tip, which is connected to an oscillating cantilever, with typical oscillation amplitude on the order of $10^1 - 10^2$ nanometers. We define "tapping" mode operation of the AFM, the situation in which the tip apex touches the sample surface.
The top side of the cantilever reflects a laser (named "deflection laser") beam, subsequently focused on a four-segment photodiode. This system is used to monitor the vibration amplitude, actually regulated by an electronic loop system.
The CO_2 laser illuminates and polarizes the probing tip, which scatters radiation in all directions. Phase and amplitude of the scattered field are influenced by the sample-tip near-field interaction, so that an optical mapping of the specimen is achievable. The detection scheme shown in Fig. 1.10 is based on a Michelson interferometer. In this work, we will consider a different detection stage, which exploits SMI scheme.
The demodulation of the detector output at an integer multiple of the tip vibration frequency is necessary for retrieving useful information about the sample. Two main contributions to the scattered light are present: the useful signal, carrying the information about near-field interaction between tip and sample, and the background signal, independent from the interaction and consisting of radiation directly reflected by the tip and the optical elements present in the setup [48]. Since the background has a negligible dependence from the laser-tip distance, while the the evanescent fields which mediate the near-field interaction strongly vary with the tip displacement, the change in the scattered field will be mostly caused by the change in the near-field interaction strength, rather than the background scattering. In

order to extract the information about the near field interaction, it is necessary to filter out the harmonics which contain this information. Therefore it is explained the necessity to operate in the tapping mode, with vibrating frequency Ω.

Probe-sample interaction

The modelling of the interaction between AFM tip and sample in s-SNOM is a fundamental aspect in the theoretical study of this configurations. This has been achieved by using two different models, the Point Dipole (PD) and the Finite (FD) Dipole model [48]. In both of them an effective polarizability α_{eff} of the target consisting of interacting tip and sample, is considered and calculated. In this paragraph we review the fundamental aspects of the FD model, which will be exploited in the following part about SD s-SNOM and accounts for a more detailed description of the near field interaction. For more details, see [48].
The first hypothesis of the FD model is the approximation of the probing tip as a prolate spheroid. The choice of spheroidal shape is justified because of the similarity between the apex of a typical probing AFM tip and the apex of a spheroid. Furthermore, the tip apex is the most important part for the near-field interaction with the sample, since it resides in the closest proximity of the sample. The different shape far away from the apex does not influence the nature of the probe-sample interaction which gives rise to contrasts in s-SNOM.
Let us consider the expression for the electric field E_s generated by the spheroid along the its axis as a function of the distance z from the spheroid boundary[48]:

$$E_s(z) = \frac{\frac{2F(L+z)}{D^2+L(2z+a)} + ln\frac{L-F+z}{L+F+z}}{2\frac{F(L-\epsilon a)}{La(\epsilon-1)} - ln\frac{L-F}{L+F}} E_0 \tag{1.25}$$

where L is the length of the semi-major spheroid axis, F is half the distance between the foci, ϵ is the dielectric function of the probe material, E_0 is an homogenous external field illuminating the spheroid and a is the radius of the spheroid curvature at its apex.

At this point if we compare the exact solution from Eq. 1.25 to the field of a point dipole and an extended dipole, consisting of two monopole contributions, it is found out that the extended dipole provides a better approximation of the exact solution [48]. Therefore, we reduce the tip approximated as a spheroid in a homogeneous field E_0, to a finite dipole p_0, composed by the charge Q_0 placed in proximity of the sample and a charge -Q_0, where only Q_0 is involved in the near-field interaction. This interaction produces a further charge contribution Q_i in correspondence of the focus of the spheroidal tip, while $-Q_i$ resides in the middle of the spheroid [48]. In summary two point charges, Q_0 and Q_i, partecipate in near-field interaction and they induce a response on the sample which is given by respectively the charges -Q_0' and -Q_i'. In figure 1.11 a graphical picture of the

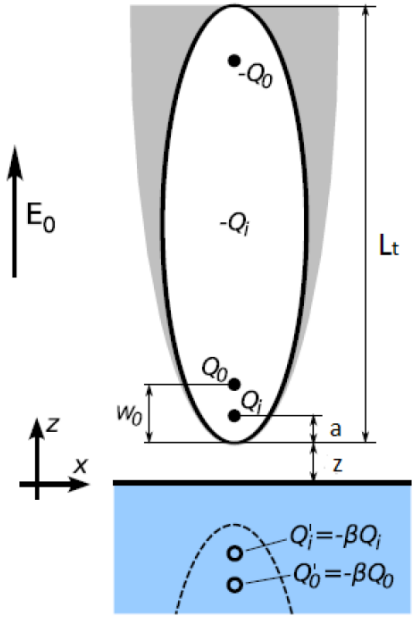

Figure 1.11: Scheme of Finite Dipole Model[48].

Finite Dipole Model is shown.
At this point it is possible to use this model to retrieve an effective polarizability α_{eff} of the tip perturbed by the near-filed interaction with the sample. The obtained expression for α_{eff} is:

$$\alpha_{eff} = \frac{p_{eff}}{E_0} \tag{1.26}$$

The calculation of α_{eff} as a function of tip-sample distance [48], according to the hypotheses of the FDM, gives:

$$\begin{aligned} \alpha_{eff} \quad = \quad & a^2 L_t \frac{L_t(\epsilon-1)\left[2L_t(\sqrt{1-\frac{a}{L_t}}) + aln\frac{(1-\sqrt{1-\frac{a}{L_t}})^2}{\frac{a}{L_t}}\right]}{2L_t\sqrt{1-\frac{a}{L_t}}(L_t-a\epsilon) - aL_t(\epsilon-1)ln\frac{(1-\sqrt{1-\frac{a}{L_t}})^2}{\frac{a}{L_t}}} \cdot \\ & \left[2 + \frac{\beta(g\frac{a+z}{L})ln\frac{4L_t}{4z+2a}}{ln\left(\frac{4L_t}{a}\right) - \beta\left(g - \frac{3a+4z}{4L_t}\right)ln\frac{2L_t}{2z+a}}\right] \end{aligned} \tag{1.27}$$

where L_t is the length of the major axis of the spheroid, a is the apex radius of the probing tip, z is the tip-sample distance, ϵ is the dielectric function of the tip, g is a complex factor related to the fraction of the total charge induced in the spheroid and β is a quantity depending on the complex dielectric function of the sample. Therefore, we can notice that α_{eff} is a complex-valued function. It represents the

polarizability of the tip in presence of near-field interaction with the sample.
At this point we define the complex scattering coefficient σ=S$e^{i\phi}$ as the ratio of the incident field E_0 and the scattered field E. This quantity will be particularly important in the treatment that we will develop in Chapter 4 about the theoretical study of SD s-SNOM. Since σ is proportional to α_{eff}, they are equivalent if measurements of relative contrast are performed.

1.3.5 Self Detection s-SNOM

In the two previous sections we revised the main aspects of SMI and s-SNOM. In this section we introduce an optical imaging scheme exploiting the combination of these techniques, the SD s-SNOM. In Chapter 4 of this work, the SD s-SNOM configuration will be largely analyzed and studied from theoretical and simulation point of view, in the weak feedback regime, with the realization of a comparison between the numerical results and some experimental measurements.

The experimental configuration of SD s-SNOM is shown in figure 1.12, and it

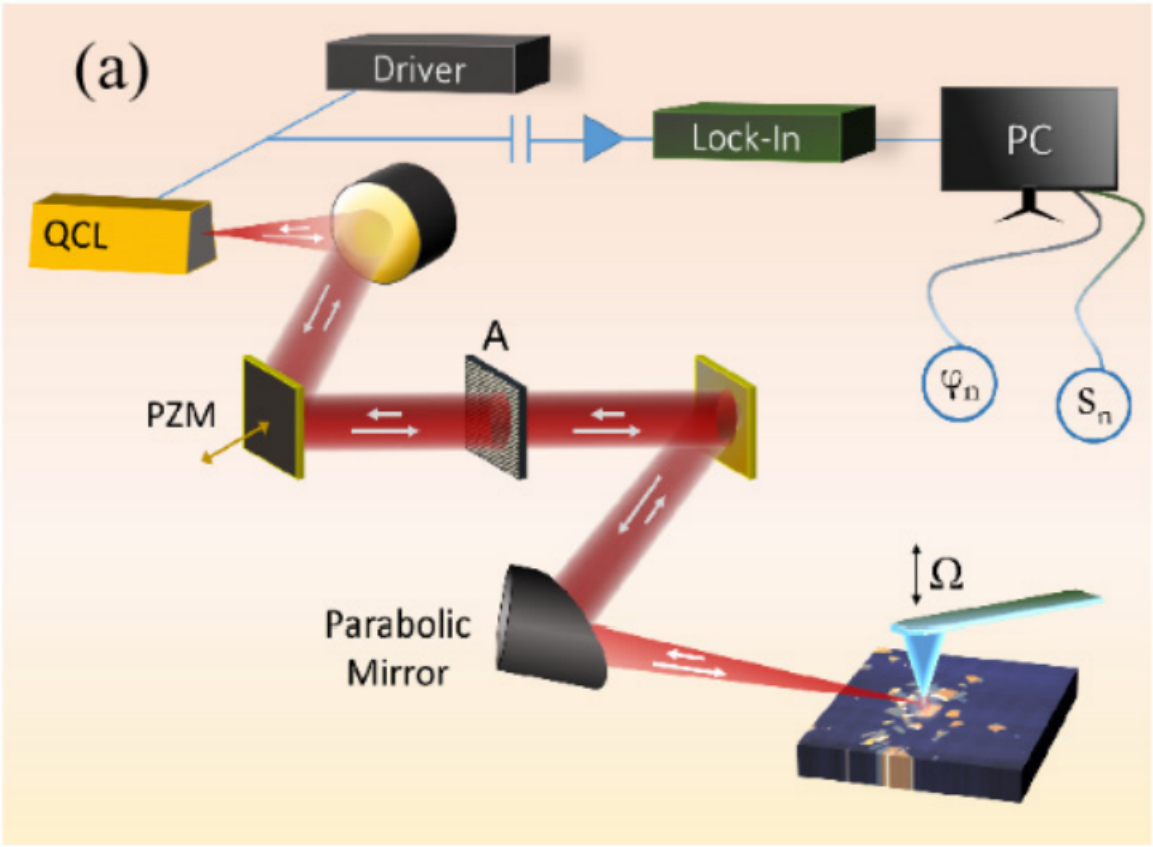

Figure 1.12: Experimental configuration of SD s-SNOM. Reproduced from [21].

enables analysis of optical properties of resonant materials in the region of Terahertz. In fact, the exploited light source is a THz Quantum Cascade Laser, which is also used as detector, according to SMI scheme. In the setup two paraboloid and two plane mirrors determines the path of the light, which is then focused onto the apex of an AFM tip in tapping mode, oscillating at the frequency Ω. The probing tip is placed in the vicinity of the sample, according to the s-SNOM scheme. The scattered light is then collected by the paraboloid mirror closest to the sample, travels the same incident optical path and is finally reinjected into the laser cavity. An attenuator (named A in the figure) is positioned into this configuration in order to select the intensity of the feedback. A lock-in amplifier is connected to the detector which, in this case, is the QCL itself. In s-SNOM configurations (and therefore also in SD s-SNOM) a lock-in amplifier is always present in order to filter the background dominating the signal, which would not allow to achieve contrast, preventing the performance of the imaging technique. Also a movable piezo-actuated mirror(PZM) appears in the setup, which consents to vary the light path length. It will be shown how this aspect is fundamental in the retrieval of the information about optical properties of the sample. The detected signal is the voltage across the terminals of the QCL.
The circumvention of the diffraction limit occurs because the near-field interaction between sample and probe is mediated by evanescent fields, which are not subject to the diffraction. The interaction modifies amplitude and phase of the light scattered by the probe, which is partially or totally reinjected into the laser cavity. In a conventional s-SNOM configuration the scattered light is collected into an external detector.
The intracavity and the back-scattered field, which carries the information about the analyzed material sample, interfere and modify the emission properties of the laser, i.e. the emission frequency, output power, voltage across the laser terminals. Analyzing the change in these properties, typically the voltage across the laser terminals, it is then possible to retrieve information about the target.

1.4 Conclusions

In this chapter of the thesis we reviewed some of the fundamental aspects of QCLs and the applications that will be studied in this work. In particular a focus was put on the possibility to engineer the Energy of the electronic transitions by realizing proper heterostructures with semiconductor materials characterized by thin layers realized with Molecular beam epitaxy. QCLs are unipolar devices, because they exploit only electrons and all the transitions occur between confined states in the conduction band, named subbands. By setting the energies of these subbands

in band scheme, it is possible to achieve coherent emission in the ranges of mid-IR and THz. We analyzed the materials and the features of the QCL cavity and the definition of OFC was introduced, which will be the main topic of the next two chapters of this work. OFCs offer the possibility to perform a spectroscopy of some materials in the mid-IR and THz regions, through the so called dual comb spectroscopy. They also have relevant applications in the field of free space communication.
Finally a brief introduction on SMI and on s-SNOM has been presented, in order to proper study the SD s-SNOM in the Chapter 4. This is a nanoscopy technique for the material analysis and imaging valid in the region of THz, which exploits a detectorless sensing with resolution independent from the wavelength.

Chapter 2

Multi-mode dynamics of Fabry-Perot Quantum Cascade Lasers

In this Chapter of the manuscript we deal with the QCL in the Fabry-Perot (FP) configuration, in order to study the spatiotemporal dynamics, evidencing the mode-locking phenomenon, and therefore investigate these devices as OFC sources. The Sec. 2.1 of this Chapter is dedicated to an overview about previous studies, both theoretical and experimental, evidencing the state of the art and the motivations for the research that will be presented in the following. In particular, the main experimental achievements related to the self-generation of OFC in QCLs and the most relevant theoretical models introduced for the simulation of these devices in multimode operation, are highlighted and presented. In Sec. 2.2 we explain the mathematical derivation of our original theoretical model, the Effective Semiconductor Maxwell-Bloch Equations (ESMBEs), which describe the multimode dynamics of a FP-QCL, and also we provide the simulation results obtained by numerically integration of this model, by studying a device emitting in the mid-IR. In particular, we reproduce important experimental evidences, such as the presence of linear chirp and the alternance between locked and unlocked states, and we highlight the role some fundamental parameters that regulate the dynamics of QCLs.

2.1 Introduction and motivation

It has been demonstrated that QCLs are capable to act as sources of self-generated OFCs in THz and mid-IR emission spectral regions. The growing interest for these devices is motivated by the existence of relevant applications, including high precision molecular spectroscopy, broadband free space optical communication

and hyperspectral imaging. Therefore a large amount of studies about the multi-mode dynamics of QCLs from both, experimental and theoretical point of view, is present in the literature.
In this section we will summarize the main results previously obtained for the QCLs in the FP configuration, in order to give motivation for the the study presented in the next sections, dedicated to our original results.
The FP configuration is characterized by an optical cavity made from two parallel plane mirrors. In Fig. 2.1 a realistic scheme of the FP configuration is shown, characterized by a cavity of length L, delimited by the two facets of the structure, and the active medium highlighted in red color.
In this type of resonator the typical modelistic treatment is based on the assump-

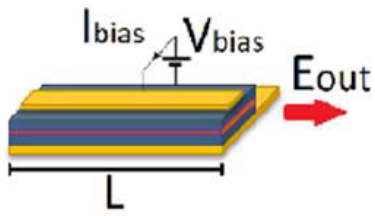

Figure 2.1: Scheme of a FP configuration for a QCL. The cavity has length L, and the active medium is underlined in red color. Top and bottom contacts are yellow in color. I_{bias} is the bias current, V_{bias} is the bias voltage and E_{out} is the output electric field.

tion that the electric field consists of the superposition of two fields propagating in opposed direction, a forward field and a backward field. When two counterpropagating waves with the same wavelength superimpose, they interfere and form a standing-wave pattern. As a consequence carriers are more effectively depleted in the nodes of the emerging standing wave, thus forming a periodic pattern for lower gaing with period half the wavelength. This phenomenon is called Spatial Hole Burning (SHB) and it characterizes FP cavities, but also ring cavities in presence of artificial defects in the active medium. Furthermore, it has been experimentally demonstrated that the population grating can also be non-stationary, exhibiting a time dependence when a beating of the the modes of the QCL occurs[52]. A graphic representation of the static and time-dependent grating is shown respectively in Fig. 2.2(b)-(c).
SHB is one of the mechanisms that brings to low current threshold for the switching from CW to multimode emission which, in presence of locking mechanism related to the nonlinearity of the system, can give origin to mode correlations and then to OFC [23, 78, 39]. The ultrafast dynamics of QCLs make these devices appropriate for the comb operation: in fact the short lifetime characterizing the upper subband

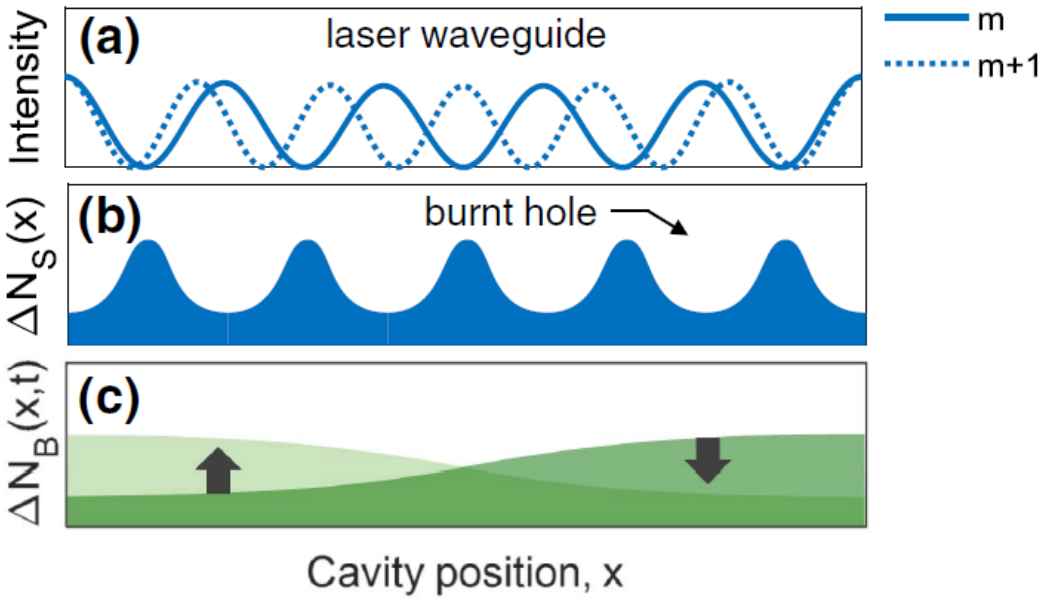

Figure 2.2: SHB in a standing-wave laser: a mode m oscillating in the laser cavity(a), induces a static grating ΔN_s (b). The beating with a mode m+1, induces a dynamic grating ΔN_B that oscillates as indicated by the arrows (c). Reproduced from [52].

produces a larger band for the FWM [19].
Since the first demonstration of QCL as a source of OFCs achieved in [29], the development of efficient methods for the characterization of these regimes from an experimental point of view has been addressed. Mainly they have been characterised through the intermode beatnote (BN) spectroscopy and their fingerprint is the presence of a narrow BN linewidth (order of magnitude of the KHz). The peaks in the BN spectrum correspond to multiple values of the FSR, which for the typical length of a QCL cavity, has an order of magnitude of tens of GHz. Typical experimental investigation about these regimes consists of a bias current sweeping, with analysis of Optical Spectra (OS) and BN spectra for different values of the current. In fig. 2.3 an example of RF spectra and OS for four values of the current is shown. We can notice that at 500mA the OS is composed by multiple lines and the BN at 7.50 GHz is narrow, typical of comb operation. For higher values of the current the OS spreads out when the pump increases, and also BN broadening is reported, corresponding to loss of coherence.
Several contributions in literature concern such altencance[19, 37, 81], when the bias current is swept from threshold onwards.
In order to fully describe OFC regimes, typical indicators characterizing mode-locked regimes corresponding to OFC generation are the number of locked modes in the $-20dB$ (or $-10dB$) spectral intensity range and the range of bias current

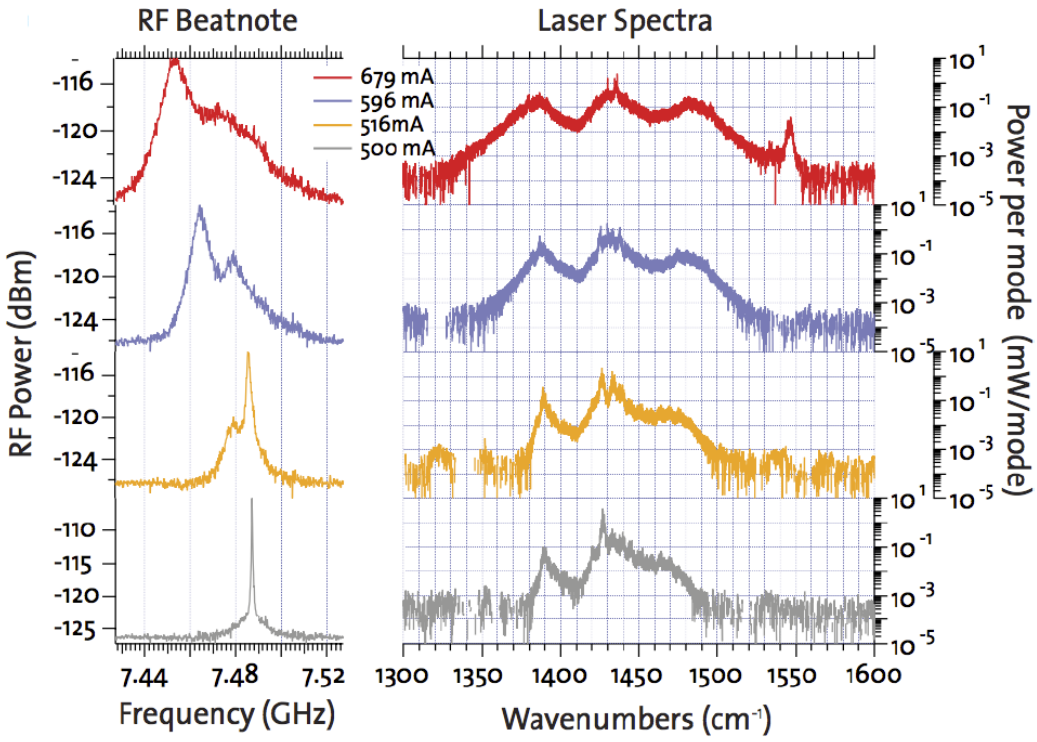

Figure 2.3: BN spectrum (left) and OS (right) at different values of the bias current for a comb QCL. Reproduced from [19].

where OFC emission occurs. For what concerns this, let us consider some typical values. THz and mid-IR QCLs present differences in terms of bandwith: while THZ QCLs emit few tens of modes in the $-40dB$ spectral range, whose width is about $1THz$, Mid-IR QCLs generate self-locked optical modes in a bandwidth of about 3THz [61, 65].
Furthermore, in absence of any dispersion compensation [73, 44] or microwave modulation [40], stable OFC regimes have been found in current ranges of about one hundred milliamperes starting from about twice the lasing threshold [61, 65].
A significant improvement in the characterization of OFC regimes has been reached with the Shifted Wave Interference Fourier Transform Spectroscopy (SWIFTS), a technique that allows to access the temporal dynamics of the field, by the retrieval of amplitude and phase of the optical field from experimental data [8, 65, 47]. This method allowed to understand that the Frequency Modulated (FM) laser emission is accompanied by a relevant Amplitude Modulation (AM) [65, 27]. Fig. 2.4 shows an experimental measurement, explotiting the SWIFTS technique, where intensity and istantaneous frequency are plotted versus time for a FP QCL in OFC regime.

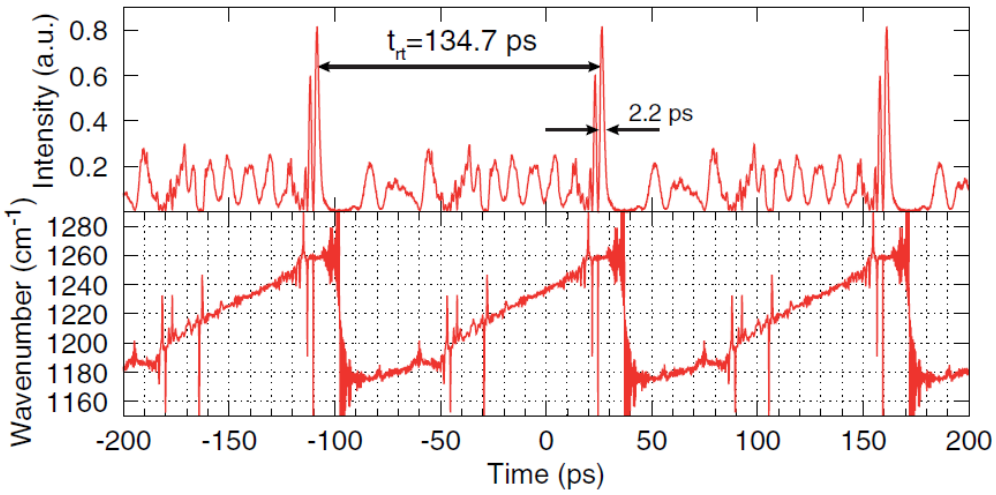

Figure 2.4: Intensity and instantaneous frequency time traces for a FP QCL, recovered by using the SWIFTS. Reproduced from [65]

.

It can be noticed that the intensity trace is characterized by optical pulses propagating on a constant background field, while the instantaneous frequency shows a non negligible modulation. In particular this result is an experimental demonstration of the existence in these dynamical regimes of linear frequency chirp, and frequency jumps occur at the instants where the amplitude is modulated by the pulse [27, 47].
In the literature a large class of works related to the theoretical modelling of the multimode dynamics of FP QCLs is reported, in order to physically explain the self generation of OFCs in these devices. The most challenging issue in this topic is the reproduction of some characteristic experimental evidences like the coexistence of optical pulses and linear frequency chirp, and also the alternance between OFC and chaotic regimes for increasing current.

Most of the proposed models are based on the treatment of the QCL as a classic atomic-like two o three levels system through Maxwell-Bloch Equations(MBE) [23, 72, 80, 71, 79, 33, 78]. Unlike the model that is introduced in this work in the next section (ESMBEs), these models do not encompass the presence of Linewidth Enhancement Factor (LEF), which describes the coupling between phase and amplitude of the field typical of semiconductor lasers. Furthermore, these models present another difference with the ESMBEs: they do not encompass some fundamental properties of the semiconductors, as the asymmetric gain profile. Whereas these

theoretical descriptions include the SHB, which is then the only physical mechanism responsible of the multi-mode instability of the device.
For instance in [33] a theoretical model obtained by solving with perturbative approach Maxwell-Bloch Equations in the frequency domain is retrieved and used to explain mainly the frequency modulation. This model predicts a pseudorandom frequency behaviour as the one shown in Fig. 2.5, coexisting with a constant intensity.

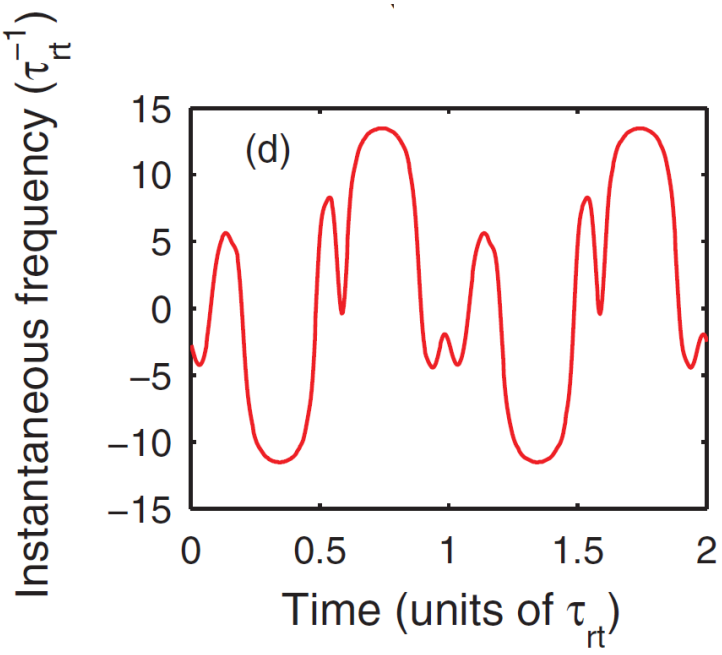

Figure 2.5: Instantaneous frequency time traces predicted with FD model presented in [33]. Reproduced from [33].

The same group developed a Time Domain (TD) model which also reproduces a pseudorandom-like FM modulation.
The following experimental evidences of the existence of linear chirp behaviour of the instantaneous frequency [65], have brought to the development of new models that try to reproduce more correctly the semiconductor characteristics. In fact the LEF and an inhomogeneous gain broadening have been "ad hoc" introduced in [27, 47] and the comparison with experimental results have reported a better match, as it is shown in Fig. 2.6. The integration of master equations derived in [47], reproduces in fact the experimental intensity behaviour and the linear chirp in the instantaneous frequency.

In [7] the QCL is described by a single Schrödinger equation with a phase potential, derived through the development of a mean-field theory, and the analytical solution of this equation brings to a correct reproduction of the experimental results

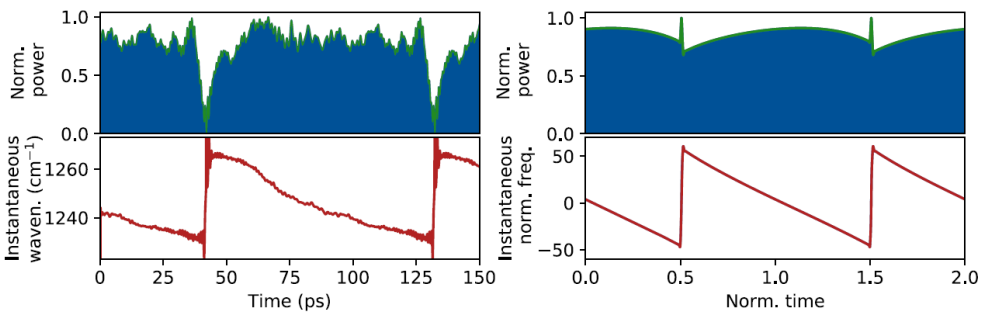

Figure 2.6: Experimental (left) and theoretical (right) results for a FP QCL, retrieved by using the model presented in [47]. Reproduced from [47].

for intensity and linear chirp.
Finally, we mention also an approach with standard rate equations for semiconductors lasers and the "ad hoc" addition of a Lorentzian filter in the field equation to mimic the finite gain line width thus avoiding unphysical multimode instability linked to unbounded mode proliferation [38].

2.2 Effective Semiconductor Maxwell-Bloch Equations

In this section the ESMBEs for the FP configuration are retrieved. This model exploits a susceptibility function which embodies the main characteristics of semiconductors, typical of a QCL (originally developed in [13] for an unidirectional resonator) combined with a multiple scale approach adopted for Quantum Dot (QD) lasers in [3] in order to account for carriers grating due to standing wave pattern and responsible for SHB, with the goal to properly describe a bidirectional FP resonator (see also Chap. 14 in [38]).
The retrieved equations are then integrated and the simulation results are presented in the second part of the section, showing an overview about the multimode emission of these devices, allowing us to discuss about the role of some specific parameters of the model in order to obtain self-generation of OFCs.

2.2.1 Derivation of the model

We want to study the spatio-temporal evolution of the electric field in a FP cavity a few millimeters long. Therefore, we begin our treatment, writing the d'Alembert equation:

$$\frac{\partial^2 E}{\partial z^2} - \frac{1}{v^2}\frac{\partial^2 E}{\partial t^2} = \frac{1}{\epsilon_0 c^2}\frac{\partial^2 P}{\partial t^2}, \tag{2.1}$$

where E is the electric field, P is the polarization, v is the radiation group velocity, c is the velocity of the light in vacuum and ϵ_0 is the vacuum dielectric constant. We impose the Slowly-Varying Envelope Approximation (SVEA) which amounts to applying the following ansatz on the spatio-temporal behaviour of electric field and polarization:

$$E(z,t) = \frac{1}{2}[E(z,t)^{+}\exp(-ik_0 z + i\omega_0 t) + E(z,t)^{-}\exp(+ik_0 z + i\omega_0 t) + c.c.], \quad (2.2)$$

$$P(z,t) = \frac{1}{2}[P_0(z,t)\exp(+i\omega_0 t) + c.c.], \quad (2.3)$$

where $E^{+}(z,t)$, $E^{-}(z,t)$ are respectively the slowly varying envelopes for the forward and backward fields inside the FP cavity and $P_0(z,t)$ is the polarization envelope, assumed to vary slowly only in time for reasons that will be clarified in the following steps of the derivation, ω_0 and k_0 are respectively the reference frequency (cold cavity mode closest to the gain peak) and wavenumber related to it.
In order to substitute Eqs. 2.2 and 2.3 in Eq. 2.1, we calculate the derivatives of field and polarization:

$$\begin{aligned}\frac{\partial E}{\partial z} &= \frac{1}{2}\left[-ik_0E^{+}\exp(-ik_0z + i\omega_0t) + \frac{\partial E^{+}}{\partial z}\exp(-ik_0z + i\omega_0t)\right] \\ &+ \frac{1}{2}\left[ik_0E^{-}\exp(+ik_0z + i\omega_0t) + \frac{\partial E^{-}}{\partial z}\exp(+ik_0z + i\omega_0t)\right] + c.c. \quad (2.4)\end{aligned}$$

$$\begin{aligned}\frac{\partial^2 E}{\partial z^2} &= \frac{1}{2}\left[-k_0^2E^{+} - 2ik_0\frac{\partial E^{+}}{\partial z} + \frac{\partial^2 E^{+}}{\partial z^2}\right]\exp(-ik_0z + i\omega_0t) \\ &+ \frac{1}{2}\left[-k_0^2E^{-} + 2ik_0\frac{\partial E^{-}}{\partial z} + \frac{\partial^2 E^{-}}{\partial z^2}\right]\exp(+ik_0z + i\omega 0t) + c.c. \quad (2.5)\end{aligned}$$

$$\begin{aligned}\frac{\partial E}{\partial t} &= \frac{1}{2}\left[i\omega_0\left(E^{+}exp(-ik_0z) + E^{-}exp(+ik_0z)\right)\right]\exp(i\omega_0t) \\ &+ \frac{1}{2}\left[\frac{\partial E^{+}}{\partial t}exp(-ik_0z) + \frac{\partial E^{-}}{\partial t}exp(+ik_0z)\right]\exp(i\omega_0t) + c.c. \quad (2.6)\end{aligned}$$

$$\begin{aligned}\frac{\partial^2 E}{\partial t^2} &= \frac{1}{2}\left[-\omega_0^2\left(E^{+}exp(-ik_0z) + E^{-}exp(+ik_0z)\right)\right]\exp(i\omega_0t) \\ &+ \frac{1}{2}\left[2i\omega_0\left(\frac{\partial E^{+}}{\partial t}exp(-ik_0z) + \frac{\partial E^{-}}{\partial t}exp(+ik_0z)\right)\right]\exp(i\omega_0t) \\ &+ \frac{1}{2}\left(\frac{\partial^2 E^{+}}{\partial t^2}exp(-ik_0z) + \frac{\partial^2 E^{-}}{\partial t^2}exp(+ik_0z)\right)\exp(i\omega_0t) + c.c. \quad (2.7)\end{aligned}$$

$$\frac{\partial P}{\partial t} = \frac{1}{2}\left[i\omega_0 P_0 exp(i\omega_0 t) + \frac{\partial P_0}{\partial t} exp(i\omega_0 t) + c.c.\right] \tag{2.8}$$

$$\frac{\partial^2 P}{\partial t^2} = \frac{1}{2}\left[-\omega_0^2 P_0 + 2i\omega_0 \frac{\partial P_0}{\partial t} + \frac{\partial^2 P_0}{\partial t^2}\right] \exp(i\omega_0 t) + c.c. \tag{2.9}$$

We insert the calculated derivatives and Eqs. 2.2 and 2.3 in Eq. 2.1 and we apply the slowly varying envelope approximation (SVEA),obtaining:

$$\left[\frac{\partial E^+}{\partial z} + \frac{1}{v}\frac{\partial E^+}{\partial t}\right] \exp\left(-ik_0 z\right) + \left[-\frac{\partial E^-}{\partial z} + \frac{1}{v}\frac{\partial E^-}{\partial t}\right] \exp\left(+ik_0 z\right) = gP_0, \tag{2.10}$$

where g is a complex coefficient given by:

$$g = \frac{-i\omega_0 N_p \Gamma_c}{2\epsilon_0 nc}, \tag{2.11}$$

and N_p is the number of stages in the cascading scheme of the QCL active region, Γ_c is the optical confinement factor (that takes into account the overlap between the optical mode and the active region) and n is the effective background refractive index of the medium.
Let us consider now the equation for describing the carrier dynamics in the QCL. The field dynamics is coupled to the active medium and in our model we assume that the electron, in the cascaded transport, returns to the ground state from the upper energy level via stimulated emission of photons and radiative and non-radiative recombination process. From the ground state the electron is then transferred to the next cascade stage via a very fast phonon-electron scattering process. For this reason we can assume that the ground state is always empty and the upper state is populated by the current injection. Therefore the only dynamical variable appearing in the model is the carrier density of the upper laser level $N(z,t)$. The evolution equation is retrieved from the Bloch two-level approach [38] by introducing the rotating wave approximation. We consider a bias current I, the carrier lifetime due to radiative and nonradiative decay process τ_e, and take into account the forward and backward field envelopes E^+ and E^-, as required for FP resonator. We obtain:

$$\begin{aligned}\frac{\partial N}{\partial t} &= \frac{I}{eV} - \frac{N}{\tau_e} - \frac{i}{4\hbar}\left[\left(E^+ exp(-ik_0 z) + E^- exp(+ik_0 z)\right) P_0^* \right. \\ &- \left.\left(E^{+*} exp(+ik_0 z) + E^{-*} exp(-ik_0 z)\right) P_0\right],\end{aligned} \tag{2.12}$$

where V is the medium volume and e is the electron charge.
The derivation of the equation for the polarization follows the approach described detailed in Sec.2 of [13]. The first step of the derivation is the introdction of

a phenomenological optical susceptibility $\chi(\omega, N)$ that encompasses fundamental characteristics of semiconductor materials. In fact it allows to describe spectrally asymmetric curves for gain and dispersion, generally dependent on the carrier density; it has the form given by the following equation (note that there is a different sign with respect to [13], due to the assumed expression for the complex electric field and polarization, i.e. Eqs. 2.2-2.3):

$$\chi(\omega, N) = \frac{f_0 N\,(1+i\alpha)\,(i-\alpha)}{(1+i\alpha)+i\omega\tau_d}. \tag{2.13}$$

where α is the LEF and $\frac{1}{\tau_d}$ is the effective polarization decay rate (due to different scalings $\frac{\Gamma}{\tau_d}$ in Eq.(13) of [13] corresponds to the effective polarization decay rate in Eq. 2.13).
The parameter f_0 is related to the differential gain, and it is possible to retrieve a typical value of it from experimental data by exploiting the P-I curve of a given QCL device.
Some further assumptions are introduced in Eq. 2.13: first of all we suppose that the reference frequency ω_0 coincides with the gain peak; therefore in Eq. 2.13 the variable ω=ω*-ω_0 is the deviation respect to the gain peak (note that the FSR is large enough so that a moderate frequency shift of the gain peak is of little relevance to the laser dynamics). The variation of the gain maximum with N is fixed by the ratio f_0/τ_d. Eq. 2.13 is associated in the time domain to the following polarization equation where the peculiar feature of the FP resonator is made evident by the dependency from the counterpropagating field envelopes:

$$\frac{\partial P_0}{\partial t} = \frac{1}{\tau_d}(1+i\alpha)\left[-P_0 + i f_0 \epsilon_0 \epsilon_b\,(1+i\alpha)\,N\left(E^+\exp\left(-ik_0 z\right) + E^-\exp\left(+ik_0 z\right)\right)\right] \tag{2.14}$$

,

For further convenience we introduce $\delta_{hom} = \frac{1}{\pi\tau_d}$, which is a measure of the FWHM of the gain spectrum in the limit $\alpha << 1$ where the susceptibility $\chi(\omega, N)$ becomes that of homogeneous broadened two-level system gain [13].
Now we want to separate forward and backward fields from Eq. 2.10, in order to retrieve a specific equation for each field. Therefore let us consider Eq. 2.10 and we set $k_0 z = \phi$, obtaining:

$$\left[\frac{\partial E^+}{\partial z} + \frac{1}{v}\frac{\partial E^+}{\partial t}\right]\exp\left(-\phi\right) + \left[-\frac{\partial E^-}{\partial z} + \frac{1}{v}\frac{\partial E^-}{\partial t}\right]\exp\left(+i\phi\right) = gP_0, \tag{2.15}$$

If we multiply Eq. 2.15 by $\exp(i\phi)$ and we integrate between $\breve{}\pi$ and π in ϕ, we have:

$$\frac{\partial E^+}{\partial z} + \frac{1}{v}\frac{\partial E^+}{\partial t} = \frac{g}{2\pi}\int_{-\pi}^{\pi} P_0 \exp(i\phi) d\phi \tag{2.16}$$

Furthermore, if we multiply Eq. 2.15 by $\exp(-i\phi)$ and we integrate between $\breve{}\pi$ and π in ϕ, we obtaing the corresponding equation for the bacward field:

$$-\frac{\partial E^-}{\partial z}+\frac{1}{v}\frac{\partial E^-}{\partial t}=\frac{g}{2\pi}\int_{-\pi}^{\pi}P_0\exp(-i\phi)d\phi \tag{2.17}$$

We have now two separated equations for forward and backward fields.
At this step of the derivation the retrieved equations include all spatial orders (measured in multiples of λ) for the field-carrier interactions, but in order to underline physical insights and obtain numerical viability, we can simplify our problem by using a multiple scale approach. Specifically, we expand in Fourier series the spatial variation at the wavelength scale of P and N:

$$P_0=exp(-ik_0z)\sum_{n=0}^{\infty}P_n^+exp\left(-2nik_0z\right)+exp(+ik_0z)\sum_{n=0}^{\infty}P_n^-exp\left(+2nik_0z\right), \tag{2.18}$$

$$N=N_0+\sum_{n=1}^{\infty}N_n^+exp\left(-2nik_0z\right)+\sum_{n=1}^{\infty}N_n^-exp\left(+2nik_0z\right). \tag{2.19}$$

Truncating these expansions respectively at n=0 and n=1 for P_0 and N, we obtain:

$$P_0=P_0^+exp(-ik_0z)+P_0^-exp(+ik_0z), \tag{2.20}$$

$$N=N_0+N_1^+exp\left(-2ik_0z\right)+N_1^-exp\left(2nik_0z\right). \tag{2.21}$$

Since N is the carrier density, it must be a quantity expressed by a real number, and therefore we have that N_1^- is the complex conjugate of N_1^+. Therefore, in the following it can be reported only the equation for N_1^+. Inserting Eqs. 2.20 and 2.21 into Eqs. 2.10), (2.12 and (2.14) we get the final set of ESMBEs for QCL in FP configuration in the form:

$$\frac{\partial E^+}{\partial z}+\frac{1}{v}\frac{\partial E^+}{\partial t}=-\frac{\alpha_L}{2}E^++gP_0^+, \tag{2.22}$$

$$-\frac{\partial E^-}{\partial z}+\frac{1}{v}\frac{\partial E^-}{\partial t}=-\frac{\alpha_L}{2}E^-+gP_0^-, \tag{2.23}$$

$$\frac{\partial P_0^+}{\partial t}=\frac{(1+i\alpha)}{\tau_d}\left[-P_0^++if_0\epsilon_0\epsilon_b\left(1+i\alpha\right)\left(N_0E^++N_1^+E^-\right)\right], \tag{2.24}$$

$$\frac{\partial P_0^-}{\partial t}=\frac{(1+i\alpha)}{\tau_d}\left[-P_0^-+if_0\epsilon_0\epsilon_b\left(1+i\alpha\right)\left(N_0E^-+N_1^-E^+\right)\right], \tag{2.25}$$

$$\frac{\partial N_0}{\partial t}=\frac{I}{eV}-\frac{N_0}{\tau_e}+\frac{i}{4\hbar}\left[E^{+*}P_0^++E^{-*}P_0^--E^+P_0^{+*}-E^-P_0^{-*}\right], \tag{2.26}$$

$$\frac{\partial N_1^+}{\partial t}=-\frac{N_1^+}{\tau_e}+\frac{i}{4\hbar}\left[E^{-*}P_0^+-E^+P_0^{-*}\right]. \tag{2.27}$$

Finally, the model equations must be completed by the boundary conditions which read:

$$E^-(L,t)=\sqrt{R}E^+(L,t), \tag{2.28}$$

$$E^+(0,t)=\sqrt{R}E^-(0,t), \tag{2.29}$$

where R is the reflectivity of each mirror of the symmetric FP cavity, here considered.

2.2.2 OFC indicators and chirp indicator

In the previous section we derived the ESMBEs for the FP configuration and our aim is to study the multimode emission of QCLs by solving this system of equations for a suitable set of parameters, in order to characterize the self-generation of OFCs in these devices. Therefore, by solving numerically the system, we obtain a description of the spatio-temporal evolution of the field inside the cavity. We want to classify the emitted regime according to the definition of OFCs. In particular, we want to assess some well defined indicators to indentify OFC emission.
A first characterization of the occurrence of an OFCs regime can be achieved, as typically done in experiments, by a narrow BN linewidth at Radio Frequency (RF). However a more rigorous assessment can be obtained by considering the definition of OFC. In fact an ideal OFC should have no intensity noise fluctuation of the power of each line (ie: low relative intensity noise per line) and zero differential phase noise. Therefore the indicators that we introduce are coherent with these characteristic: we estimate some phase and amplitude noise quantifiers that have been introduced for the first time in [3]for numerical characterization of OFCs in QD lasers. To calculate them, the spectrum of the optical field at z=L (exit facet of the simulated device) is filtered so as to retain only the modes within a 10dB power ratio to the spectral maximum. We then consider the temporal evolution of each filtered optical line of the spectrum: the modal amplitudes $P_q(t), q = 1, ..., N_{10}$ and the temporal phase difference between one mode and the adjacent one $\Delta\Phi_q(t), q = 1, ..., N_{10}$, where N_{10} is the number of optical lines in the $-10dB$ spectral bandwidth [3]. Given the amplitude and phase dynamics of each optical line, we calculate the quantities:

$$M_{\sigma_P} = \frac{1}{N_{10}} \sum_{q=1}^{N_{10}} \sigma_{P_q} \quad , \quad M_{\Delta\Phi} = \frac{1}{N_{10}} \sum_{q=1}^{N_{10}} \sigma_{\Delta\Phi_q}, \tag{2.30}$$

where:

$$\mu_{P_q} =< P_q(t) > \quad , \quad \mu_{\Delta\Phi_q} =< \Delta\Phi_q(t) >, \tag{2.31}$$

$$\sigma_{P_q} = \sqrt{< \left(P_q(t) - \mu_{P_q}\right)^2 >} \quad , \quad \sigma_{\Delta\Phi_q} = \sqrt{< \left(\Delta\Phi_q(t) - \mu_{\Delta\Phi_q}\right)^2 >}, \tag{2.32}$$

and the symbol $<>$ indicates the temporal average.
The indicators defined by Eq. 2.30 measure the average fluctuations of the power and phase of the selected optical lines. In our simulations we observe residual fluctuations, so that we will define in the following an OFC regime when the indicators are $M_{\sigma_P} < 10^{-2} mW$ and $M_{\Delta\Phi} < 2 \cdot 10^{-2} rad$.
Another characteristic of the comb regimes in the FP QCLs, as it is evidenced by experimental results [65], is the linear chirp behaviour of the instantaneous frequency.

It is then useful to obtain a complete characterization of our solution, to define a quantifier for the linearity of the chirp. Therefore we define here an indicator of chirp linearity, which is conceptually based on the comparison of the instantaneous frequency obtained from the simulation with a perfect frequency sawtooth signal [2].
Firstly we remember that the ratio of the moduli of two adjacent Fourier coefficients ($c_{n,st}$ and $c_{n+1,st}$) of the Fourier series of an ideal sawtooth can be written as $\frac{|c_{n+1,st}|}{|c_{n,st}|} = \frac{n}{n+1}$; secondly we calculate the Fourier transform of the instantaneous frequency signal, we define c_n the peak of each n-th component of the spectrum and the ratio $R_n = \frac{|c_{n+1}|}{|c_n|}$. We calculate then the relative error ϵ_n between $\frac{n}{n+1}$ and R_n for each component of the spectrum :

$$\epsilon_n = \left| \frac{R_n - n/(n+1)}{n/(n+1)} \right| \tag{2.33}$$

Finally we retrieve the average of ϵ_n over N_c components and we obtain (ϵ_c):

$$\epsilon_c = \frac{1}{N_c} \sum_{1}^{N_c} \epsilon_n \tag{2.34}$$

ϵ_c is the indicator for the linear chirp behaviour of the instantaneous frequency and it is the relative error aimed at quantifying the discrepancy between the QCL instantaneous frequency signal and an ideal sawtooth. We assume that a regime can be reasonably defined as 'linearly chirped' when $\epsilon_c < 10^{-1}$.

2.2.3 Numerical results

In this subsection we present the numerical results obtained by integrating the ESMBEs (2.22-2.27) with the boundary conditions (2.28)-(2.29) for a Mid-IR QCL emitting at λ=10μm with typical parameters reported in Table 1 and chosen according to the main references from literature [19, 65]. The equations have been solved by exploiting a code which implements a TDTW algorithm, with an advanced finite differences scheme in time and space [3].
The first target of our numerical study is the reproduction of OFC regimes which

Table 1. Typical parameters for a FP QCL

n	L(μm)	R	τ_e(ps)	Γ_c	f_0(μm^3)	V(μm^3)	N_p	λ_0(μm)
3.3	2000	0.3	1	0.3	1.1*10^{-7}	2240	50	10

present characteristics similar to those experimentally observed, namely: a combination of FM and AM OFCs occurring close to the lasing threshold and in a

significant bias current range, followed by a current range of unlocking with irregular dynamics and, possibly, occurring again in a second window for larger bias currents, a feature that is commonly observed in experiments, but that, to the best of our knowledge, was never found theoretically.
Therefore, the first results that we present are obtained setting the values of $\alpha = 0.4$ and $\delta_{hom} = 0.48$THz (corresponding to τ_d =0.66ps), which are reasonable and realistic values for these quantities. In the following, the role and the impact of these two parameters on the self-generation of OFCs will be studied, by presenting and analyzing the most relevant results of a massive campaign of simulations that evidenced a broad zoology of dynamical regimes.
The plot of the light-current curve corresponding to the selected values, is reported in Fig. 2.7. It can be noticed that, since our model does not encompass temperature dynamics or current blockades, the emission is not quenched for high values of the pumping parameter.

We swept the bias current I and applied the indicators defined in Eq. 2.32

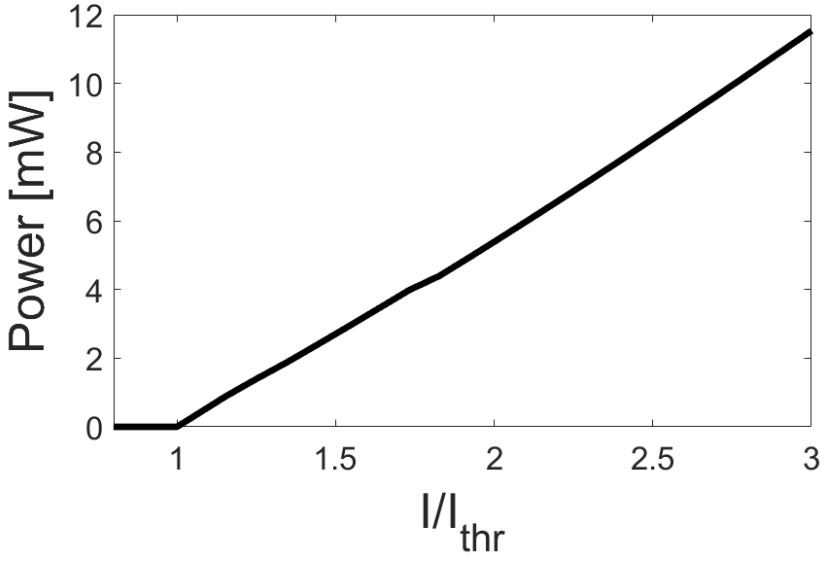

Figure 2.7: Power as a function of the ratio I/I_{thr} for $\alpha = 0.4$, $\delta_{hom} = 0.48$THz. In this case $I_{thr} = 260mA$. Power is the time average over a simulation time window of about $500ns$, after a stable regime is attained. Other parameters as in Table 1. Reproduced from [63].

and the chirp quantifier defined in Eq. 2.34 in order to identify and characterize OFC regimes. In Fig. 2.8 the results of a bias current sweeping are shown. From Fig. 2.8.a, we can notice that our QCL starts off with a CW emission at threshold ($I_{thr} = 260mA$), and then we have a destabilization of the CW towards a multi-mode dynamics, that we can recognize by noticing the appearance of a BN

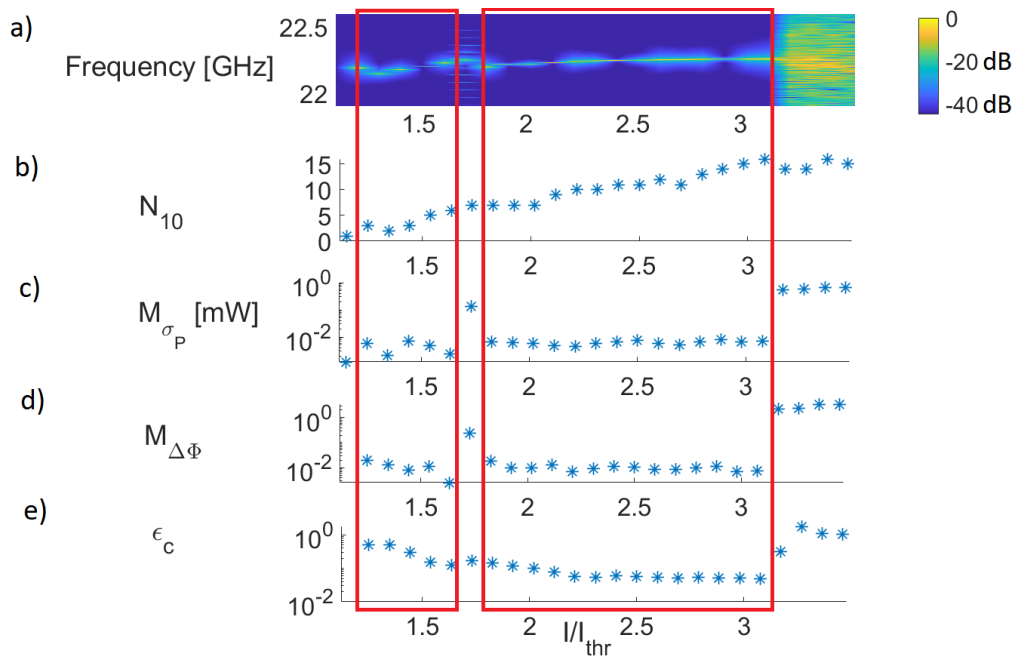

Figure 2.8: Results of simulations for a current scan from QCL threshold I_{th} to $3.5I_{th}$ for $\alpha = 0.4$, $\delta_{hom} = 0.48THz$. Other parameters as in Table 1. a) First BN in the RF spectrum (color scale normalized to the maximum for each current value; log scale); b) number of modes in a -10dB spectral bandwidth; (c) amplitude and (d) phase noise quantifiers for the N_{10} modes, as introduced in [3]; (e) chirp quantifier for the first $N_c = 5$ Fourier coefficients of the instantaneous frequency signal. Two regions of OFCs operation highlighted with a red rectangular box can be identified. Reproduced from [63].

for values of I/I_{thr} between 1.25 and 1.64. In this current interval we find OFC regimes characterized by a gradual increase of N_{10}. We can recognize these regimes as OFCs, since intensity and phase noise are low according to the definitions of the OFCs indicators ($M_{\sigma_P} < 10^{-2}mW$ and $M_{\Delta\Phi} < 2 \cdot 10^{-2}rad$). Furthermore the chirp indicator has a high value ($\epsilon_c > 10^{-1}$), so that we can not recognize linear chirp behaviour in this locking window. We also report a BN shift of $0.03GHz$ around $I/I_{thr} = 1.34$, which is in agreement, in terms of order of magnitude, with recent experimental results [45].
When the pump parameter reaches the value $I/I_{thr} = 1.73$ the OFC regime is lost. In fact in this case we observe in the RF spectrum several lines around the BN, which imply a relevant broadening of the BN linewidth. We recognize this broadening as a fingerprint of an unlocked regime. In particular this regime is characterized by an amplitude modulation with a period equal to the inverse of the separation

between the BN and the adjacent side bands. The corresponding phase and intensity noise indicators increase of nearly two orders of magnitude. At $I/I_{thr} = 1.83$ a new OFC window appears, extending up to $I/I_{thr} = 3.08$. According to this, we can state that by exploiting our model ESMBEs we are able to reproduce the locked/unlocked state alternance, which was found in some experiments [37].
After this second locking window chaotic emission has been reported in our simulations. Comparing in Fig. 2.8.e the linear chirp indicator of the first and the second locking window, we see that for all currents $I/I_{thr} < 2$ the value of ϵ_c is higher than 10^{-1}. In this region N_{10} is less than 9. The second locking region for $I/I_{thr} > 2$ is characterized by linear chirp with $N_{10} > 10$ and at the same time the number of locked modes increases and the linear chirp indicator decreases. We can conclude that this correlation between the reduction of ϵ_c and an increasing number of locked modes suggests that the linear chirp is a complex cooperative phenomenon involving a highly multi-mode dynamics (note that in calculating our ϵ_c we choose N_c=5).

Let us consider now some interesting cases of dynamical regimes that we found in this bias current scan. The first example of dynamics is shown in Fig. 2.9, for $I/I_{thr} = 2.31$, where I_{thr} is the threshold current of the laser. This dynamics, characterized by concomitant and relevant amplitude and frequency modulation, shows confined field structures propagating at the group velocity in the resonator and sitting on an almost constant background in the intensity trace (Fig. 2.9.a, blue curve). Furthermore, as it is shown in Fig. 2.9.a (red curve), the instantaneous frequency of the laser shows a linear chirp in the time range of nearly constant intensity and fast and discontinuous jumps when the intensity structure occurs. We found a strong similarity with the experimental evidences in Fig. 2.b of [65] and with the analytical predictions very recently reported in [7]. Figure 2.9 indicates, in excellent agreement with experimental evidence, that this OFC regime with a broad and flat optical spectrum is characterized by an almost linear frequency chirp.
Therefore we can assert that the regime shown here corresponds to an OFC with coexistence of AM and FM behaviour occurs.
By analyzing the Optical Spectrum, we observe 10 lines in the $-10dB$ spectral bandwidth of 0.2 THZ (Fig. 2.9.b); each line has a very narrow linewidth as shown by the zoom around one line in Fig. 2.9.c, as expected.
A paradigmatic case of irregular dynamics is observed for example at $I/I_{thr} = 3.46$. The output power and its instantaneous frequency versus time are shown in Fig. 2.10.a, respectively blue curve and red curve. We can notice that the behaviour characterized by intensity spikes sitting on constant background is lost, and the curve of the power as a function of the time has an irregular chaotic trend. The instantaneous frequency does not present a linear chirp. Furthermore, even though the whole optical spectrum corresponding to this case, shown in Fig. 2.10.b does not look too different from the locked case of Fig. 2.9.b, we can appreciate the

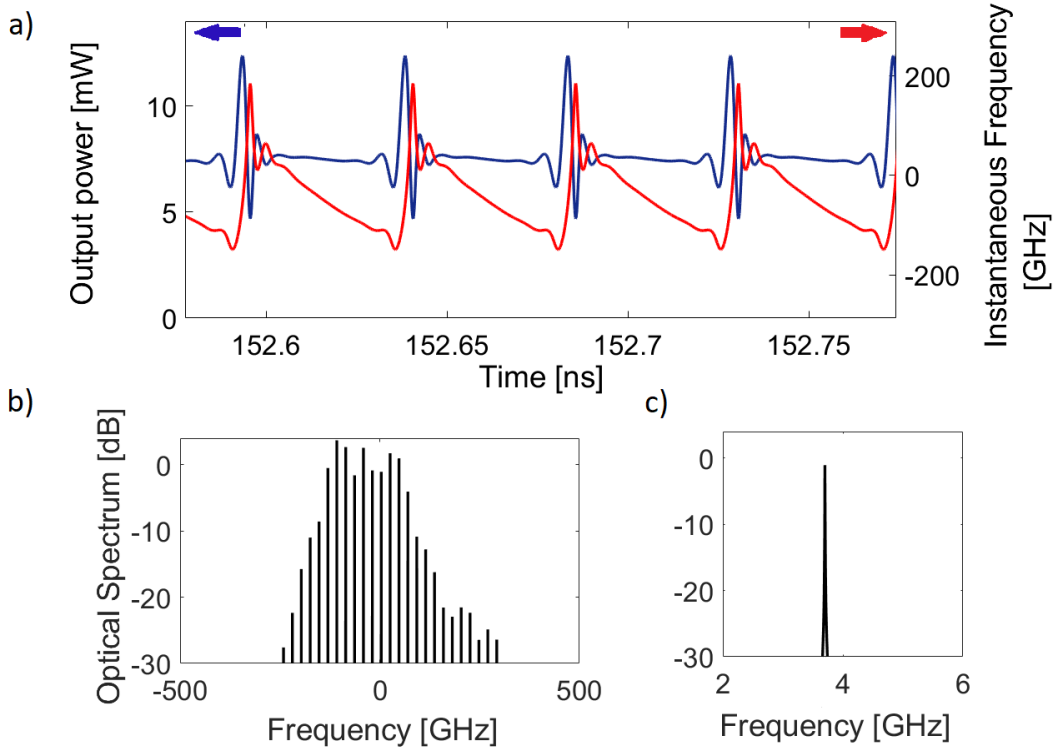

Figure 2.9: OFCs emission for $I/I_{thr} = 2.31$. Here $\alpha = 0.4$, $\delta_{hom} = 0.48THz$, other parameters as in Table 1. Temporal evolution of laser power (blue curve) and instantaneous frequency (red curve). A propagating pulse at the round trip frequency sits on an almost constant background associated with a linear frequency chirp. (b) Optical spectrum of the emitted radiation showing 10 modes in the $-10dB$ spectral bandwidth. c) Zoom around one peak of the optical spectrum. Reproduced from [63].

difference by zooming around the single line of the spectrum, noticing that each line is significantly enlarged and accompanied by several lines close to the main peak (Fig. 2.10.c).

2.2.4 OFCs properties: the role of LEF and gain/dispersion bandwidth

This subsection is dedicated to highlight the role of the LEF and the gain/refractive index dispersion in affecting both the bias current range where OFC can be observed and the figures of merit of the optical comb.
We run systematic sets of long ($> 500ns$) simulations by sweeping the bias current between the threshold I_{thr} and $3I_{thr}$ with a step of $0.19I_{thr}$, and considering

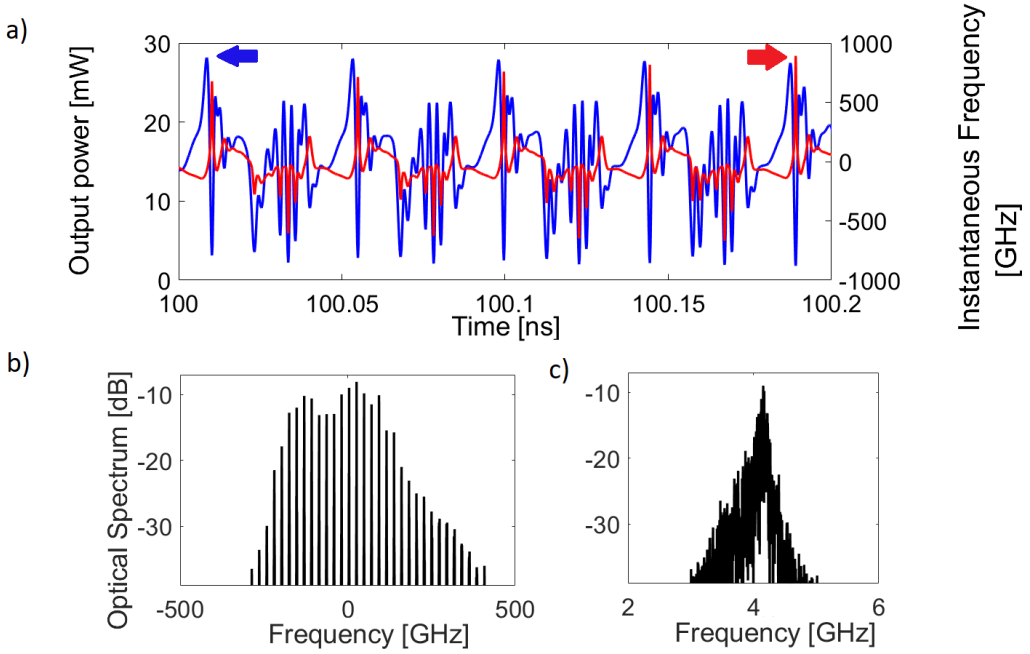

Figure 2.10: Chaotic behaviour for $I/I_{thr} = 3.46$. Other parameters are as in Fig. 2.9. (a) Temporal evolution of laser power (blue curve) and instantaneous frequency (red curve). Irregular oscillations are visible in the output power. (b) Optical spectrum of the emitted light. c) Zoom around one line of the optical spectrum. Reproduced from [63].

$\alpha \in (0.4, 1)$ and $\delta_{hom} \in (0.16\text{THz}, 1.27\text{THz})$. The other parameters are as in Table 1. Let us remind that the quantity δ_{hom} represents the homogeneous contribution to the FWHM of the threshold gain bandwith.
The results of these simulations are properly summarized in Fig. 2.11, where we report for each pair (α, δ_{hom}) a black circle when no locking is observed, and a red circle in case of OFC emission; in the latter case inside the circle we also report the main characteristics of the comb regimes we found: the FWHM of the gain spectrum at threshold, the maximum number of locked modes found in the $-10dB$ spectral bandwidth, the extension of the bias current interval ΔI where the OFC regime is found and the estimated values of ϵ_c.

We first observe that spontaneous OFC formation is found diffusely throughout the considered values of α and of δ_{hom}. Also, as a general trend, in the locked regime the number of locked modes N_{10} tends to increase with the FWHM of the gain curve as one may expect.
We also report that, for a fixed value of δ_{hom}, larger values of α increase the modal competition via nonlinear dispersion and reduce the range of ΔI where OFC is met in agreement with the results in [13]. In fact an increment of the modal competition

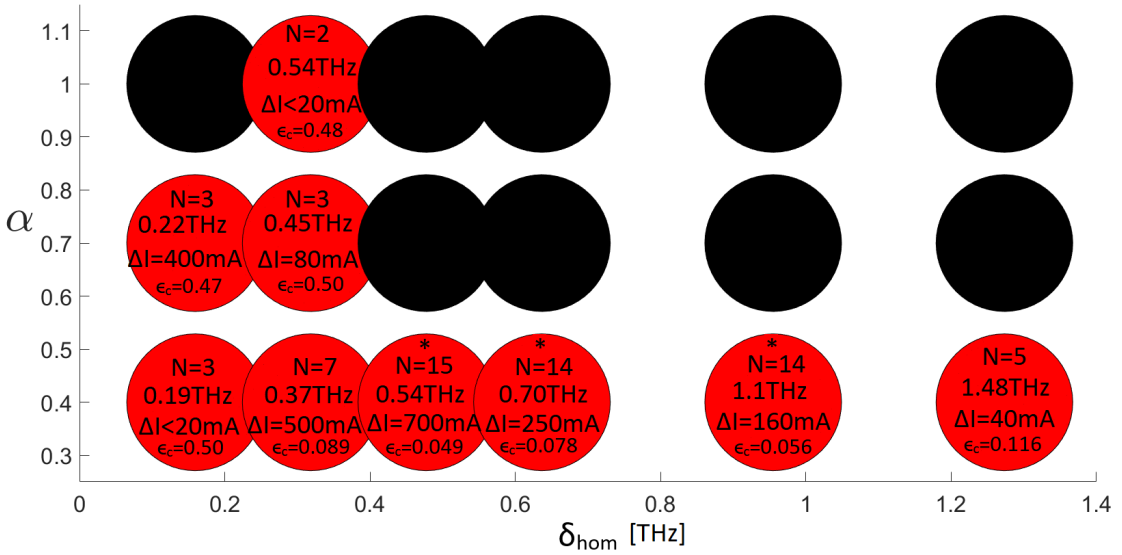

Figure 2.11: Analysis of locked regimes upon variation of parameters δ_{hom} and α. Black dots indicate that no locked regime could be found upon scanning the pump current in the interval $(I_{thr}, 3I_{thr})$. Red dots indicate parameter pairs where such regime could be found. In the dots the dynamical FHWM gain linewidth (see text) in THz is reported along with the current range where locking was found ΔI, the corresponding value of N_{10} and ϵ_c. The symbol '$*$' indicates the presence of more than one locking window. Reproduced from [63].

makes more difficult the achievement of the locking, which therefore occurs for a smaller interval of current. As an example, for e.g. $\delta_{hom} = 0.32$THz where OFCs are reported for all values of α, we found that ΔI drastically decreases as α increases. For fixed value of δ_{hom}, the increase of LEF is equivalent to an increase of the asymmetry or inhomogeneity of the semiconductor material gain spectrum which is deviating from the ideally symmetric homogeneous gain of two-level atoms. On the contrary, low value of LEF implies a more symmetric gain broadening, whereas the increase of δ_{hom} can be read as a reduction of the de-phasing time as typically observed increasing temperature. Finally, we report that when few number of modes are locked in the -10dB bandwidth (N_{10}<7), the resulting instantaneous frequency does not show a clear linear chirp behaviour since $\epsilon_c > 10^{-1}$ in these cases.
At fixed α, as a general trend an increment of δ_{hom} reduces the current range (or occurrence) for OFC regimes. These evidences seem consistent with the fact that the number of dispersed cavity modes for which the gain overcomes the losses increases with δ_{hom}, but the quantity N_{10} is actually limited by the efficiency of the FWM in locking the lasing modes that typically is an inverse function of distance from the resonance[19]. In this regard an anomalous behaviour is found at the map

edge where, for $\alpha = 1$ and $\delta_{hom} = 0.16$THz, we could not find any locked regime contrary to what happens for the two neighbouring circles of the map. We may argue that this low value of the gain FWHM implies a destabilization of the single mode solution for high bias currents where the multi-mode regime is prone to be chaotic for the relatively high value $\alpha = 1$. To corroborate this interpretation we checked that for $\alpha = 1$ and $\delta_{hom} < 0.16$THz only irregular multi-mode regimes are reliazed beyond the CW instability threshold.
Let us briefly analyze the results about the size ΔI of bias current generating the combs. If we focus on the case $\alpha = 0.4$ where we report OFC formation for all the considered δ_{hom}, for the lowest value of δ_{hom} we found a comb regime spanning just a few mA in the whole simulation interval $(I_{thr}, 3I_{thr})$; nevertheless, an extended comb regime of $\Delta I = 1000mA$ can be found for higher values of the pump current $(I/I_{thr} > 3)$. For larger values of δ_{hom}, ΔI keeps growing, it is maximum at $\delta_{hom} = 0.48$THz and then decreases.

In order to clarify the role of α in triggering the CW multi-mode , we observe that it was already shown how increasing this parameter lowers the threshold for the multi-mode lasing (see Fig.3a in [13]). In fact, since amplitude fluctuations lead to frequency fluctuations via α, in presence of sufficiently large gain and bias current, we expect that a CW emission will be destabilized more easily in presence of larger α. This mechanism is the only possible multi-mode source in an unidirectional ring resonator, but in a FP configuration it would compete with SHB, a second well known mechanism for CW instability [23, 78].

We numerically verified the previous considerations by simulating the QCL dynamics for $\alpha = 0$ (ideal two-level system). We set $\delta_{hom} = 0.48$THz, since it corresponds to the largest ΔI and maximum N_{10} when $\alpha \neq 0$. We also eliminate the SHB, to simulate a ring resonator, verifying that CW emission occurs at any current above threshold and even very far from threshold. We estimated the instability threshold (see Chap. 20-22 in [38]) and could verify that beyond that value $(I_{inst} > 13I_{thr})$ a RNGH multi-mode instability sets in when we assume that SHB is negligible in the FP laser. In the case of low transmissivity of the FP mirrors and without SHB we have also verified the set in of the RNGH instability at the current of 13 times the threshold current. This result is consistent with the expectation that in unidirectional, two-level case the well known RNGH instability is the only means to destabilize the single mode emission, triggered by the resonance of one cavity mode with the Rabi oscillation. By increasing α (e.g. setting $\alpha = 1.5$) and without SHB, we can confirm, in line with [13], that the multi-mode instability affecting the single mode CW emission appears very close to threshold.
When instead, keeping $\alpha = 0$, and the SHB is switched on, we observe again CW destabilization just above the lasing threshold as it was recently demonstrated for the QD laser case [3]. Moreover we verified that for the set of parameters of Fig. 2.9 we observe only irregular regimes. We therefore conclude that either the LEF

or the SHB can (alone or together) contribute to the multi-mode emission which however does not necessarily lead to an OFC regime. The self-locked regime is found only for proper bias currents, for proper combinations of LEF and homogeneous braodening linewidth and, as shown in the following, for fast enough carrier dynamics.

2.2.5 Pulses, chirping and OFC: the role of carrier dynamics

A relevant role in the formation of regular dynamics from multi-mode emission is played by the carrier decay time. In slow ($\tau_e \geqslant 100ps - 1ns$) conventional semiconductor lasers (for example in quantum well laser diodes) the spontaneous OFC formation is scarcely reported. In agremement with that, our numerical simulations showed that increasing τ_e from $1ps$ to $1.3ps$ leads to a pulse broadening (Fig.2.12). For larger τ_e, mode locking is lost for the same set of parameters of Fig.2.8 and α =0.

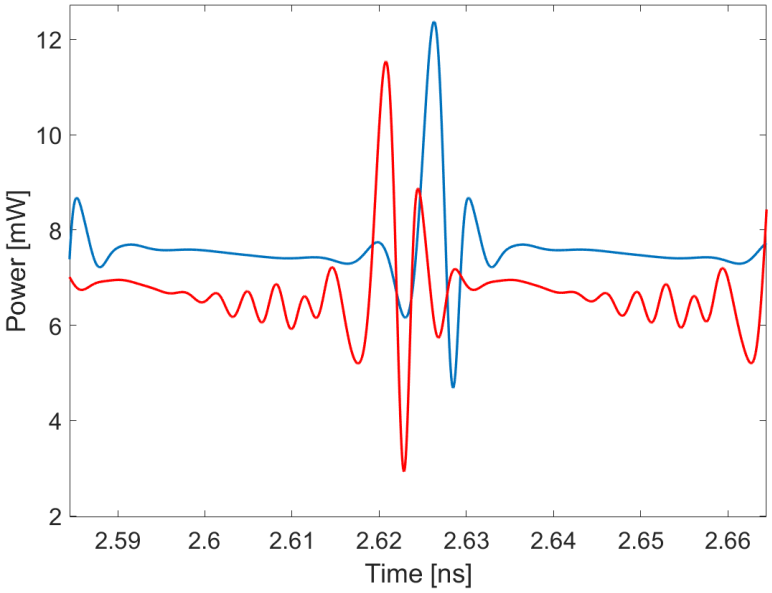

Figure 2.12: Zoom of a single power pulse for τ_e = 1ps (blue line) and τ_e = 1.3ps (red line) for $\delta_{hom} = 0.48$THz, $\alpha = 0.4$. Other parameters as in Table 1. The width of blue pulse is estimated 25ps, and 35ps for the red one. Reproduced from [63].

On the other direction, we investigated the behaviour for a fast carrier life time $\tau_e = 0.2ps$ (smaller than the value considered in previous sections). We also set $\alpha = 0.4$ and $\delta_{hom} = 3.18$THz, which gives a FWHM of the gain bandwidth at

threshold of $3.7THz$, much larger then those considered in the map of Fig. 2.11. This gain bandwidth is comparable with the one measured in [20]. We interestingly found that a reduction of the carrier lifetime is very beneficial in giving OFC regimes in quite wide bias current range and even for very large gain bandwidth FWHM. This seems to be consistent with the evidence reported in [20] according to which a very small carrier lifetime will result in very broad and strong FWM at the origin of the locking phenomenon.

Whereas the map of Fig.2.11 shows that increasing the gain FWHM the OFC regime might be lost, we stress here that the OFC regime is also strongly dependent on the carrier lifetime. Considering the reduced value of τ_eWe observe that that the increase of the gain bandwidth is accompanied by a significant increase of the number of comb lines N_{10}. The OFC and linear chirp indicators versus bias current are in Fig.2.13, where we see one very large comb region (red rectangle) characterized also by the presence of linear chirped regime, since $\epsilon_c < 10^{-1}$ for all the current values in this region. The maximum number of locked modes is $N_{10} = 61$ found at $I/I_{thr} = 2.16$; the corresponding AM and FM dynamics at this bias current, shown in Fig.2.14, shows shorter pulses and markedly linear chirp as compared to Fig.2.9.

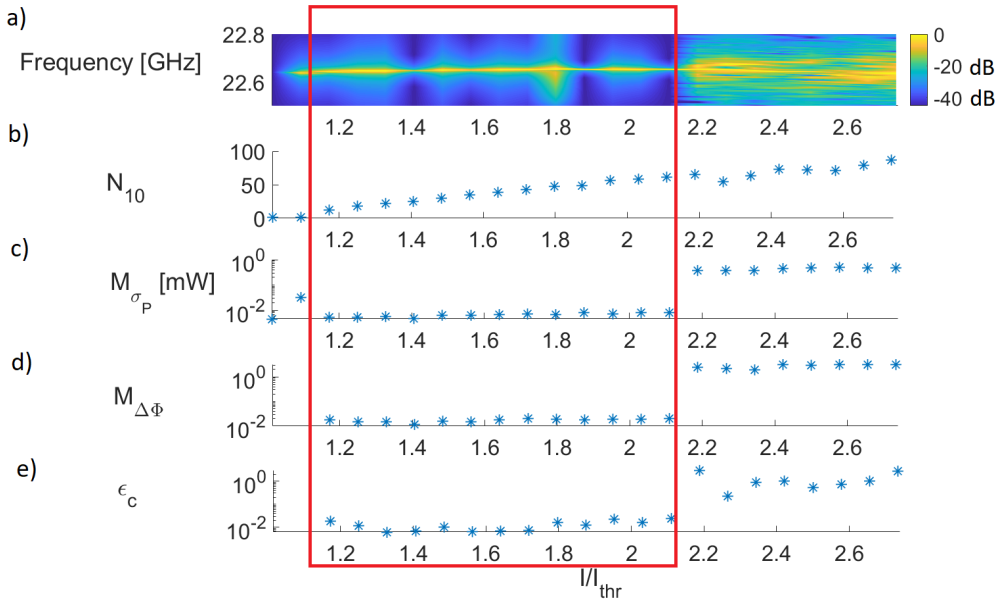

Figure 2.13: a) Power spectrum map for the case $\tau_e = 0.2ps$ with carrier grating. b) Number of modes in the -10dB band as a function of the current. c) M_{σ_P} and d) $M_{\Delta\Phi}$ as functions of the ratio between bias current and threshold current. e) Chirp quantifier for the first $N_c = 5$ Fourier coefficients of the instantaneous frequency signal. Reproduced from [63].

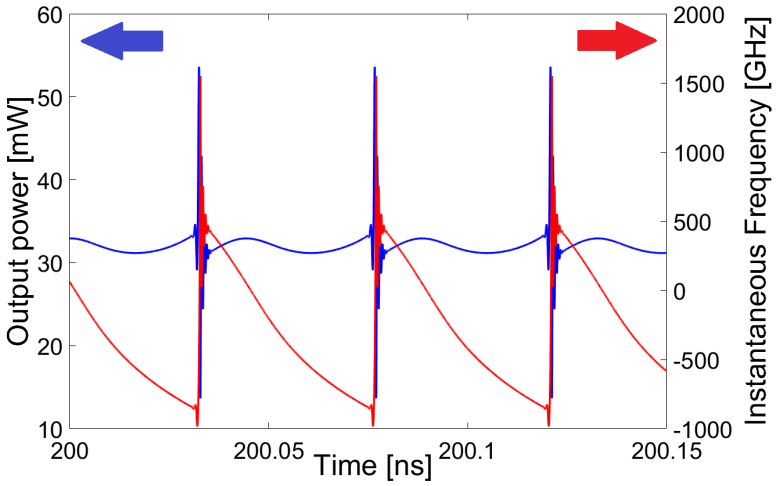

Figure 2.14: Locked regime for $I/I_{thr} = 2.16$, with $\alpha = 0.4$, $\delta_{hom} = 3.18THz$ and $\tau_e = 0.2ps$. Other parameters as in Table 1. Temporal evolution of laser power (blue curve) and instantaneous frequency (red curve). Reproduced from [63].

Finally Fig. 2.15 reports the map for $\tau_e = 0.2ps$ in the parameter space $\alpha \in (0.4, 1)$ and $\delta_{hom} \in$ (3.18THz, 5.74THz); for each parameter configuration the bias current has been scanned between I_{thr} and $3I_{thr}$, with current step $0.08I_{thr}$ of $100mA$. The other values are those in Table 1. For $\alpha = 0.4$ we find locked cases for all the considered values of δ_{hom}. The wider bias current range for OFC corresponds to $\delta_{hom} = 3.18$THz and the highest number of locked modes is achieved with a FWHM gain linedwith of 6.47THz. Locked states are found also for a higher (and probably more realistic) value of $\alpha = 0.7$, whereas locking is completely lost for $\alpha = 1$. The trend is similar to the one in Fig.2.11: the increase of the LEF causes a reduction of N_{10} as well as a reduction of the bias current range of OFC operation.

2.3 Conclusions

A numerical study focused on the multi-mode dynamics of QCLs have been performed, based on the ESMBEs. We outlined the main experimental achievements, such us the linear chirp behaviour in the comb regimes, the presence of intensity structures and the alternance between locked and unlocked states. In our study also the role of some parameters appearing in the ESMBEs, such as the alpha-factor, the homogeneous gain bandwidth and carrier lifetime, was investigated and specified. We found out that increasing the value of alpha-factor there is an enhancement of the phase-amplitude coupling, as well as of the modal competition, so that for the same values of the other parameter the achievement of the comb regimes results

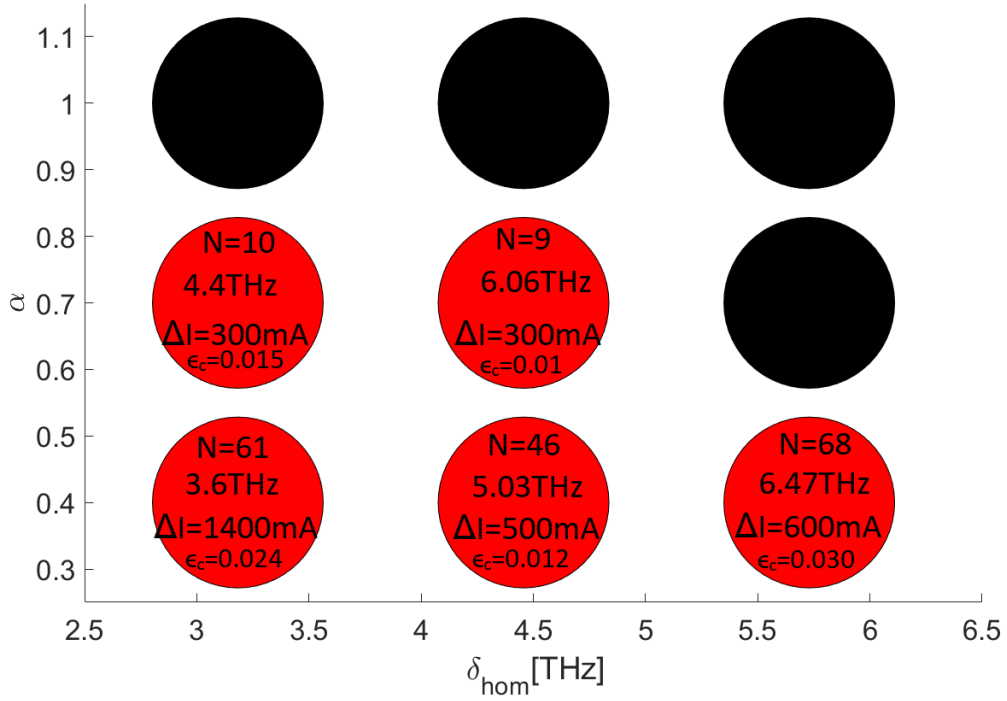

Figure 2.15: Case $\tau_e = 0.2ps$: analysis of locked regimes upon variation of parameters δ_{hom} and α. Black dots indicate that no locked regime could be found upon scanning the pump current in the interval $((I_{thr}, 3I_{thr})$. Red dots indicate parameter pairs where such regime could be found. In the dots the FWHM gain bandwidth (see text) in THz is reported along with the current range where locking was found, the corresponding value of N_{10} and ϵ_c. Reproduced from [63].

more difficult and the locking current interval reduces. Furthermore, an increase of the gain/dispersion bandwith produces a higher number of modes in the optical spectrum. The carrier lifetime also relevantly influences the features of the combs. In fact by reducing the carrier lifetimes, a relevant increase of the number of modes, an increase of the locking current interval and also a chirp behaviour closer to an ideal sawtooth signal, are reported.

Chapter 3

Multi-Mode Dynamics of Ring Quantum Cascade Laser

This Chapter is dedicated to the study of multi-mode dynamics of QCLs in ring configuration, in order to analyze their dynamics and characterize OFC self generation.
In Sec. 3.1 a general overview about the state of the art related to the most recent research in this topic is presented, in order to give motivation to the following original part of the chapter. In Sec. 3.2 the model of ESMBEs for a ring QCL is introduced and some significant simulation results are presented, with a part related to a comparison with the dynamics in the FP case. Specifically, we found that by exploiting the same parameters used to simulate a FP QCL, except than for α factor and length of the cavity, we can confirm again the alternation between locked and unlocked states, and it is also frequent to find comb regimes of harmonic type, with optical spectra characterized by mode separation of a multiple of the FSR [53], [32].
In Sec. 3.3 a reduced model consisting of a single master equation is derived. This model is suited to describe the ring QCL in the limit of fast carrier dynamics and near threshold operation. The instability of the single mode solution in this model is studied and the predicted domains of multi mode emission are compared to the full model case. In particular, simulation results evidences that the model is capable to reproduce all the dynamical regimes found with the full model and also an agreement (even much above threshold) has been found between full and reduced model, in terms of type of emission: in almost the totality of the analyzed cases, for the same value of the parameters, both the models report continuous wave regime or regular and chaotic multi-mode regime, when the pump current is varied.

3.1 Introduction and motivation

The ring cavity is characterized by a different configuration respect to FP. In Fig. 3.1 a scheme of ring configuration is presented. The shape of the waveguide

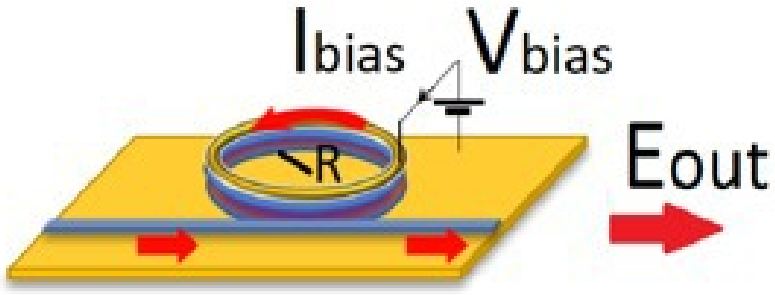

Figure 3.1: Scheme of a ring configuration for a QCL.

is circular with radius R, and in this scheme there is no superposition of forward and backward field, as in the FP cavity, but a single propagating electric field can be considered. More specifically, there is no coupling between the clockwise and counterclockwise waves propagating in the cavity, when defects or generic reflection points are not present in the laser cavity, so that no element of the system can break its natural circular symmetry; devices of this type have been realized, with unidirectional lasing [50].
Another relevant feature of the ring cavity, which establishes a significant difference with the FP scheme, is the absence of Spatial Hole Burning (SHB). In Chapter 2 we analyzed the effect of SHB in the generation of OFC in the case of a FP QCL, which has also been analyzed in depth from experimental and theoretical point of view, as reported in a vast literature [65], [63]. Therefore it is interesting to study the generation of OFCs in a configuration where SHB is negligible or not present, in order to underline possible differences in the characteristics of the combs.
In particular, a vast literature reported studies about the generation of combs in passive (i.e. lacking a bias current) ring microresonator, where the single-mode destabilization occurs because of the concomitance of resonator dispersion and Kerr nonlinearity of the exploited crystal (the materials commonly used are Si, MgF_2, SiO_2, and Si_3N_4) [34]. In two-levels ring lasers it is known that when the pumping parameter reaches values that are several multiples of the threshold (between 9 and 14) a multimode instability occurs [38],[60]. In QCLs, which are characterized by an ultrafast dynamics of the carriers, we have instability of the single mode wave at low pumping levels. It has been shown that this instability shares a common origin with other instabilities found in different types of physical systems

and areas of the physics, as hydrodynamics, superconductors and Bose-Einstein condensates. Specifically, it is related to a CW phase turbulence predicted by the Complex Ginzburg Landau equation [50]. In ring QCLs, this instability which occurs at low pumping levels is due to the presence of a linewidth enhancement factor, which provides a phase-amplitude coupling of the electric field propagating in the ring. Therefore, an interplay between waveguide dispersion and nonlinearity occurs, producing a destabilization of the continuous wave emission and therefore a locking between the modes due to the 4-wave mixing occurring in the laser heterostructure.

The phase turbulence which produces OFC in ring QCLs has become object of study from an experimental and a theoretical point of view only recently [50], [51]. Previously QCL devices with ring-shaped geometry have been investigated, but without any attempt to generate and analyze the self-generation of OFCs [46].

In [46], which is one of the pioneeristic works about this configuration, a characterization of a single mode-emitting ring-QCL illustrated in Fig. 3.2 is performed, with details about its fabrication and analysis of its temperature-dependent wavelength tuning. Later, multi-mode dynamics of QCLs have been studied in an external ring cavity [82], [59], an example setup of which can be seen in Fig. 3.3. In particular, the achievement of the production of ultrashort light pulses and OFCs are generated by exploiting active mode-locking in external cavities, where the current is modulated at round trip frequency [59]. These dynamical regimes are stable and an example is shown in Fig. 3.4, together with the modulated current. In this case, in fact, we have a sequence of pulses obtained by modulating the current in the proximity of the round-trip frequency. The setup exploited for the experiment is the one shown in Fig. 3.3.

The passage from an external ring cavity to a monolithic ring-QCL has allowed the study of self-generated OFCs in these devices. In [50] a fabricated ring QCL in a ridge waveguide geometry is exploited. This device operates in the mid-infrared range at room temperature under constant electrical injection. As in the FP, the emission presents a multimode regime slightly above the threshold, and the optical spectrum presents less modes respect to FP case, with separation equal to the FSR. In Fig. 3.5 a characteristic experimental optical spectrum is shown. We can notice that the number of modes in the -10dB band is 5 and, furthermore, it is interesting the shape of the spectrum: while in the FP both experiments and theory evidence an essentially flat spectrum, in the case of the ring QCL, the envelope of the spectrum follows a $sech^2$ trend [50], [42] (see the black line in Fig. 3.5 fitting the optical spectrum (red line) and see also [43]). Interestingly, this $sech^2$ envelope is known to be characterizing the temporal soliton, since the optical spectrum corresponding to this type of regime is characterized by a sequence of lines enveloped by a $sech^2$ function. The formation of temporal solitons described by the LLE is the spatiotemporal equivalent of the frequency combs and governs their features.

Another feature specific of this device, emerging from the experiments, is that, for

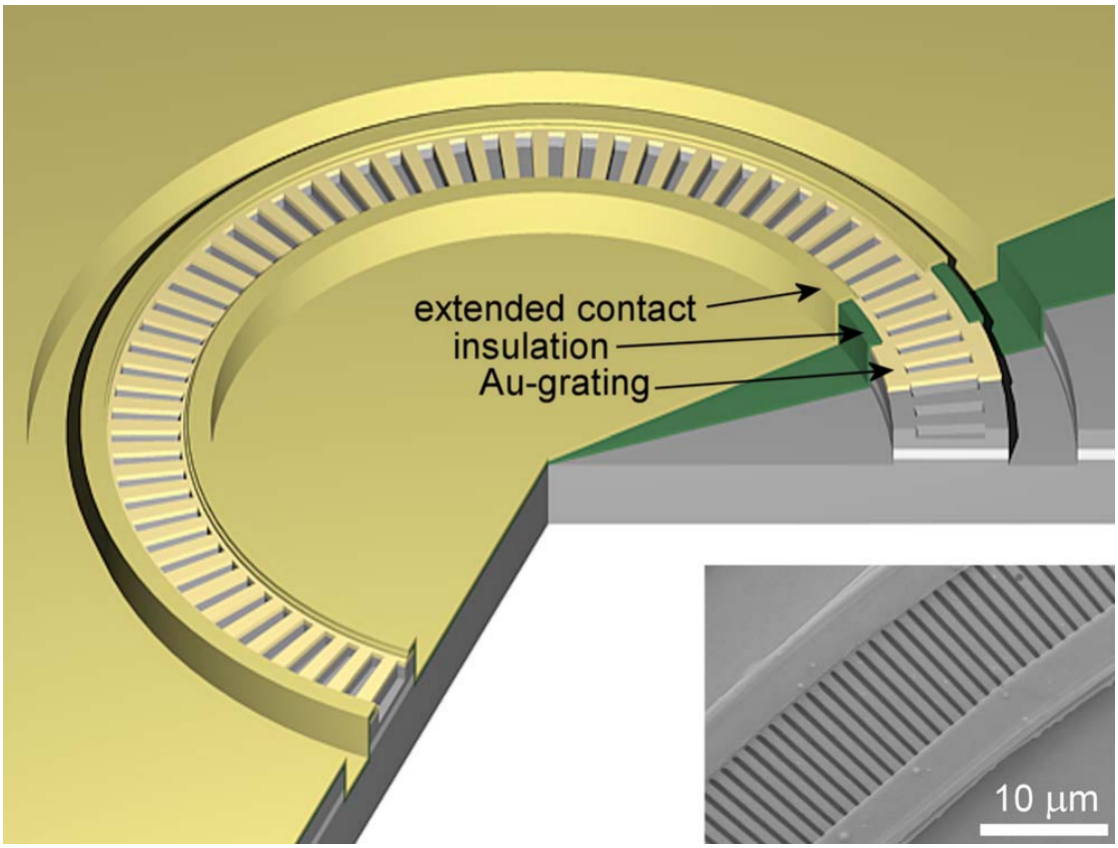

Figure 3.2: Three-dimensional illustration of a surface-emitting ring QCL. The inset shows a scanning electron microscopy image of a waveguide section holding the etched second-order DFB gratings to provide surface emission. Reproduced from [46].

increasing values of the pump, one observes the occurrence of multimode emission ranges, followed by a new window where the singlemode (CW) emission returns stable [30]. This trait of the behaviour of the laser has not been found for FP cavities.
The invention and the improvement of the SWIFTS technique [8] has enabled the possibility to reconstruct the temporal dynamics with high precision [43]. In Fig. 3.6 an example of reconstructed power trace for a laser emiting in the mid-IR is shown, characterized by the presence of regular repetition of structures which have the shape of power bumps. Each structure is composed by a main peak and a secondary one and there is no evidence of a constant background power between two adjacent structures.
Recently also multi-mode regimes generated by ring lasers emitting in the THz region have been deeply studied and analyzed from both theoretical and experimental point of view,evidencing an alternance between Harmonic combs, dense

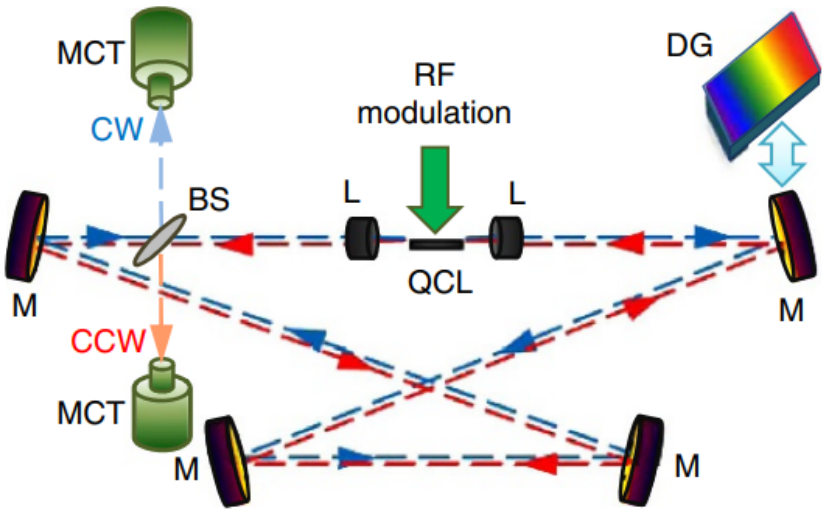

Figure 3.3: Optical set-up of free-space external ring cavity QCL. BS, beam splitter; CCW, counter clockwise direction; CW, clockwise direction; DG, diffraction grating; L, aspheric lenses; M, mirrors; MCT, detector; QCL, quantum cascade laser. Reproduced from [59].

combs, single-mode regimes, and chaotic regimes all found by sweeping the bias current [30]. The dense comb regime is characterized by a spectrum consisting of a number of modes one order of magnitude higher than in the mid-IR case.
The theoretical explanation of the experimental achievements have been performed by using a set of Maxwell-Bloch equations [30]. Further models based on this formalism have been proposed in order to explore the multi-mode dynamics of QCL with ring cavity. In particular, a model based on a self-consistent approach encompassing the main characteristic of semiconductors, has been used to obtain simulation results that would help to understand the features of combs emitted by ring QCLs [13]. This model, which we will exploit in the next section of this Chapter in order to obtain the presented simulation results, is obtained by adapting the ESMBEs retrieved in Chapter 2 and in in [63] to the ring configuration. In [13] dense and harmonic combs have both been obtain by integrating this model, as well as alternation between locked and unlocked states. In this work we focus on the detailed investigation of the HFC regimes, and we classify them by using the indicators introduced in Sec. 2.2.2. Moreover, a study of the instantaneous frequency of the locked regimes is introduced in this work, underlining the differences respect to the combs generated in a FP configuration.
Furthermore, the QCL ring configuration in presence of an injected optical field have attracted growing interest in recent years, with several papers on this topic [12], [57], [56]. Such systems have been considered in order to obtain temporal

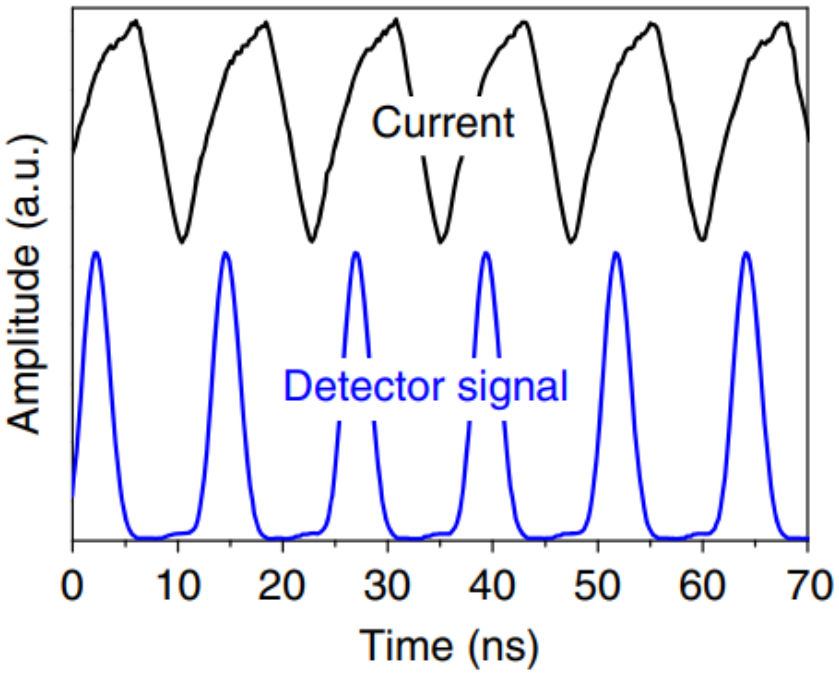

Figure 3.4: Experiment: periodic emission pulses and driving modulated near the round-trip frequency for the external cavity QCL setup of Fig. 3.3. Reproduced from [59].

solitons, therefore combs, in analogy to the study performed in passive microresonators with injected field [34]. These devices are able to support the propagation of particular types of global and localized temporal structures: Turing roll patterns (see Fig. 3.7(a)), temporal solitons (see Fig. 3.7.c)), and localized structures characterized by several adjacent peaks separated by a constant background [12], [57]. The relation between the output intensity of the laser and the intensity of the injected field can be represented by an s-shaped curve for a suitable choice of the operational parameters. In this case the system will show an hysteretic behaviour, as shown in Fig. 3.7(b). In [12] a formal unification of frequency combs in active and passive systems has also been performed, by proposing a model based on a generalized form of the Lugiato-Lefever Equation (LLE). The same equation can provide the description of the generation of OFCs in passive microresonators and in ring QCLs in presence of drive, showing also in this second case the existence of temporal solitons.

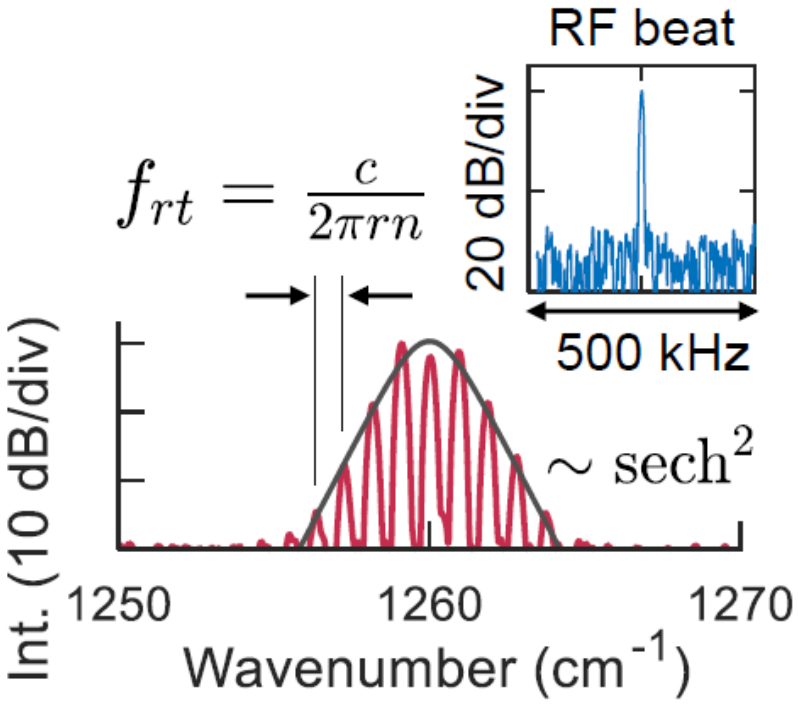

Figure 3.5: Optical spectrum of a ring QCL frequency comb. Also shown is the narrow (< 1 kHz) electrical beat note of the laser (central frequency 27.8 GHz). Reproduced from [50].

3.2 Effective Semiconductor Maxwell-Bloch Equations for Ring Quantum Cascade Laser

This section is dedicated to the retrieval of the ESMBEs for a QCL in the ring configuration. This model have been previously proposed in [13], where its derivation has been performed *ab initio* following a procedure analogous to the retrival of the ESMBEs for the FP case explained in Chapter 2. Let us consider a total length of the cavity L of few millimiters. It is possible to retrieve this system of equations starting from the ESMBEs for the FP configuration, Eqs. 2.22-2.27, and implementing the hypotheses specific of the ring configuration. In particular, in a ring resonator we assume that only the forward field is propagating (ie: clockwise mode). This is true under the assumption of no defects or any other asymmetries that excites the counter clockwise mode. This implies:

$$E^{-} = 0 \tag{3.1}$$

$$P_0{}^{-} = 0 \tag{3.2}$$

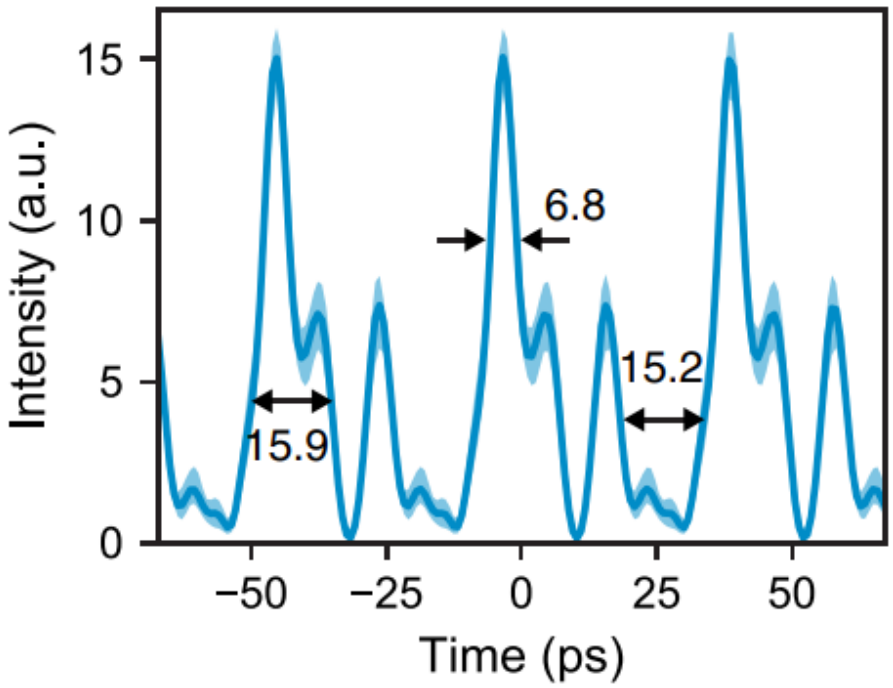

Figure 3.6: Reconstructed temporal intensity of a mid-IR ring QCL output power, by exploiting the SWIFTS technique. Reproduced from [43].

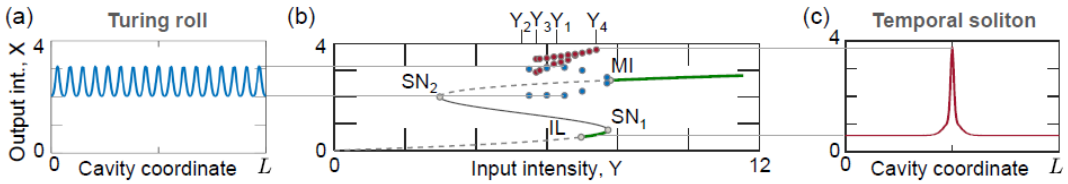

Figure 3.7: Dynamics of a driven ring QCL: (a) Turing rolls oscillating between two intensities, which constitutes a pair of blue dots in (b). (b) S-shaped curve of output intensity X vs. input intensity Y. (c) A Cavity Soliton whose peak corresponds to a red dot of (b). Reproduced from [12].

Therefore, since we do not have standing wave into the cavity, also the carrier grating (i.e. the SHB) is not present and we can eliminate the dynamical variables that describe this carrier grating, imposing into Eqs. 2.22-2.27:

$$N_1^+ = 0 \tag{3.3}$$
$$N_1^- = 0 \tag{3.4}$$

We remove the superscript +, since it is not necessary to distinguish between forward and backward field, as in the FP case. We obtain then:

$$\frac{\partial E}{\partial z} + \frac{1}{v}\frac{\partial E}{\partial t} = -\frac{\alpha_L}{2}E + gP_0, \tag{3.5}$$

$$\frac{\partial P_0}{\partial t} = \frac{(1+i\alpha)}{\tau_d}\left[-P_0 + if_0\epsilon_0\epsilon_b\left(1+i\alpha\right)N_0E\right], \tag{3.6}$$

$$\frac{\partial N_0}{\partial t} = \frac{I}{eV} - \frac{N_0}{\tau_e} + \frac{i}{4\hbar}\left[E^*P_0 - EP_0{}^*\right]. \tag{3.7}$$

$$\tag{3.8}$$

Finally, the model equations must be completed by the boundary condition which reads:

$$E(0,t) = \sqrt{R}E(L,t), \tag{3.9}$$

where R is the reflectivity of the ring [9].
Eqs. 3.5-3.7 with boundary condition Eq. 3.9 constitute the ESMBEs for ring configuration. This model has been derived by exploiting the semiconductor susceptibility defined in Eq. 2.13, encompassing therefore relevant characteristics of the semiconductor media, as the inclusion of α factor, the asymmetric gain profile, the dependence of the susceptibility from the carrier density. In the following subsection we will report the numerical integration of this model and the most significant numerical results.

3.2.1 Numerical results

In this subsection we present the results obained by performing several simulation streams, through the integration of Eqs. 3.5-3.7 with boundary condition (3.9) for the QCL in ring configuration, and assuming the same parameters used in the study of the FP QCL, which will allow for a comparison between these two lasers [64]. The code exploited for integration of the Differential equations is based on a finite differences scheme, discretizing both in time and space.
In the following table we report the values of these parameters.

Table 2. Parameters for QCL in ring configuration.

n	L(μm)	R	τ_e(ps)	Γ_c	f_0(μm^3)	V(μm^3)	N_p	λ_0(μm)
3.3	4000	0.3	1	0.3	$1.1*10^{-7}$	2240	50	10

In Table 2 the same values of Table 1 are reported, except than the length of the cavity L, which is 4000μm instead of 2000μm, in order to have the same FSR of

the FP case (FSR=22.4 GHz). By keeping fixed the values of parameters in Table 2, we considered different values of α and Γ (δ_{hom}) and for each couple (α, δ_{hom}) a current scan was performed between the threshold current I_{thr} and $4I_{thr}$ with steps of $0.3I_{thr}$. For all the simulation I_{thr}=175mA.
The first results we show are for α=1.5 and different values of δ_{hom}, because in these cases we found a multi-mode dynamics with regular (locked) regimes.
Let us consider the case corresponding to δ_{hom}=1.6THz. In this case we report the presence of locked and chaotic dynamics, with some specific difference respect to the FP results. In Fig. 3.8 a regular (locked) regime is shown: it presents 4 structures

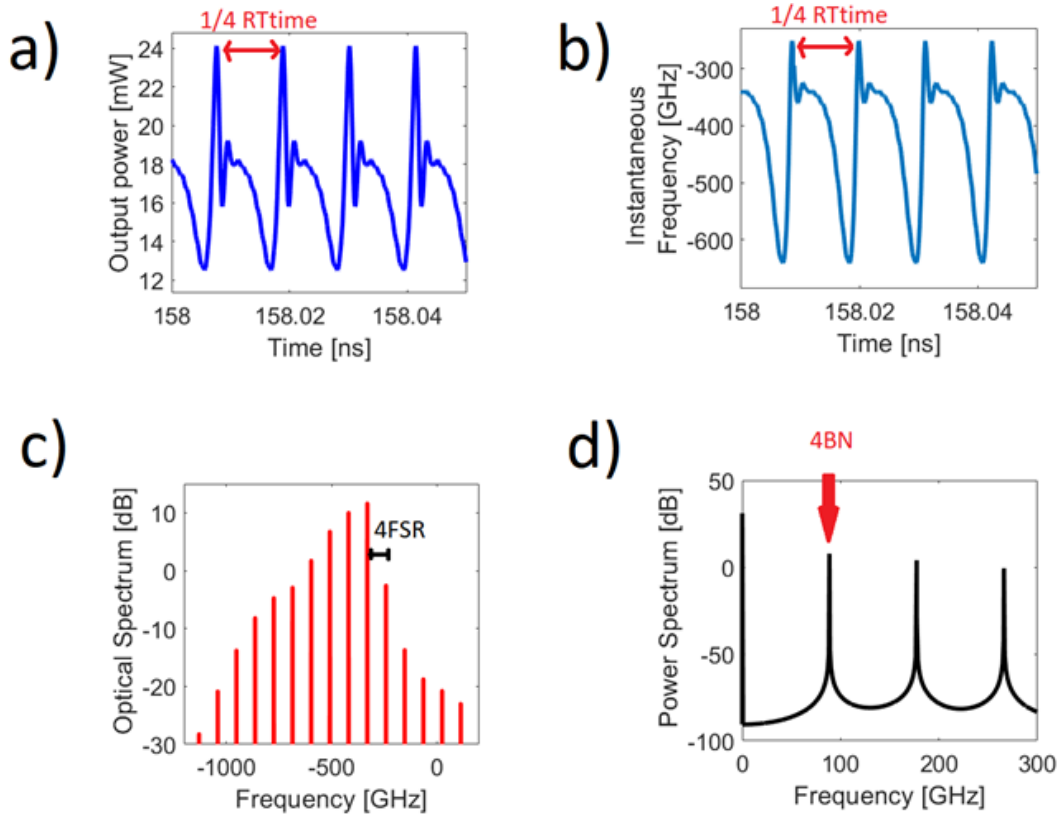

Figure 3.8: Case α=1.5, δ_{hom}=1.6THz, I/I_{thr}=2.3: locked regime with 4 structures per roundtrip. a) Power-time trace. b) Instantaneous frequency as a function of the time. c) Optical Spectrum and d) Power Spectrum. The BN frequency is the FSR 22.4GHz

per RT in the power and instantaneous frequency traces (Fig. 3.8.a) and b)). We can notice that the power structures have a shape similar to the ones found in the FP case, while the instantaneous frequency is not characterized by linear chirp as for the FP. Another relevant difference with the FP is the fact that we observe 4 structures per RT time (about 48ps), while all the simulations in the FP case were

characterized by 1 structure per RT time. Furthermore, it can be noticed that the separation between two adjacent modes in the optical spectrum is a multiple of the FSR (n=4) and no secondary peaks are detected (Fig. 3.8 c)). Moreover, the RF spectrum (Fig. 3.8.d)) is characterized by peaks occurring for value of the frequency which are multiple of 4BN, where BN is the beat note frequency equal to 22.4GHz, without secondary peaks. This scenario is in agreement with the definition of Harmonic Frequency Comb and their experimental demonstration [53], [32].

If we increment the value of δ_{hom}, setting it to δ_{hom}=2.24THz keeping fixed

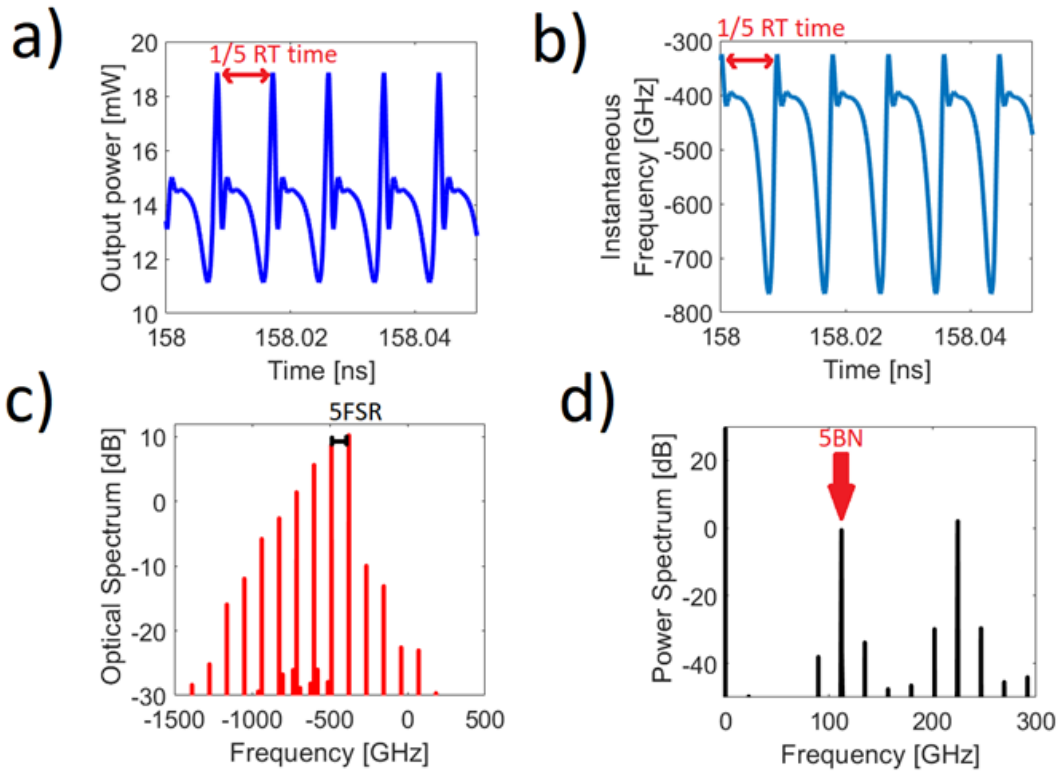

Figure 3.9: Case α=1.5, δ_{hom}=2.24THz, I/I_{thr}=2: locked regime with 5 structures per roundtrip. a) Power-time trace. b) Instantaneous frequency as a function of the time. c) Optical Spectrum and d) Power Spectrum.

all the other parameters, we find new OFC regimes, which present ananlogous characteristics to the regime shown in Fig. 3.9. The general scenario presented in this figure reproduces the picture of Fig. 3.8, with the exception that the Power trace (Fig. 3.8.a)) presents 5 structures per roundtrip, the modes in the OS are separated by 5 FSR (Fig. 3.8.c)) and the main peaks in the RF spectrum are occurring at 5BN(Fig. 3.8.d)). We have therefore an harmonic frequency comb of 5th order. Also for this value of δ_{hom} we do not find any evidence of linear frequency

chirp (Fig. 3.8.b)).

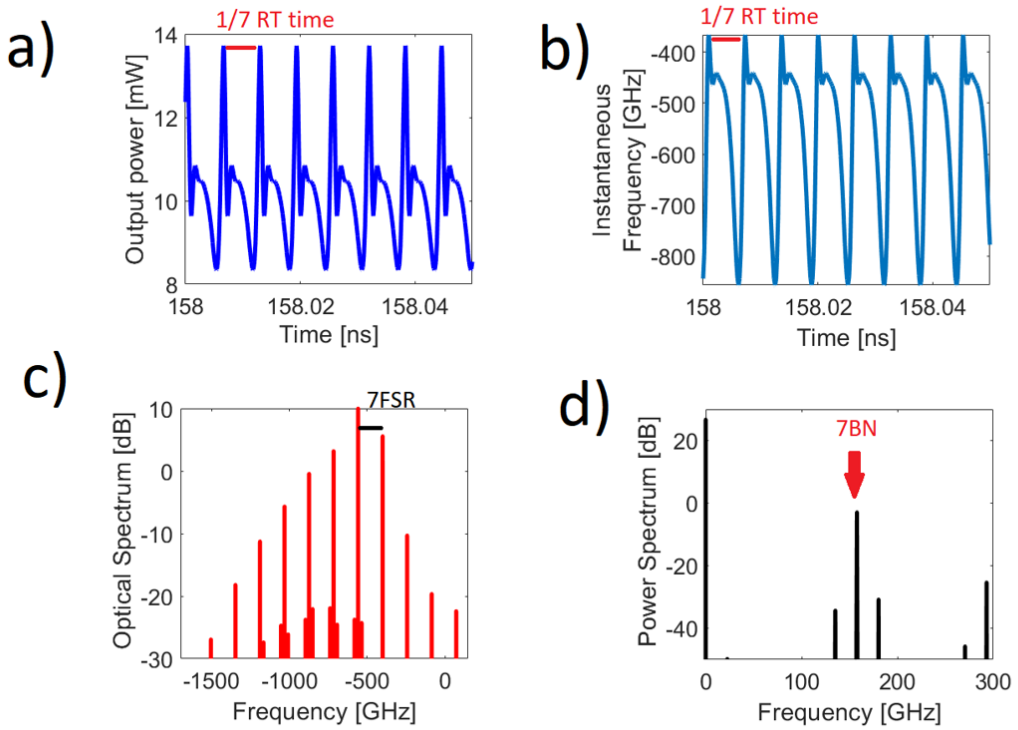

Figure 3.10: Case α=1.5, δ_{hom}=2.88THz, I/I_{thr}=1.7: locked regime with 7 structures per roundtrip. a) Power-time trace. b) Instantaneous frequency as a function of the time. c) Optical Spectrum and d) Power Spectrum.

By further increasing δ_{hom} to the value 2.88THz we obtain a locked case with 7 structures per roundtrip, shown in Fig. 3.10. We can therefore notice that, as a general trend, the maximum number of structures per roundtrip in the power/frequency trace (or equivalently the number of FSR between two adjacent modes in the OS) tends to increase by increasing δ_{hom}. Moreover, the instantaneous frequency trace follows the same trend in correspondence of different values of δ_{hom}, without evidence of linear chirp. In Fig. 3.11 a typical current scan is shown, corresponding to the case $\delta_{hom} = 2.88THz$. In this plot the comb region is underlined in red, determined by considered low values of the quentifiers of amplitude and phase noise as done in previous chapter for the FP configuration. Some differences can be noticed respect to the analogous case in the FP configuration. Firsly, the OFC regimes are characterized by a number of locked modes around 5, therefore quite less than the 15 locked modes that we observed in the FP. Furthermore the chirp indicator is quite larger than the threshold identified in order to recognize linear chirped

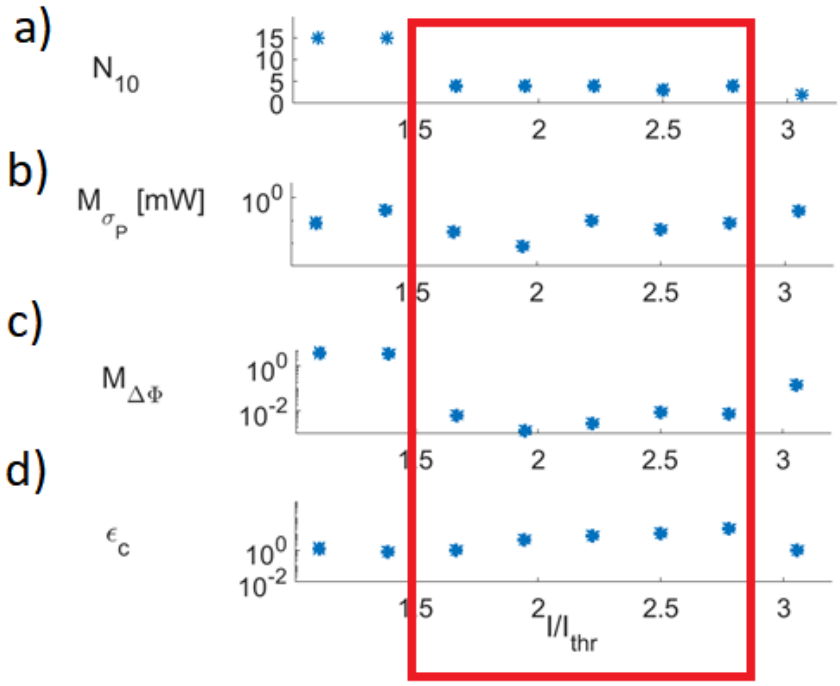

Figure 3.11: Results of simulations for a current scan from ring QCL threshold I_{th} to $3I_{th}$ for $\alpha = 1.5$, $\delta_{hom} = 2.88THz$. Other parameters as in Table 2. a) Number of modes in a -10dB spectral bandwidth; (b) amplitude and (c) phase noise quantifiers for the N_{10} modes, as introduced in 2; (d) chirp quantifier for the first $N_c = 5$ Fourier coefficients of the instantaneous frequency signal, as introduced in 2. The region of OFC operation highlighted with a red rectangular box can be identified.

regimes, so that no chirped regime can be observed in a full current scan. This behaviour is confirmed also for different values of $\delta_{hom} = 2.88THz$.
By performing a more focused investigation of these HFC regimes, we did not find a complete sequence (with "complete sequence" we mean the number of FSR between two consecutive peaks in the OS following the sequence of consecutive integers for increasing value of $\delta_{hom} = 2.88THz$). Furthermore, by fixing all the parameters and by varying only the bias current in proximity a found HFC regime, we did not find another regime of this type.
In conclusion, considering the performed sets of simulations, we found alternance between locked and unlocked states, as shown in Fig.3.11, which is an example of current scan, as we found in the FP case. The most relevant difference between the

results for FP and ring, is the absence of chirped frequency in the ring case, that therefore makes this a characteristic fingerprint of the FP configuration.

3.3 Reduced Model for Ring Quantum Cascade Laser

We want to retrieve a reduced model for the ring configuration, by assuming the hypotheses of near threshold operation and fast carriers. The aim of this section is to analyze the stability of the predicted CW states and to verify the consistence of the model respect to the implemented hypotheses. This method, in fact, appears more suitable for a Linear Stability Analysis (LSA) and therefore it is more convenient in order to understand the parameters which destabilize the CW emission. We remark that the LSA predicts the destabilization of the CW, but does not give information about the type of multimode regimes that are achieved when this destabilization occurs.

3.3.1 Retrieval of the model

This section is dedicated to describe the mathematical treatment aimed to derive the reduced model. Let us first consider the equation for the electric field, Eq. 3.5. We multiply both sides of this equation by the group velocity v, obtaining:

$$v\frac{\partial E}{\partial z} + \frac{\partial E}{\partial t} = -v\frac{\alpha_L}{2}E + vgP_0 \tag{3.10}$$

Then we define photon lifetime as:

$$\tau_p = (v\alpha_L/2)^{-1} \tag{3.11}$$

Multiplying both sides of Eq. 3.10 by the polarization dephasing time τ_d and introducing also the definition given by Eq. 3.11 we obtain:

$$v\tau_d\frac{\partial E}{\partial z} + \tau_d\frac{\partial E}{\partial t} = -\frac{\tau_d}{\tau_p}E + \tau_d vgP_0 \tag{3.12}$$

At this point we introduce the following dimensionless space and time variables:

$$\eta = \frac{z}{v\tau_d}, \tag{3.13}$$

$$t' = \frac{t}{\tau_d} \tag{3.14}$$

and the parameter σ, which is the ration between the dephasing time and the photon lifetime:

$$\sigma = \frac{\tau_d}{\tau_p} \tag{3.15}$$

We have, then:

$$\frac{\partial E}{\partial \eta} + \frac{\partial E}{\partial t'} = \sigma \left[-E + \tau_p v g P_0^+ \right] \tag{3.16}$$

Now let us consider and manipulate the equations for polarization and carriers. First we consider Eq. 3.6, for the polarization envelope P_0. Let us multiply both the sides of this equation by τ_d. We obtain:

$$\frac{\partial P_0}{\partial t'} = \frac{(1+i\alpha)}{\Gamma} \left[-P_0 + i f_0 \epsilon_0 \epsilon_b (1+i\alpha) N_0 E \right] \tag{3.17}$$

Then we consider Eq. 3.7, for the carrier envelope N_0, and also in this case we multiply both sides of this equation by τ_d:

$$\frac{\partial N_0}{\partial t'} = \frac{I\tau_d}{eV} - \frac{\tau_d N_0}{\tau_e} + \frac{i\tau_d}{4\hbar} \left[E^* P_0 - E P_0{}^* \right]. \tag{3.18}$$

Let us define:

$$b = \frac{\tau_d}{\tau_e}, \tag{3.19}$$

$$n_0 = N_0 V \tag{3.20}$$

Eq. 3.18 becomes:

$$\frac{\partial n_0}{\partial t'} = b \left[\frac{I\tau_e}{e} - n_0 + \frac{iV\tau_e}{4\hbar} \left(E^* P_0 - E P_0{}^* \right) \right] \tag{3.21}$$

We consider now Eq. 3.17 and we introduce:

$$f_0' = \frac{f_0}{V} \tag{3.22}$$

and we obtain:

$$\frac{\partial P_0}{\partial t'} = \frac{(1+i\alpha)}{\Gamma} \left[-P_0 + i f_0' \epsilon_0 \epsilon_b (1+i\alpha) n_0 E \right] \tag{3.23}$$

At this point we introduce the new dimensionless dynamical variables:

$$F = \sqrt{\frac{V\tau_e f_0' \epsilon_0 \epsilon_b}{4\hbar}} E, \tag{3.24}$$

$$p = i\sqrt{\frac{V\tau_e f_0' \epsilon_0 \epsilon_b}{4\hbar}} P_0, \tag{3.25}$$

$$d_0 = f_0' \epsilon_0 \epsilon_b n_0, \tag{3.26}$$

$$\tag{3.27}$$

and the the pump parameter:

$$\mu = f_0' \epsilon_0 \epsilon_b \frac{I \tau_e}{e} \tag{3.28}$$

We can write then the equations for p and d_0:

$$\frac{\partial p}{\partial t'} = \frac{(1+i\alpha)}{\Gamma}\left[-p^+ - (1+i\alpha)\, d_0 F\right], \tag{3.29}$$

$$\frac{\partial d_0}{\partial t'} = b\left[\mu - d_0 + F^* p + F p^*\right] \tag{3.30}$$

$$\tag{3.31}$$

We introduce now quantity:

$$A = \frac{v \tau_p \omega_0 N_P \Gamma_C}{2 \epsilon_0 n c} \tag{3.32}$$

and rewrite the equation for the field:

$$\frac{\partial F}{\partial \eta} + \frac{\partial F}{\partial t'} = \sigma\left[-F - Ap\right] \tag{3.33}$$

Finally, if we recall:

$$P = Ap \tag{3.34}$$

$$D_0 = A d_0 \tag{3.35}$$

$$\tag{3.36}$$

we can rewrite the ESMBEs as:

$$\frac{\partial F}{\partial \eta} + \frac{\partial F}{\partial t'} = \sigma\left[-F - p\right] \tag{3.37}$$

$$\frac{\partial P}{\partial t'} = \frac{(1+i\alpha)}{\Gamma}\left[-P - (1+i\alpha)\, D_0 F\right], \tag{3.38}$$

$$\frac{\partial D_0}{\partial t'} = b\left[\mu - D_0 + F^* P + F P^*\right] \tag{3.39}$$

$$\tag{3.40}$$

We suppose valid the low transmissivity approximation, so that τ_p also accounts for the transmission losses.
At this point we introduce the smallness parameter

$$\epsilon = \sqrt{\sigma} \tag{3.41}$$

and we assume fast carriers and near threshold operation. Consistently with these assumptions, we can write:

$$F = \varepsilon\ F^{(1)} + O(\varepsilon^2) \tag{3.42}$$
$$P = \varepsilon\ P^{(1)} + O(\varepsilon^2) \tag{3.43}$$
$$D_0 = 1 + \varepsilon^2 D_0^{(2)} + O(\varepsilon^3) \tag{3.44}$$
$$\mu = 1 + \varepsilon^2 \mu^{(2)} + O(\varepsilon^3) \tag{3.45}$$

The expansion of μ in Eq. 3.45 corresponds to the implementation of the hypothesis of near threshold operation. Furthermore, in order to have derivatives of order O(1), we assume that the following Taylor expansions hold:

$$\frac{\partial}{\partial t'} = \frac{\partial}{\partial t'^{(0)}} + \varepsilon^2 \frac{\partial}{\partial t'^{(2)}} + O(\varepsilon^3) \tag{3.46}$$
$$\frac{\partial}{\partial \eta} = \frac{\partial}{\partial \eta^{(0)}} + \varepsilon^2 \frac{\partial}{\partial \eta^{(2)}} + O(\varepsilon^3) \tag{3.47}$$

By introducing the expansion Eq. 3.46, we can rewrite the equation Eq. 3.37 for the electric field:

$$\varepsilon \frac{\partial F^{(1)}}{\partial \eta^{(0)}} + \varepsilon^3 \frac{\partial F^{(1)}}{\partial \eta^{(2)}} + \varepsilon \frac{\partial F^{(1)}}{\partial t'^{(0)}} + \varepsilon^3 \frac{\partial F^{(1)}}{\partial t'^{(2)}} = \varepsilon^2 \left[-\varepsilon\ F^{(1)} - \varepsilon\ P^{(1)} \right] \tag{3.48}$$

At first order in ϵ we have:

$$\frac{\partial F^{(1)}}{\partial \eta^{(0)}} = -\frac{\partial F^{(1)}}{\partial t'^{(0)}} \tag{3.49}$$

Now let us consider the equation for P, Eq. 3.38 and let us introduce the expansions Eqs. 3.46-3.47 into it. We have at first order in ϵ:

$$\varepsilon \frac{\partial P^{(1)}}{\partial t'^{(0)}} = \frac{(1+i\alpha)}{\Gamma} \left\{ -\varepsilon\ P^{(1)} - (1+i\alpha)\, \varepsilon\ F^{(1)} \right\} \tag{3.50}$$

and then:

$$\left[1 + \frac{1}{\Gamma(1+i\alpha)} \frac{\partial}{\partial t'^{(0)}} \right] \varepsilon P^{(1)} = -\,(1+i\alpha)\, \varepsilon\ F^{(1)} \tag{3.51}$$

If we solve Eq. 3.51 in the Fourier domain we obtain:

$$\left[1 + \frac{i\omega}{\Gamma(1+i\alpha)} \right] \hat{P}^{(1)} = -\,(1+i\alpha)\ \hat{F}^{(1)} \tag{3.52}$$

By introducing the additional hypothesis that $\omega/\Gamma << 1$:

$$P^{(1)} = -\,(1+i\alpha)\ F^{(1)} \tag{3.53}$$

Using Eq. 3.53 we get from Eq. 3.39:

$$D_0 \;=\; \mu - 2|F^+|^2 \tag{3.54}$$

By solving in the Fourier domain Eq. 3.38:

$$\left[1 + \frac{i\omega}{\Gamma(1+i\alpha)}\right] \hat{P}^+ = -\,(1+i\alpha)\;\left(D_0 F^{\pm} + D_1{}^{\pm} F^{\mp}\right) \tag{3.55}$$

and using the Taylor expansion of $(1+x)^{-1}$ truncated at the second order, then anti-transforming both sides of the obtained equation, and using Eqs. 3.48 and 3.49 we have:

$$\begin{aligned} &\frac{\partial F}{\partial \eta} + \frac{\partial F}{\partial t\prime} \\ &\quad = \sigma\left[(\mu - 1 + i\alpha\mu)\,F - 2\,(1+i\alpha)\,F|F|^2 + \left(\frac{1}{\Gamma^2\,(1+i\alpha)}\right)\frac{\partial^2 F}{\partial \eta^2}\right] \end{aligned} \tag{3.56}$$

with boundary conditions:

$$F(0,t') \;=\; \sqrt{R}F(L',t'), \tag{3.57}$$

This is the reduced model for the ring cavity, consisting in one spatio-temporal differential equation for the field F.

3.3.2 Steady State solutions

In this subsection we want to calculate the steady state solutions of the Eq. 3.56. Let us assume for the field the continuous wave expression:

$$F \;=\; a_0 e^{-iq\eta + i\omega t'} \tag{3.58}$$

where a_0 is the amplitude of the field, ω the angular frequency expressed in adimensional unit, according to the definition of t', and q is the wavenumber. Substituting Eq. 3.58 in the Eq. 3.56 we obtain:

$$\begin{aligned} &-iqa_0 + i\omega a_0 \\ &\quad = \sigma\left[(\mu - 1 + i\alpha\mu)\,a_0 - 2\,(1+i\alpha)\,a_0|a_0|^2 + \left(\frac{1}{\Gamma^2\,(1+i\alpha)}\right)\left(-q^2 a_0\right)\right] \end{aligned} \tag{3.59}$$

and by simplifying a_0:

$$\begin{aligned} &-iq + i\omega \\ &\quad = \sigma\left[(\mu - 1 + i\alpha\mu) - 2\,(1+i\alpha)\,|a_0|^2 + \left(\frac{1}{\Gamma^2\,(1+i\alpha)}\right)\left(-q^2\right)\right] \end{aligned} \tag{3.60}$$

Taking the real part of Eq. 3.60 we obtain:

$$|a_0|^2 = \frac{1}{2}\left[\mu - 1 - q^2\left(\frac{1}{\Gamma^2\left(1+\alpha^2\right)}\right)\right] \tag{3.61}$$

which gives the laser intensity versus the pump and the continuous wave wavevector. Taking the imaginary part of the equation 3.60 we have:

$$\omega = q + \sigma\alpha\left(1 + \frac{2q^2}{\Gamma^2\left(1+\alpha^2\right)}\right) \tag{3.62}$$

This is the dispersion relation, i.e. the relation between the wavenumber q and the pulsation ω. Eqs. 3.61 and 3.62 are the steady state solutions of Eq. 3.56.

3.3.3 Linear stability analysis

At this point we want to perform the linear stability analysis of the equation 3.56, in order to study the destabilization of the continuous wave solution.
Let us introduce a perturbation in the continuous wave field expression:

$$F = \left(a_0 + \delta a(\eta, t')\right) e^{-iq\eta + i\omega t'} \tag{3.63}$$

Substituting Eq. 3.63 in Eq. 3.56, we obtain:

$$\begin{aligned} -iq\left(a_0+\delta a\right) + \frac{\partial \delta a}{\partial \eta} + i\omega\left(a_0+\delta a\right) + \frac{\partial \delta a}{\partial t'} \\ = \sigma[-\left(a_0+\delta a\right) + \left(1+i\alpha\right)\mu\left(a_0+\delta a\right) - 2\left(1+i\alpha\right)\left|\left(a_0+\delta a\right)\right|^2\left(a_0+\delta a\right) \\ + \left(\frac{1-i\alpha}{\Gamma^2\left(1+\alpha^2\right)}\right)\left(\left(-q^2\right)\left(a_0+\delta a\right) - 2iq\frac{\partial \delta a}{\partial \eta} + \frac{\partial^2 \delta a}{\partial \eta^2}\right)] \end{aligned} \tag{3.64}$$

If we use the steady state solutions Eqs. 3.61 and 3.62 and we neglect the terms with order $O((\delta a)^n)$ with n≥2:

$$\begin{aligned} -iq\delta a + \frac{\partial \delta a}{\partial \eta} + i\omega\delta a + \frac{\partial \delta a}{\partial t'} \\ = \sigma[-\delta a + \left(1+i\alpha\right)\mu\delta a - 2\left(1+i\alpha\right)\left(\left|a_0\right|^2\delta a + a_0^2\delta a^*\right) \\ + \left(\frac{1-i\alpha}{\Gamma^2\left(1+\alpha^2\right)}\right)\left(\left(-q^2\right)\delta a - 2iq\frac{\partial \delta a}{\partial \eta} + \frac{\partial^2 \delta a}{\partial \eta^2}\right)] \end{aligned} \tag{3.65}$$

Let us also consider the complex-conjugate of Eq. 3.65:

$$\begin{aligned} &+iq\delta a^* + \frac{\partial \delta a^*}{\partial \eta} - i\omega\delta a^* + \frac{\partial \delta a^*}{\partial t'} \\ &\quad = \sigma[-\delta a^* + (1-i\alpha)\,\mu\delta a - 2\,(1-i\alpha)\left(|a_0|^2\,\delta a^* + {a_0}^{*2}\delta a\right) \\ &\quad + \left(\frac{1+i\alpha}{\Gamma^2\,(1+\alpha^2)}\right)\left(\left(-q^2\right)\delta a^* + 2iq\frac{\partial \delta a^*}{\partial \eta} + \frac{\partial^2 \delta a^*}{\partial \eta^2}\right)] \end{aligned} \tag{3.66}$$

If we assume the following Fourier expansions:

$$\delta a = \left(\sum_{n=-\infty}^{+\infty} \delta a_{0n} e^{-ik_n\eta}\right) e^{\lambda t} \tag{3.67}$$

$$\delta a^* = \left(\sum_{n=-\infty}^{+\infty} {\delta a_{0n}}^* e^{+ik_n\eta}\right) e^{\lambda t} = \left(\sum_{n=-\infty}^{+\infty} {\delta a_{0-n}}^* e^{-ik_n\eta}\right) e^{\lambda t} \tag{3.68}$$

and we substitute them into Eqs. 3.65-3.66, and using the ortonormality of Fourier basis we get:

$$\begin{aligned} &-iq\delta a_{0n} - ik_n\delta a_{0n} + i\omega\delta a_{0n} + \lambda\ \delta a_{0n} \\ &\quad = \sigma[-\delta a_{0n} + (1+i\alpha)\,\mu\ \delta a_{0n} - 2\,(1+i\alpha)\left(2\,|a_0|^2\,\delta a_{0n} + {a_0}^2\delta {a_{0-n}}^*\right) \\ &\quad + \left(\frac{1-i\alpha}{\Gamma^2\,(1+\alpha^2)}\right)\left(\left(-q^2\right)\delta a_{0n} - 2iq\,(-ik_n)\,\delta a_{0n} - {k_n}^2\delta a_{0n}\right)] \end{aligned} \tag{3.69}$$

and its complex-conjugate:

$$\begin{aligned} &+iq{\delta a_{0n}}^* + ik_n\delta a_{0n}^* - i\omega\delta a_{0n}^* + \lambda\ \delta a_{0n}^* \\ &\quad = \sigma[-\delta a_{0n}^* + (1-i\alpha)\,\mu\ \delta a_{0n}^* - 2\,(1-i\alpha)\left(2\,|a_0|^2\,\delta a_{0n}^* + a_0^{*2}\delta a_{0-n}\right) \\ &\quad + \left(\frac{1+i\alpha}{\Gamma^2\,(1+\alpha^2)}\right)\left(\left(-q^2\right)\delta a_{0n}^* + 2iq\,(+ik_n)\,\delta a_{0n}^* - {k_n}^2\delta a_{0n}^*\right)] \end{aligned} \tag{3.70}$$

If we consider a_0 as a real number, we rewrite Eqs. 3.65-3.69 as:

$$\delta a_{0n}\,(W_n + iY_n + i\omega + \lambda) + {\delta a_{0-n}}^*\left(\sigma\,(1+i\alpha)\,{a_0}^2\right) = 0 \tag{3.71}$$

$$\delta a_{0n}\left(\sigma\,(1-i\alpha)\,{a_0}^{*2}\right) + {\delta a_{0-n}}^*\,(W_{-n} - iY_{-n} - i\omega + \lambda) = 0 \tag{3.72}$$

Where:

$$W_n = \sigma\left[1-\mu+4\left|a_0\right|^2+\left(\frac{1}{\Gamma^2\left(1+\alpha^2\right)}\right)\left(q^2+2qk_n+{k_n}^2\right)\right] \quad (3.73)$$

$$W_{-n} = \sigma\left[1-\mu+4\left|a_0\right|^2+\left(\frac{1}{\Gamma^2\left(1+\alpha^2\right)}\right)\left(q^2-2qk_n+{k_n}^2\right)\right] \quad (3.74)$$

$$Y_n = \sigma\left[-\alpha\mu+2\alpha\left|a_0\right|^2-\left(\frac{\alpha}{\Gamma^2\left(1+\alpha^2\right)}\right)\left(q^2+2qk_n+{k_n}^2\right)\right] \quad (3.75)$$

$$Y_{-n} = \sigma\left[-\alpha\mu+2\alpha\left|a_0\right|^2-\left(\frac{\alpha}{\Gamma^2\left(1+\alpha^2\right)}\right)\left(q^2-2qk_n+{k_n}^2\right)\right] \quad (3.76)$$

If we call M the characteristic matrix of the linear system composed by Eqs. 3.71-3.72 and we calculate det(M)=0, we obtain:

$$\left(W_n+iY_n+i\omega+\lambda\right)\left(W_{-n}-iY_{-n}-i\omega+\lambda\right)-\sigma^2\left(1+\alpha^2\right)\left|a_0\right|^4=0 \quad (3.77)$$

Eq. 3.77 is the secular equation.

3.3.4 Simulation results

In this subsection we present the results of the simulations performed by integrating Eq. 3.56.The method exploited to solve Eq. 3.56 is the Exponential time-stepping method, which is described in [16].
In Fig. 3.12 we show a plot of the field amplitude as a function of the time for different values of the pump parameter μ at fixed α, Γ and L. In particular for this simulation the values of the parameters are showed in the Table 3. We present a

Table 3.

L (μm)	1000
σ	0.007
Γ	0.034
α	1.71

current scan where the pump parameter μ is varied stepwise in time between 1.2

and 2.8, keeping it constant for 300ns, i.e. long enough for the system to develop a steady state. In Fig. 3.12 we can notice that for μ between 1.2 and 1.6 we have

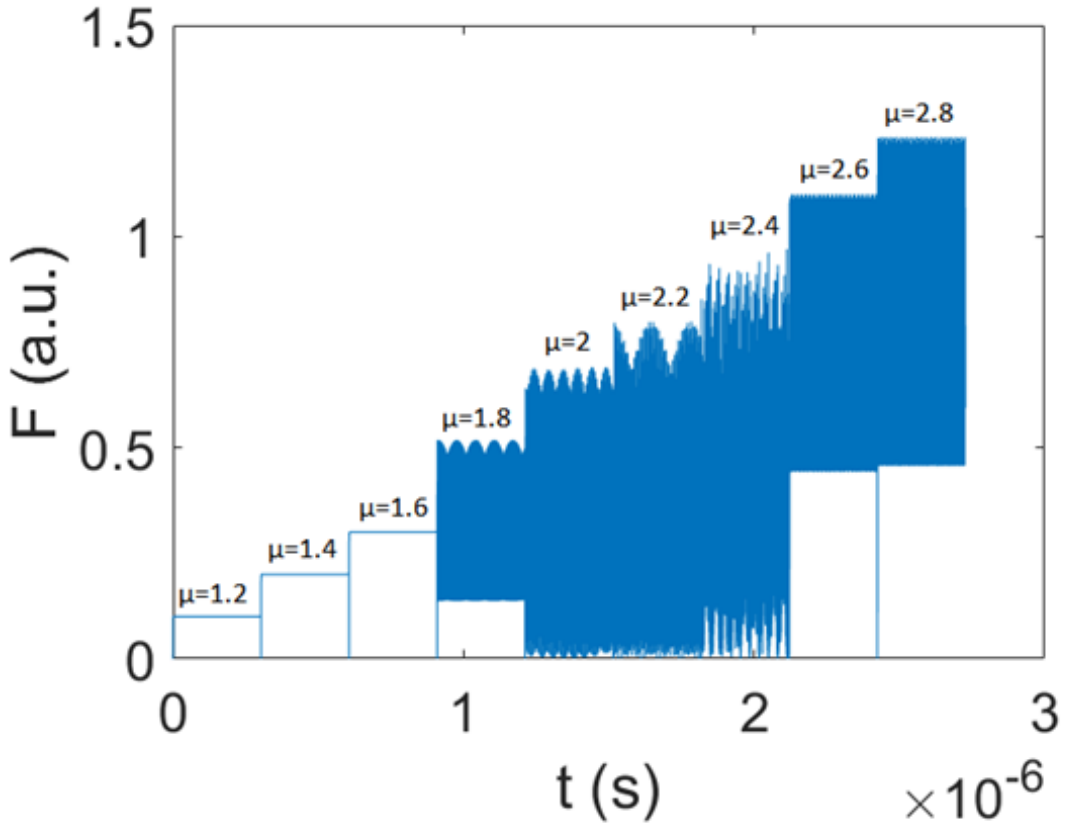

Figure 3.12: Sweeping of the pump parameter μ: amplitude of the field F as a function of the time.

a continuous wave regime. For $\mu \geq 1.8$ we have multi-wavelength emission and we find an alternance between regular (μ=1.8, 2, 2.2, 2.6, 2.8) and irregular (μ=2.4) regimes. Therefore we confirm that our model is able to reproduce alternance between locked and unlocked regimes.

3.3.5 Validation of the Linear Stability Analysis

We can solve numerically the model and we can also perform the linear stability analysis (LSA), since we retrieved the secular equation for the reduced model, Eq.

3.77. Therefore we have checked the consistency of the LSA with the simulations performed on our model, Eq. 3.56.
We present in Fig. 3.13 a visual synthesis fo the LSA predictions: while varying parameters α and μ we plot in colorscale the real part of the eigenvalue λ for Γ=0.03 and Γ=0.3. The color maps show the value of real(λ) in the parameter plane. If real(λ) is positive the solution is unstable, while if real(λ) is negative it is stable.
The consistency with the simulations is shown in Fig. 3.14 where we superimpose to the previous colorscale eigenvalue maps the results of the simulations, represented by black and red dots. We did not find any case of disagreement between the scenario given by the LSA and the numerically performed simulations: wherever the LSA predicted a CW or a multimode regime the simulations showed at regime the same regime.

3.3.6 Reduced model in the ring configuration: comparison with the complete model

An essential check of the validity of the reduced model is based on its comparison with the results obtain by simulating the full model based on the ESMBEs, i.e. Eqs. 3.5-3.7. Therefore, in order to realize this comparison, we tested the two models in the ring configuration, by considering the same set of parameters compatible with the limits within which the reduced model has been derived (Table 3), and we compared the results obtained by the two models, in terms of LSA and type of multimode regime as obtained by the simulations. In Fig. 3.16 we present the results obtained for Γ=0.03 for three values of α. For the lowest two values of α we have total agreement in terms of LSA results and also in terms of type of regime obtained when the laser shows multimode emission, and this occurs up to I/I_{thr} =2.54. For $\alpha = 2$ we have only one discrepancy between complete and reduced model in terms of stability of the CW emission, precisely at I/I_{thr} =1.42. We justify this considering that this value of the normalized pump parameter when $\alpha = 2$ is at the boarder of the stability region (see Fig. 3.13.a), where it is expected to have more relevant differences between the results obtained with the two models.
In Fig. 3.16 we show an analogous comparison obtained by setting Γ=0.3 for two values of α, 0.7 and 1.7. In this case there is total agreement between the results obtained with the two models, both in terms of CW stability and in terms of type of obtained multi-mode regime.
Furthermore, the found multimode regimes present strong similarity with the ones obained with the full model: the irregular regimes are chaotic in both cases and the output power oscillates between the value 0 and a maximum value; the regular regimes are in both cases characterized by a propagation of a regular repetition of structures.
We also remark that the reduced model present a relevant strength in the reproduction of the instability thresholds also for high values of the pump, beyond the

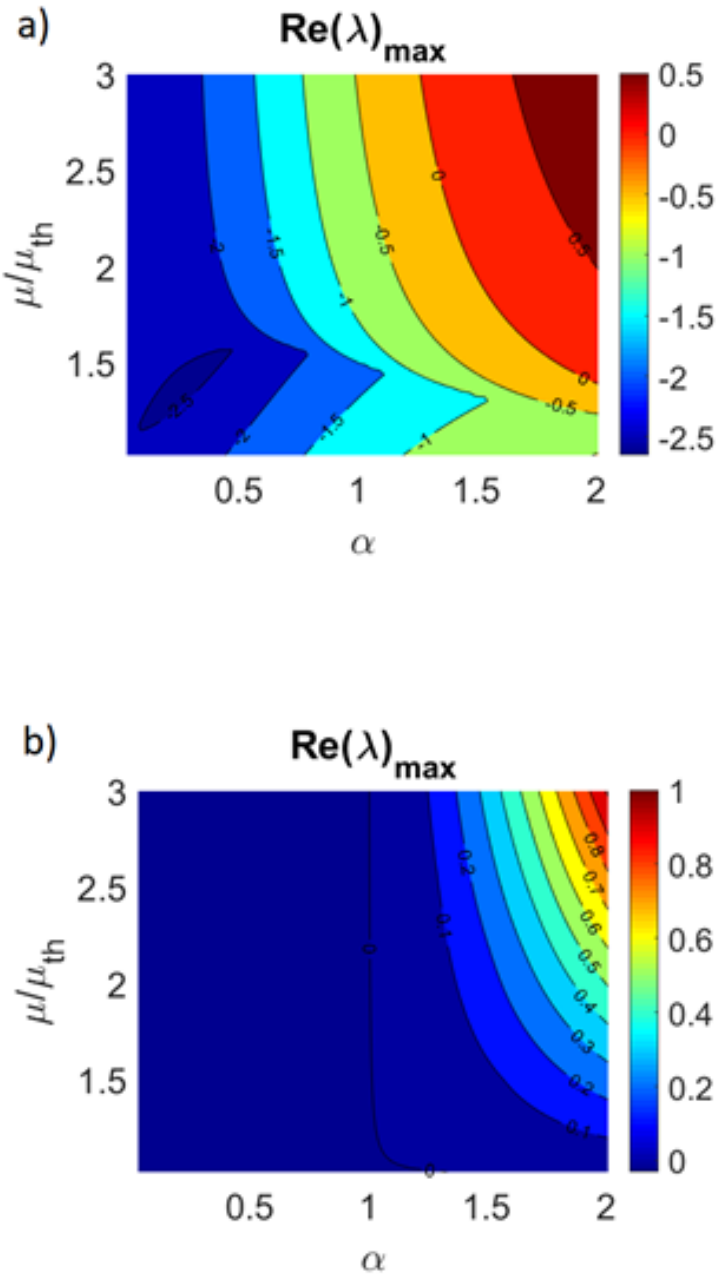

Figure 3.13: a) Stability map for Γ=0.03. On the horizontal axis we represent α, while on the vertical axis we have the μ/μ_{th} where in our case μ_{th}=1. In the color map the real part of the eigenvalue λ is shown. b) Stability map for Γ=0.3.

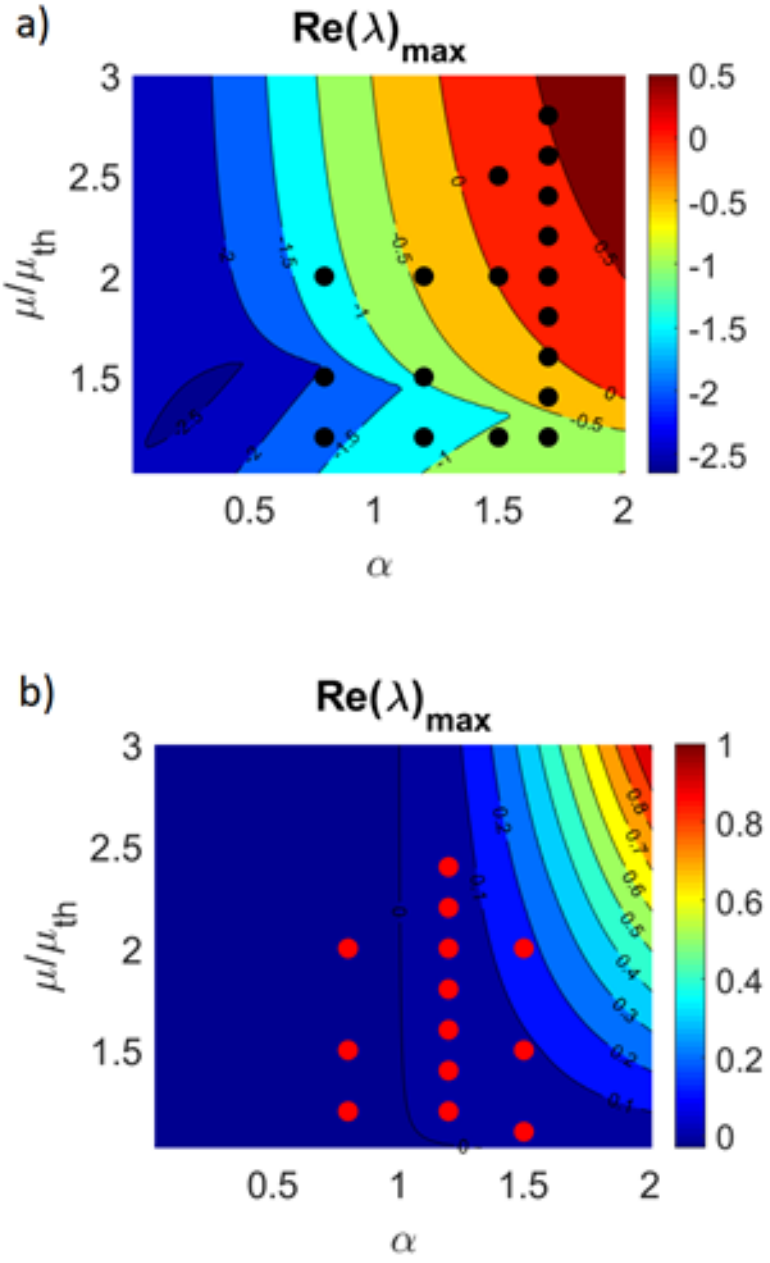

Figure 3.14: Stability map compared with the results of numerical solving of the model Eq. 3.56 for Γ=0.03 (a) and Γ=0.3 (b). In Fig. a) black dots and in Fig. b) red dots represent agreement between simulation and LSA.

intrinsic limits of its derivation.

α=1

Complete	Reduced	I/Ithr
CW	CW	1.14
CW	CW	1.42
CW	CW	1.7
CW	CW	1.98
CW	CW	2.26
CW	CW	2.54

α=1.5

Complete	Reduced	I/Ithr
CW	CW	1.14
CW	CW	1.42
CW	CW	1.7
CW	CW	1.98
MM, regular	MM, regular	2.26
MM, regular	MM, regular	2.54

α=2

Complete	Reduced	I/Ithr
CW	CW	1.14
MM, regular	CW	1.42
MM, regular	MM, regular	1.7
MM, irregular	MM, irregular	1.98
MM, regular	MM, irregular	2.26
MM, regular	MM, irregular	2.54

Figure 3.15: Comparison between simulated results obtained by integrating ESMBEs(complete model, Eqs. 3.5-3.7) and reduced model (Eq. 3.3) for Γ=0.03.

α=0.7

Complete	Reduced	I/Ithr
CW	CW	1.11
CW	CW	1.33
CW	CW	1.55
CW	CW	1.77
CW	CW	1.99
CW	CW	2.21

α=1.7

Complete	Reduced	I/Ithr
MM, irregular	MM, irregular	1.11
MM, irregular	MM, irregular	1.33
MM, irregular	MM, irregular	1.55
MM, irregular	MM, irregular	1.77
MM, irregular	MM, irregular	1.99
MM, irregular	MM, irregular	2.21

Figure 3.16: Comparison between simulated results obtained by integrating ESMBEs(complete model, Eqs. 3.5-3.7) and reduced model (Eq. 3.3) for Γ=0.3.

3.4 Ring with optical injection

The study of OFCs in passive systems as microresonators based on Kerr media, have been particularly relevant because of their application for phonic integration and miniaturization of device on chip-scale. Recently, the study of OFC in these systems was unified with the treatment of combs in active systems, with the achievement of a general version of the LLE [12]. The generalized LLE can be used also to describe lasers, in our case ring QCLs, in presence of optical injection. The introduction of a driving field into the ring QCL setup involves two additional control

parameters, i.e. the intensity and the frequency of the optical injected field, which enable the possibility to generate and manipulate temporal solitons, one type of OFC that have importance in the field of spectroscopy and metrology [57]. Let us consider the case of a ring QCL in presence of injection of an optical field. This configuration is shown in Fig. 3.17. The experiments performed in [50] and [57]

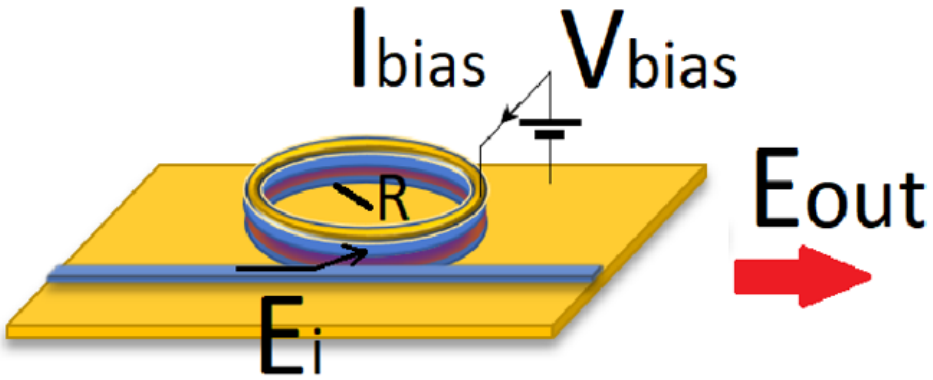

Figure 3.17: Scheme of a QCL with a ring resonator, in presence of electric field E_i. E_{out} is output field, I_{bias} is the bias current, V_{bias} is the bias voltage. The ring resonator is coupled with a straight waveguide, to a driving laser providing the injected field E_i.

exploit ridge-waveguide geometry of the QCL which is coupled to a straight waveguide, used to convey the driving field into the resonator.
Let us consider how this system behaves by varying the intensity of the injected field. According to the considered region of the parameter space, if we consider the plane with output power on the vertical axis and power of the injected field on the orizontal axis, the curve which describes the actual behaviour of the system can be a monodromic function. Therefore, for each value of the injected power, one value of the output power exists.
Conversely, for different portions of the parameters space, bistability can occur, i.e. the curve describing the laser in the injected power-output power plan, is a function with multiple values in some intervals, with an hysteretic behaviour.
An example of bistability in this system is shown in Fig. 3.18, obtained by adopting the parameters in Table 4. This curve is characterized by an unstable region for values of the injection power less than 29 mW, which corresponds to the injection locking point named IL. By increasing the injected power, we have a CW stability region and between the point SN1 and SN2 the curve is not monodromic. A further point which marks the border between an instability and a stability region is the modulation instability point MI, placed on the upper branch of the curve.

The portion of the curve with negative slope in unstable, and this always occurs in optical systems.

More aspects of the bistability in injected ring-QCL will be analyzed carefully in

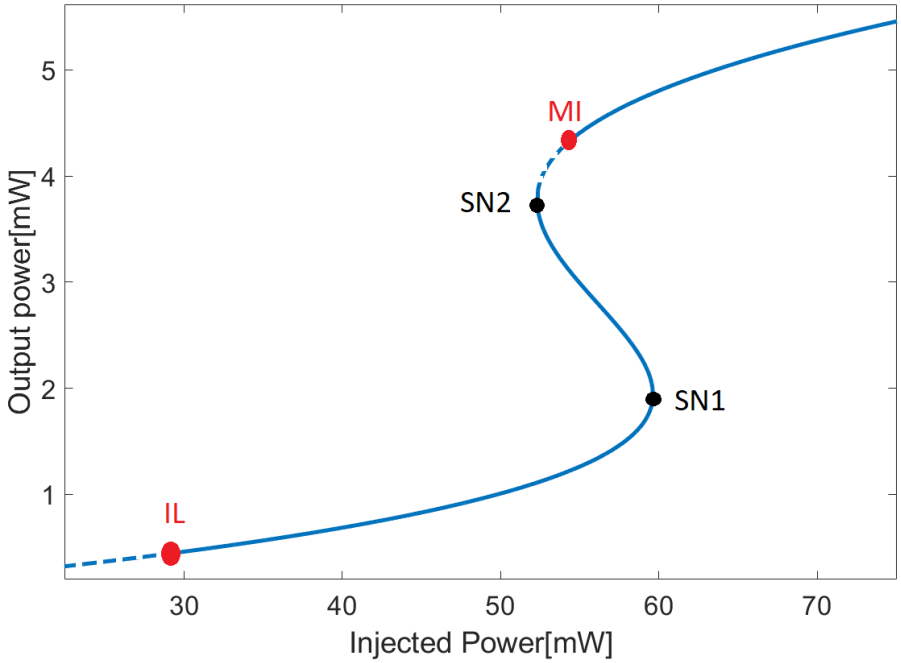

Figure 3.18: Bistability in QCL-ring with optical injection: on the vertical axis the output power expressed in mW; on the horizontal axis the optical power of the injected field expressed in mW. IL: injection locking point. MI: modulation instability point. Curve obtained by using the parameters in Table 4.

the following, during the discussion of the simulation results.

We perform a simulative study of this system by exploiting the same set of equations for electric eield E, polarization P_0 and carrier density N_0, which we previously introduced for the free-running ring QCL, i.e. Eqs. 3.5-3.7, but we insert properly the injected electric field E_i in the boundary conditions as in [12], obtaining:

$$E(0,t) = \sqrt{T}E_i + \sqrt{R}E(L,t)e^{-i\delta_0} \tag{3.78}$$

where T is the trasmittance of the ring waveguide ($T = 1 - R$) and δ_0 is the normalized detuning between the frequency of the optical injected field ω_i and the closest ring cavity resonance ω_c, so that it is expressed as $\delta_0 = nL/c(\omega_c - \omega_i)$, where n is the group refractive index of the laser active waveguide, L is the length of the cavity, and c the speed of light. Furthermore, R is the reflectivity of the ring, L the length of the cavity, t a generic time value and E_i the injected optical field.

As in the previous approaches, we simplify the model equations by introducing

proper transformations of the variables, as in [12]. First we introduce the following auxiliary variables:

$$E'(z,t) = \eta_1 E(z,t), \tag{3.79}$$
$$P'(z,t) = i\eta_2 P(z,t), \tag{3.80}$$
$$D(z,t) = \eta_3 N_0(z,t) \tag{3.81}$$

where:

$$\eta_1^2 = \frac{\eta_3 \tau_e}{2\hbar}, \tag{3.82}$$
$$\eta_2 = \eta_1, \tag{3.83}$$
$$\eta_3 = \epsilon_0 \epsilon_b f_0 \tag{3.84}$$

By inserting Eqs. 3.79-3.84 into Eq. 3.5 and removing the primes in E' and P' we obtain:

$$\frac{\partial E}{\partial z} + \frac{1}{v}\frac{\partial E}{\partial t} = -\frac{\alpha_L}{2}E + g'P, \tag{3.85}$$

where $g'{=}{-}ig$.
If we insert Eqs. 3.79-3.84 into Eq. 3.6 we get:

$$i\eta_1 \frac{\partial P_0}{\partial t} = \frac{(1+i\alpha)}{\tau_d}\left[-i\eta_1 P_0 + i f_0 \epsilon_0 \epsilon_b (1+i\alpha)\, i\eta_1 N_0 E\right], \tag{3.86}$$

$$\frac{\partial P'}{\partial t} = \frac{(1+i\alpha)}{\tau_d}\left[-P' - f_0 \epsilon_0 \epsilon_b (1+i\alpha)\, N_0 E'\right]. \tag{3.87}$$

and, finally, by removing also in this case the primes in E' and P':

$$\frac{\partial P}{\partial t} = \frac{(1+i\alpha)}{\tau_d}\left[-P - (1+i\alpha)\, DE\right]. \tag{3.88}$$

Let us now rewrite the equations for the carriers:

$$\eta_3 \frac{\partial N_0}{\partial t} = \frac{I\eta_3}{eV} - \frac{\eta_3 N_0}{\tau_e} + \frac{i\eta_3}{4\hbar}\left[E^* P_0 - E P_0{}^*\right] \tag{3.89}$$

If we introduce the scaled variable D, defined as:

$$D = \eta_3 N_0 \tag{3.90}$$

we obtain:

$$\frac{\partial D}{\partial t} = \frac{1}{\tau_e}\left[\frac{I\eta_3\tau_e}{eV} - D + \frac{i\eta_3\tau_e}{4\hbar}\left(E^* P_0 - E P_0{}^*\right)\right] \tag{3.91}$$

Using Eq. 3.82 and introducing the normalized pump parameter:

$$\mu = \frac{I\eta_3\tau_e}{eV} \tag{3.92}$$

we obtain:

$$\frac{\partial D}{\partial t} = \frac{1}{\tau_e}\left[\mu - D + \frac{1}{2}\left(E^*P + EP^*\right)\right]. \tag{3.93}$$

where in the last passage we removed again the primes for field and polarization. At this point we introduce new auxiliary variable for field and polarization:

$$E''(z,t) = E(z,t)\, e^{(lnR - i\delta_0)}, \tag{3.94}$$
$$P''(z,t) = P(z,t)\, e^{(lnR - i\delta_0)}. \tag{3.95}$$

We rewrite Eq. 3.96 by inserting the definitions Eqs. 3.94-3.95.

$$v\frac{\partial E''}{\partial z} + \frac{vE''}{L}\left(-lnR + i\delta_0\right) + \frac{\partial E''}{\partial t} = -\frac{v\alpha_L}{2}E'' + g'vP'', \tag{3.96}$$

$$v\frac{\partial E''}{\partial z} + \frac{\partial E''}{\partial t} = \frac{vE''}{L}\left(lnR - i\delta_0 - \frac{v\alpha_L L}{2}\right) + g'vP'', \tag{3.97}$$

$$v\frac{\partial E''}{\partial z} + \frac{\partial E''}{\partial t} = \frac{vTE''}{L}\left(\frac{lnR}{T} - \frac{i\delta_0}{T} - \frac{v\alpha_L L}{2T}\right) + g'vP'', \tag{3.98}$$

$$v\frac{\partial E''}{\partial z} + \frac{\partial E''}{\partial t} = \frac{vT}{L}\left[\left(\frac{lnR}{T} - \frac{i\delta_0}{T} - \frac{\alpha_L L}{2T}\right)E'' + \frac{g'L}{T}P''\right], \tag{3.99}$$

$$v\frac{\partial E''}{\partial z} + \frac{\partial E''}{\partial t} = \frac{vT}{L}\left[\left(\frac{lnR}{T} - \frac{i\delta_0}{T} - \frac{\alpha_L L}{2T}\right)E'' + AP''\right]. \tag{3.100}$$

where $A = \frac{g'L}{T}$.
At this point, we assume valid the low transmission approximation, defined by:

$$g'L \ll 1 \tag{3.101}$$
$$\alpha_L L \ll 1 \tag{3.102}$$
$$T \ll 1 \tag{3.103}$$
$$\delta_0 \ll 1 \tag{3.104}$$

In this limit the auxiliary variables E'' and P'' coincide with E and P, respectively. We obtain:

$$v\frac{\partial E}{\partial z}+\frac{\partial E}{\partial t}=\frac{vT}{L}\left[-\left(1+i\theta_0+\frac{\alpha_L L}{2T}\right)E+AP\right] \tag{3.105}$$

where $\theta_0=\frac{\delta_0}{T}$.

$$v\frac{\partial E}{\partial z}+\frac{\partial E}{\partial t}=\left[-\left(v\left(\frac{T}{L}+\frac{\alpha_L}{2}\right)+i\frac{vT}{L}\theta_0\right)E+\frac{vTA}{L}P\right] \tag{3.106}$$

$$v\frac{\partial E}{\partial z}+\frac{\partial E}{\partial t}=\frac{1}{\tau_p}\left[-\left(1+i\frac{\tau_p vT}{L}\theta_0\right)E+A'P\right] \tag{3.107}$$

where $\tau_p=\left[v\left(\frac{T}{L}+\frac{\alpha_L}{2}\right)\right]^{-1}$ and $A'=\frac{vTA}{L}$.
We can write the final equations of the model:

$$v\frac{\partial E}{\partial z}+\frac{\partial E}{\partial t} = \frac{1}{\tau_p}\left[-\left(1+i\theta_0'\right)E+A'P\right] \tag{3.108}$$

$$\frac{\partial P}{\partial t} = \frac{(1+i\alpha)}{\tau_d}\left[-P-(1+i\alpha)\,DE\right] \tag{3.109}$$

$$\frac{\partial D}{\partial t} = \frac{1}{\tau_e}\left[\mu-D+\frac{1}{2}\left(E^*P+EP^*\right)\right]. \tag{3.110}$$

where $\theta_0'=\frac{\tau_p vT}{L}\theta_0$.
We simulated the device by using the Eqs. 3.108-3.110 with the boundary condition 3.78.
In the next subsection we will study the spatiotemporal dynamics predicted by this model with the aim to characterize the generation and the characteristic of OFCs in this setup.

3.4.1 Numerical results

In order to obtain the simulation results that we will show in the next sections we exploited the values of the parameters presented in Table 4, which correspond to the case shown in Fig. 3.18.

We searched for dynamical regimes of interest, pattern formation and solitons, comparing the dynamics of the full model with the results achieved with the generalized LLE [12], obtaining good results. The most interesting dynamical regimes are Cavity Solitons (CS) and Turing Rolls. CS are isolated peaks of intensity which sit on the pedestal of a homogeneous stationary solution, while Turing rolls are sequences of identical equally spaced peaks sitting on a constant background.
As already mentioned, this regime is characterized by a bistability in the plane

Table 4.

δ_0	α	μ	L	τ_d	τ_p	τ_e	n
-0.55	1.9	1.045	4.5 mm	0.18ps	130ps	0.2ps	3.3

Output Power-Injected Power, with a S-shaped curve.
We performed several simulations by keeping constant the value of the current, and by varying the injected optical field. We report here two characteristic dynamical behaviour of the simulated laser, that we found in the high branch of the S-shaped curve, such as Cavity Solitons and Turing Rolls. For both these cases the value of the Power of the injected field is 58.4 mW and pumping current I, corresponding to the pump parameter μ =1.045 (see Table 4), has a value of 21mA.
First let us consider the Turing Rolls regime, shown in Fig. 3.19. We have a stable sequence of several peaks which propagate inside the cavity. The minimum value of these peaks corresponds to the CW stable background that we have for the same value of E_i on the lower branch of the steady state curve.
By decreasing the value of the injected field but remaining in the bistability region, we found another regime, with distinguished sets of peaks as shown in the figure 3.20. Then, starting from this regime we performed some steps in order to obtain to obtain one stable CS. In Fig. 3.21 the simulated Cavity Soliton is shown. This dynamical regime is characterized by the propagation of one single peak inside the laser cavity. In Fig. 3.21. a) the temporal distance between two adjacent peaks corresponds to the cavity roundtrip RT=49.5ps. The Optical Spectrum is presented in figure 3.21. b): it is characterized by one main peak corresponding to the cavity mode closer to the injected field frequency and then there are secondary peaks as it is shown in the plot.
Let us briefly explain the procedure performed to obtain the CS. First a value of E_i characterized by the presence of Turing Rolls on the higher branch of the steady states curve has been found. Then, in correspondence of this value, since the Turing Rolls electric field profile consists of a sequence of several identical peaks sitting on a constant background, we select and cut a single peak of this set. Therefore we have a cavity field profile consisting of one single peak sitting on a constant background. When this profile is used as an injection power initial condition for a further simulation performed exploiting the same injection power where Turing Rolls occur. This peak in this second simulation at regimes becomes the CS shown

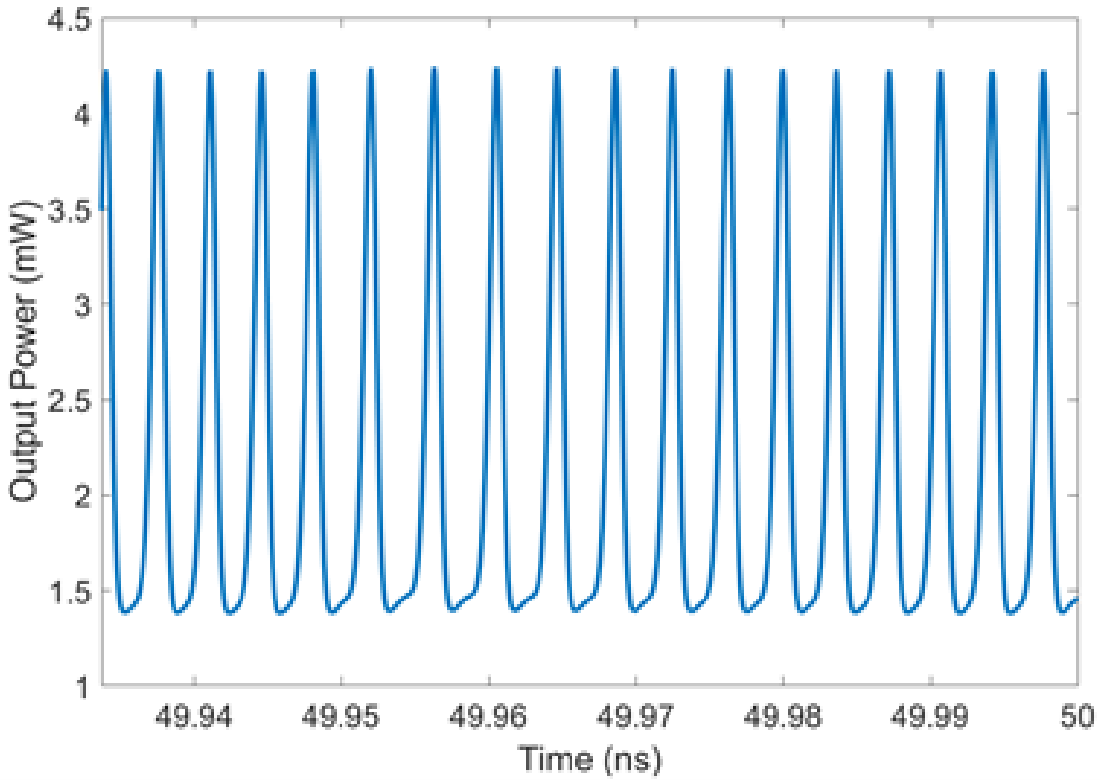

Figure 3.19: Output Power as a function of the time for a Turing rolls regime, found for injected power P_i=58.4mW, I=21mA and BN frequency 20.2GHz.

in Fig. 3.21. a).

3.5 Conclusions

A numerical study of multimode dynamics of a free running ring QCL has been performed, by exploiting the EMBEs adapted for this resonator. The absence of linear chirp behaviour, the alternance between locked and unlocked regimes, and the typical shape of the power structures found in the combs regimes as in the experimes, were retrieved and reproduced.
A reduced model was also presented and the comparison between full and reduced model showed an agreement far above the near threshold operation, where the second one has been derived.
Finally, we also performed an analysis of a bistable regime characterizing the ring QCL with optical injection, and we were able to reproduce with our model some relevant experimentally achieved multimode regimes, such as the cavity soliton and Turing rolls.

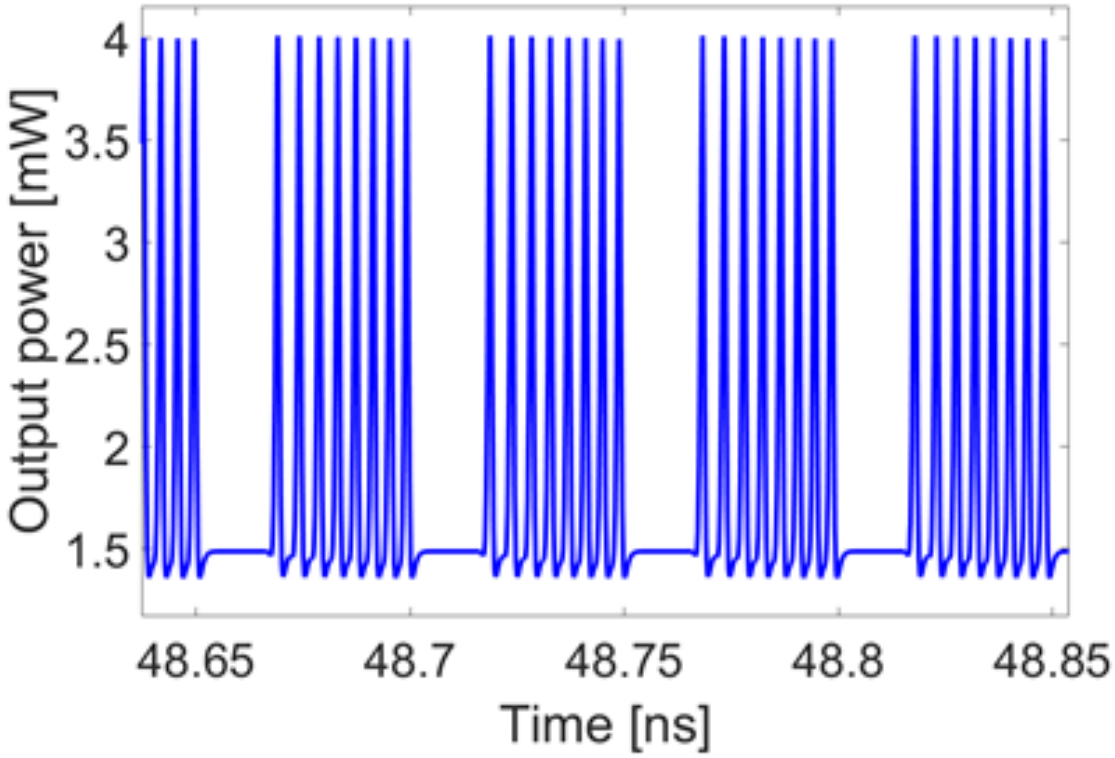

Figure 3.20: Output Power as a function of the time for a regime characterized by a sequence of set of peaks, found for P_i=57.8mW, I=21mA and BN frequency 20.2GHz.

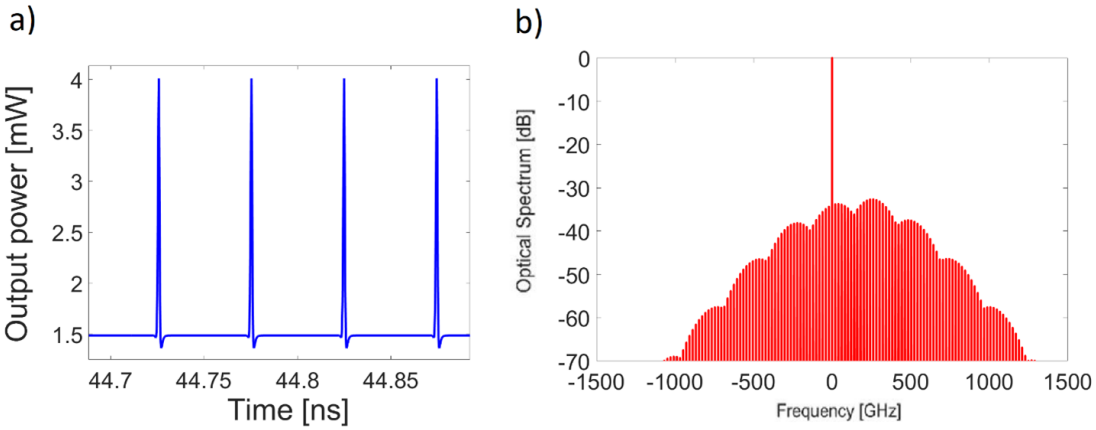

Figure 3.21: Cavity Soliton found for P_i=57.8mW, I=21mA and BN frequency 20.2GHz. a) Output Power as a function of the time. b) Optical Spectrum.

Chapter 4

Scattering type Self-Detection Near-Field Optical Microscopy

In the section 1.3 we have seen that Self-Mixing offers the possibility to perform detectorless interferometric measurements. In fact in the SMI the light source (a semiconductor laser, in our case a QCL) is used as a detector. The nonlinear superposition between the light back-diffused from a target and the light inside the cavity of the laser, changes the emission characteristics of the source. In particular the laser threshold, emission frequency, output optical power and voltage across the laser terminals are modified and by measuring these quantities it is possible to retrieve information related to the target optical susceptivity. The implementation of this technique with Terahertz QCL is particularly relevant since in this spectral region detectors are expensive and not efficient, therefore the possibility to use a setup without detector is convenient.
The description SMI has been achieved by using the LK model, which we studied and analyzed deeply in section 1.3.2. It is composed by two rate equations for field and carrier density, and described the behaviour of the laser in presence of feedback. Furthermore, we also introduced the classification of the feedback regimes. In this chapter the very weak and most of all the weak regime will be object of study.
The second part of section 1.3 is dedicated to the introduction of s-SNOM, an imaging technique which circumvents the diffraction limit. s- SNOM is based on the presence of a nanometric tip interacting with the analyzed sample, exploiting the near-field interaction between tip and sample, mediated by evanescent waves. These methods are classified as SNOM techniques, and their spatial resolution is limited by the dimension of the curvature radius of the tip (typically 10 nm).
The combination between SNOM and SMI have produced the SD s-SNOM, which allows in THz region a spatial resolution of 10 nm by exploiting light with 100 μm-order of magnitude wavelength λ, i.e. a spatial revolution about $\lambda/10000$, far beyond the diffraction limit [48]. Therefore this technique enable a high resolution imaging in the THz region. Another advantage of this method is the absence of

the detector, deriving from the SMI configuration. The setup of SD s-SNOM has been shown in Fig. 1.10 and described in section 1.3.4. This will be starting point of this chapter.
In Section 4.1 a general review about the most recent and relevant results is presented, in order to contextualize the original results presented in this work, in both theoretical and simulation-experimental purview. In particular, a deep focus about the last-generation implementations of this technique is proposed in this section, ranging from the solid-state materials analysis, to its usage in the detection of the skin cancer [69].
In Sec. 4.2 we pass from the LK model explained in Sec. 1.3.2 to a LK model valid for the SD s-SNOM configuration by introducing proper hypotheses of this configuration.
In Section 4.3 we present the results of a theoretical treatment of the LK model in the very weak and in the weak feedback regimes. We introduce some approximated formulas that enable a retrieval of the dielectric properties of a given material, analyzed with a s-SNOM setup. In the very weak regime a sinusoidal approximation of the interferometric fringes can be applied in order to retrieve the final equations. In the weak regime the theory is based on first order Taylor expansions, in order to have suitable mathematical expressions of the interferometric signals, and retrieve the scattering coefficient and its harmonics. From the scattering coefficient it is possible, then, to retrieve the dielectric properties of the analyzed material. The complete derivation of these formulas for very weak and weak regimes, are presented respectively in Appendix C and Appendix D.
In the last part of this Chapter, which is Section 4.4, we show the numerical results obtained by implementing the formulas retrieved in Appendix D, and also by using an original numerical code that simulates the s-SNOM configuration. A further comparison with experimental results is then performed.

4.1 Introduction and motivation

The Terahertz(THz) region, characterized by wavelentgth between 30μm and 300μm, holds a relevant importance for the study of optical properties of materials. In fact the electromagnetic waves in this region may be successfully exploited for the investigation of resonances of solids and biological tissues [25], [6]. The main limits for the realization of optical techniques aimed to perform material analysis or imaging in the THz range are the diffraction limit and the lack of efficient, compact detectors.
The SD s-SNOM is a nanoscopy technique convceived to solve both these problems. In fact, the spatial resolution far beyond the diffraction limit, allows to perform a direct analysis of structured materials on nanoscopic scale, like quantum dots and nanocomposites, electronic components like nanotransistors and memory cells, or

biological systems like molecules and proteins. Furthermore the Self-Mixing scheme implies the usage of the laser as detector, which allows to make up for the absence of efficient detectors in the THz region.
A THz-QCL emits a laser beam, which describes an optical path determined by piezometric and parabolic mirrors and impinges on the target, composed by a nanometric probing tip placed in proximity of the analyzed specimen surface. An attenuator is positioned into this configuration in order to select the intensity of the feedback. The circumvention of the diffraction limit occurs because the near-field interaction between sample and probe is mediated by evanescent fields, which are not subject to the diffraction. The interaction modifies amplitude and phase of the light scattered by the probe, which is partially or totally reinjected into the laser cavity. In a conventional s-SNOM configuration the scattered light would collected into an external detector.
The intracavity and the back-scattered field, which carries the information about the analyzed material sample, interfere and modify the emission properties of the laser, i.e. the emission frequency, output power, voltage across the laser terminals. Analyzing the change in these properties, typically the voltage across the laser terminals,it is then possible to retrieve information about the target.
The experimental configuration of SD s-SNOM, shown in Fig. 1.12, has been proposed in [21], in order to prove a amplitude- and phase-resolved technique for the analysis and imaging of solids in the THz, with 60-70 nm spatial resolution. By demodulating the interferometric signal by using a lock-in amplifier, it is possible to retrieve modulus and phase of its background-free harmonics that emcompasses the information about the dielectric function of the sample. In [21] the operative feedback regime is the very weak regime, where fringes are approximately sinusoidal and in this hypothesis modulus and phase of the third harmonics have been retrieved through a 2-parameters fitting procedure.

An example of application of this method to Cesium Bromide (CsBr) and Gold (Au) is shown in Fig. 4.1, where amplitude and phase of the near field signal are plotted as a function of the distance between tip and sample. In the Sec. 4.3 of this work we will review the mathematical treatment related to the very weak regime which justifies the approximations introduced for the analysis and processing of the experimental data presented in [21].
A relevant issue related to the study of this technique is the possibility to perform a processing and analysis of data for a higher level of feedback (i.e. weak, moderate), where the sinusoidal approximation for the interferometric fringes is not valid and a more accurate approximation is needed. In this work we exploit a theoretical treatment of the LK model specialized for the weak regime (see Appendix D), in order to obtain approximated formulas that allow to retrieve the optical properties of a given material sample resonant in the THz region. Furthermore, we process and analyze sets of experimental data by exploiting the developed theory. This study has been presented in [54].

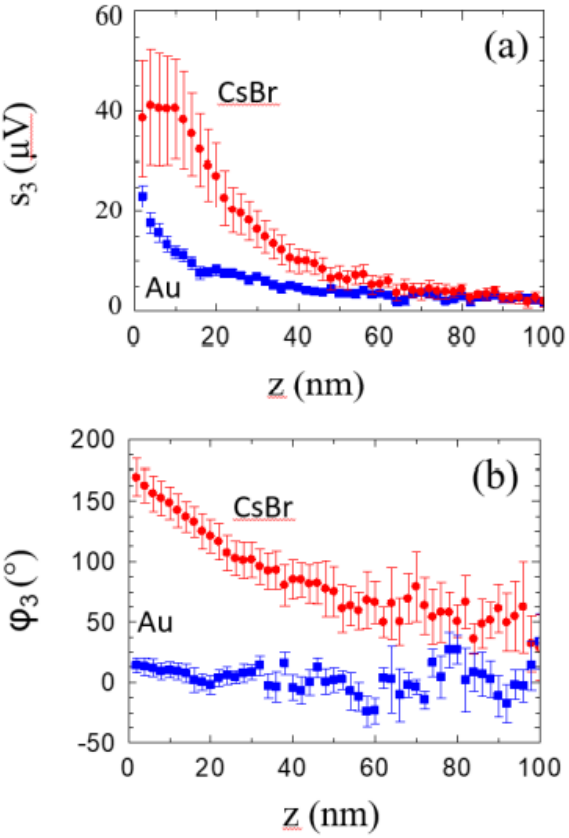

Figure 4.1: THz near field amplitude and phase as a function of tip-sample distance (approach curves). (a-b) Comparison between the experimental amplitude (a) and phase (b) of CsBr (red) and Au (blue), collected as a function of the tip-sample distance z. Reproduced from [21].

4.2 Lang-Kobayashi Equations for SD s-SNOM configuration

Let us consider the standard Lang Kobayashi equations 1.3 and 1.10. In these equations the coupling coefficient $\widetilde{\kappa}$ appearing in the feedback term in the Equation 1.3 is expressed by the equation 1.9 and depends on the reflection coefficient of the target $\sqrt{R_3}$, defined as the ratio between reflected field and incident field. Therefore, it is a real quantity. Conversely, in SD s-SNOM configuration the target is not just a mirror, but it is a more complicated objected composed by the probing tip having a near-field interaction with the analyzed material sample. For this reason, the

reflection coefficient $\sqrt{R_3}$ must be replaced by the complex scattering coefficient σ, proportional to the effective polarizability of the target α_{eff}, which depends on the complex dielectric function of the sample. This substitution implies the introduction of a complex coupling coefficient $\widetilde{\kappa}$ in the LK model modified for the SD s-SNOM configuration, and this coefficient is expressed by:

$$\widetilde{\kappa} = \sigma \frac{c\widetilde{a}(1-R)}{2\eta l\sqrt{R}} \tag{4.1}$$

where R is the laser mirror reflectivity (we assume that both facets of the laser have the same value of reflectivity), η is the refractive index of the laser medium, l is the length of the laser cavity and $\widetilde{a}$ is an attenuation factor connected to the presence of an optical attenuator in the experimental configuration.
This last passage is crucial, because it allows to include into the LK model the information about the near-field interaction between tip and sample, as explained. At this point we want to determine the steady-state solutions of the LK model with a complex scattering coefficient with modulus S and phase ϕ appearing in the expression of the coupling coefficient $\widetilde{\kappa}$. We follow an approach [31] based on steady-state solutions because the temporal change of the feedback, linked to the tip oscillation on the scale of 10-100 KHz, is much slower than the fast field and carrier dynamics in the QCL (below the ns scale) field and carrier timescales.
The first step of the procedure consists to rewrite the L-K equations introducing the transparency carrier density n_0 into the equation for the field and recalling μ the pumping term into the rate equation for the carrier density. We obtain:

$$\frac{dE(t)}{dt} = \frac{1}{2}(1+i\alpha)\left[G_n(n(t)-n_0) - \frac{1}{\tau_p}\right]E(t) + \widetilde{\kappa}E(t-\tau)e^{-i\omega_0\tau} \tag{4.2}$$

$$\frac{dn}{dt} = -\frac{n}{\tau_e} - G_n(n-n_0)\left|E\right|^2 + \mu \tag{4.3}$$

We now introduce a convenient scaling of Eqs. 4.2-4.3. Let us consider first Eq. 4.3.

$$\begin{aligned}\frac{dn}{dt} &= -\frac{n}{\tau_e} - G_n(n-n_0)\left|E\right|^2 + \mu = \\ &= -\frac{n-n_0}{\tau_e} - \frac{n_0}{\tau_e} - G_n(n-n_0)\left|E\right|^2 + \mu\end{aligned} \tag{4.4}$$

Defining:

$$\Delta n = n - n_0 \tag{4.5}$$

Equation 4.4 can be rewritten as:

$$\begin{aligned}\frac{d(\Delta n)}{dt} &= -\frac{\Delta n}{\tau_e} - \frac{n_0}{\tau_e} - G_n(\Delta n)\left|E\right|^2 + \mu = \\ &= \frac{1}{\tau_e}\left[(\tau_e\mu - n_0) - \Delta n\left(1 - G_n\tau_e\left|E\right|^2\right)\right]\end{aligned} \tag{4.6}$$

Then we define:

$$I_p = \tau_e \mu - n_0 \tag{4.7}$$
$$\widetilde{E} = \sqrt{G_n \tau_e} E \tag{4.8}$$

and the scaled equation for carrier density becomes:

$$\frac{d(\Delta n)}{dt} = \frac{1}{\tau_e}\left[I_p - \Delta n\left(1 - \left|\widetilde{E}\right|^2\right)\right] \tag{4.9}$$

Let us consider now the Equation 4.2 and let us multiply it by $\sqrt{G_n \tau_e}$:

$$\sqrt{G_n \tau_e}\frac{dE(t)}{dt} = \frac{1}{2}(1+i\alpha)\left[G_n(\Delta n) - \frac{1}{\tau_p}\right]\sqrt{G_n \tau_e}E(t) + \tilde{\kappa}\sqrt{G_n \tau_e}E(t-\tau)e^{-i\omega_0 \tau} \tag{4.10}$$

Using equation 4.8 we have:

$$\frac{d\widetilde{E}(t)}{dt} = \frac{1}{2}(1+i\alpha)\left[\tau_p G_n \Delta n - 1\right]\frac{1}{\tau_p}\widetilde{E} + \tilde{\kappa}\widetilde{E}(t-\tau)e^{-i\omega_0 \tau} \tag{4.11}$$

Introducing

$$\widetilde{N} = \Delta n \tau_p G_n \tag{4.12}$$
$$\widetilde{I}_p = I_p \tau_p G_n \tag{4.13}$$

the equations 4.11 and 4.9 become:

$$\frac{d\widetilde{E}(t)}{dt} = \frac{1}{\tau_p}\left[\frac{1}{2}(1+i\alpha)\left(\widetilde{N}-1\right)\widetilde{E} + \tau_p \tilde{\kappa}\widetilde{E}(t-\tau)e^{-i\omega_0 \tau}\right] \tag{4.14}$$
$$\frac{d\widetilde{N}(t)}{dt} = \frac{1}{\tau_e}\left[\widetilde{I}_p - \widetilde{N}\left(1 - \left|\widetilde{E}\right|^2\right)\right] \tag{4.15}$$

Separating the field $\widetilde{E}$ in modulus $\widetilde{E}_0$ and phase $\widetilde{\Phi}$ and defining

$$V = 2\frac{1-R}{\sqrt{R}}\tilde{a}\frac{\tau_p}{\tau_c} \tag{4.16}$$

Equation 4.14 can be rewritten as:

$$\frac{d\widetilde{E}_0(t)}{dt} = \frac{1}{2\tau_p}\left[\left(\widetilde{N}-1\right)\widetilde{E}_0 + VS\widetilde{E}_0(t-\tau)cos\left(\omega_0\tau + \Phi(t) - \Phi(t-\tau) - \phi\right)\right] \tag{4.17}$$

$$\frac{d\widetilde{\Phi}(t)}{dt} = \frac{1}{2\tau_p}\left[\alpha\left(\widetilde{N}-1\right) - VS\frac{\widetilde{E}_0(t-\tau)}{\widetilde{E}_0(t)}sin\left(\omega_0\tau + \Phi(t) - \Phi(t-\tau) - \phi\right)\right] \tag{4.18}$$

In Equations 4.17 and 4.18 modulus S and phase ϕ of the scattering coefficient σ explicitly appear.
At this point we are ready to retrieve the steady state solutions of Eqs. 4.17, 4.18 and 4.15. Therefore the conditions $\widetilde{E}(t)=\widetilde{E}(t-\tau)=\widetilde{E}_s$, $\widetilde{N}(t)=\widetilde{N}_s$, $\widetilde{\Phi}(t)=(\omega_F-\omega_0)t$, $\widetilde{\Phi}(t-\tau)=(\omega_F-\omega_0)(t-\tau)$, already mentioned in the study of the standard L-K equations (see Sec. 1.3.2), are imposed.
The equation for the modulus of the field, Eq. 4.17. becomes:

$$0 = \widetilde{N}_s - 1 + VScos\left(\omega_F\tau - \phi\right) \tag{4.19}$$

and defining ΔV=1-$\widetilde{N}_s$ we obtain:

$$\Delta V = VScos\left(\omega_F\tau - \phi\right) \tag{4.20}$$

ΔV is a variable proportional to the interferometric signal, i.e. the voltage across the QCL terminals [70],[1]. Therefore the Eq. 4.20 is commonly known as "signal equation".
After imposing the steady-state conditions, equation 4.18 becomes:

$$\omega_F - \omega_0 = \frac{1}{2\tau_p}\left[\alpha\, VScos\left(\omega_F\tau - \phi\right) + VSsin\left(\omega_F\tau - \phi\right)\right] \tag{4.21}$$

and phase excess equation for SD s-SNOM scheme can be straightforwardly retrieved:

$$\omega_F\tau = \omega_0\tau - \epsilon S\sqrt{1+\alpha^2}sin\left(\omega_F\tau - \phi + atan\left(\alpha\right)\right) \tag{4.22}$$

where

$$\epsilon = \frac{\tau}{\tau_c}\left(\frac{1-R}{\sqrt{R}}\right)\widetilde{a} \tag{4.23}$$

In Eq. 4.22 the modulus S and phase ϕ of the scattering coefficient σ explicitly appear; ϵ is an adimensional quantity which will have a relevant role in the following treatment in the weak feedback regime case.
Eqs. 4.20-4.22 are the starting point for the approach aimed to retrieve of the dieletric properties of the material sample in the very week and in the weak regime.

4.3 Theoretical results

In this section we want to present the results of a theoretical study of the SD s-SNOM in the very weak and weak regimes, based on the L-K Model modified with a complex scattering coefficient. In particular we retrieved some approximated formulas which allow a retrieval of the scattering coefficient σ and its harmonics in both these regimes. The determination of *sigma* is fundamental in order to obtain information about the optical properties of the analyzed material sample.

4.3.1 Very weak regime

Let us consider the very weak regime, which is characterized by values of the feedback parameter C<0.1. Taking as a starting point the steady-state solutions of the L-K model, Eqs. 4.20 and 4.22, it is possible to derive approximated expressions of modulus and phase of the scattering coefficient σ, valid in this regime. We assume that the frequency of the laser perturbed by the feedback, which we named ω_F, corresponds approximately to the unperturbed laser frequency ω_0. By implementing this hypothesis, and performing the calculations developed in Appendix C, we obtain the following expressions for the modulus S and the phase ϕ of the scattering coefficient σ:

$$S = \frac{1}{V}\sqrt{\Delta V^2 + \Delta V_{\frac{\pi}{2}}{}^2} \tag{4.24}$$

$$\phi = \omega_0\tau + atan\left[\frac{\Delta V_{\frac{\pi}{2}}}{\Delta V}\right] \tag{4.25}$$

where ΔV and $\Delta V_{\frac{\pi}{2}}$ are two values of the voltage signal obtained respectively for values of the distance laser target L and L+ΔL, with ΔL=$\frac{\lambda}{8}$, and λ is the wavelength of the light.
Equations 4.24 and 4.25 constitute a way to easily determine the complex scattering coefficient, and therefore in principle the dielectric properties of the sample known the tip characteristics, by exploiting only two signal measurements in two experimental configurations, i.e. for two different values of laser-tip distance. The complete derivation of these formulas is presented in Appendix C. We remark that neglection of the small variation of this distance due to the tip oscillation.
These two formulas are based on the approximated phase excess equation valid in very weak regime, Eq. C.2. The last detail that we want to remark is dependence of S on V: this constant can be determined only by measuring the attenuation factor $\tilde{a}$(see equation 4.2), which is not a quantity easily retrievable by experiments. In any case, this will yield a relative measure of optical contrast, so that it is not necessary to know the exact value of V.
As shown in Appendix C it is possible to show that in the same hypothesis the same relation between signals and scattering coefficient, expressed by Eqs. 4.24-4.25 occurs between the signal harmonics and the scattering coefficient harmonics:

$$s_n = \frac{1}{V}\sqrt{(\Delta V_n)^2 + (\Delta V_{\frac{\pi}{2}})_n{}^2} \tag{4.26}$$

$$\phi_n = \omega_0\tau + atan\left[\frac{(\Delta V_{\frac{\pi}{2}})_n}{\Delta V_n}\right] \tag{4.27}$$

where ΔV_n are the harmonics of the signal and s_n, ϕ_n are respectively modulus and phase of the harmonics of the scattering coefficient σ. The full derivation of Eqs. 4.26-4.27 is performed in Appendix C. These formulas have a fundamental

application role, because the harmonics of the voltage signal are the quantities which is possible to retrieve experimentally, since every SNOM setup provides a lock-in amplifier. Therefore, they can be directly used to process experimental data, in order to reconstruct the dielectric properties of the analyzed material.

4.3.2 Weak regime

The values of the feedback parameter C in the weak regime are included in the interval $]0.1, 1[$ and in this case it is not possible to assume that the interferometric fringes are sinusoidal and that ω_F and ω_0 have approximately the same value. In fact the presence of the feedback is not neglectable and its contribution must be considered. Therefore, we developed an approximated theory based on first order Taylor expansions, which brought us to obtain approximated formulas for the retrieval of modulus S and phase ϕ of the scattering coefficient in the weak regime:

$$S = \frac{1}{2V}\sqrt{(\Delta V - \Delta V_\pi)^2 + \left(\Delta V_{\frac{3\pi}{2}} - \Delta V_{\frac{\pi}{2}}\right)^2} \tag{4.28}$$

$$\phi = \omega_0\tau - atan\left(\frac{\Delta V_{\frac{3\pi}{2}} - \Delta V_{\frac{\pi}{2}}}{\Delta V - \Delta V_\pi}\right) \tag{4.29}$$

where ΔV, $\Delta V_{\frac{\pi}{2}}$, ΔV_π, $\Delta V_{\frac{3\pi}{2}}$ are four values of the voltage signal obtained for values of the distance laser target L+ΔL, with ΔL=0, $\frac{\lambda}{8}$, $\frac{\lambda}{4}$, $\frac{3\lambda}{8}$ respectively.
Equations 4.28 and 4.29 allow us to exploit four signals in four different experimental configurations(i.e. four different values of the laser-tip distance)in order to implement a retrieval of σ by a first order approximation.
It is possible also to prove that the same formula is valid also for the harmonics. In fact we can obtain the following equations:

$$s_n = \frac{1}{2V}\sqrt{((\Delta V_{\frac{3\pi}{2}})_n - (\Delta V_{\frac{\pi}{2}})_n)^2 + (\Delta V_n - (\Delta V_\pi)_n)^2} \tag{4.30}$$

$$\phi_n = \omega_0\tau - atan\left[\frac{(\Delta V_{\frac{3\pi}{2}})_n - (\Delta V_{\frac{\pi}{2}})_n}{\Delta V_n - (\Delta V_\pi)_n}\right] \tag{4.31}$$

They are valid in the weak regime and are based on first order approximations of Taylor expansions. As already mentioned for the very weak case, these equations where the harmonics of the signal appear at the right hand side can be used to process experimental data, in orer to retrieve the harmonics of the scattering coefficient.
The full derivation of the Eqs. 4.28-4.29 and Eqs. 4.30-4.31 is presented in Appendix D.

4.4 Numerical results

In the previous part of this chapter we introduced the LK model adapted for SD s-SNOM configuration, which is characterized by a complex scattering coefficient σ. This coefficient encompasses the information about the optical properties of the analyzed material sample, therefore its retrieval was a relevant part of our mathematical treatment, for very weak and weak feedback regimes. We developed a theory based on the steady states solutions of the LK equations, in order to obtain approximated expressions for the signal (i.e the voltage across the laser terminals), and then for modulus and phase of σ.
The results of the previous theoretical part have been exploited in order to process and analyze data obtained from experimental measurements, whose details are available in [54]. In this section we will present and discuss these results. A scheme of the experimental setup used for the measurements is shown in Fig. 4.2. It exploits a set of THz-QCLs operating in continuous wave regime at a certain driving current which is possible to tune, emitting at frequencies of 2.0 THz and 2.7 THz with peak powers at the temperature of 15 K of 5 mW and 4.2 mW, respectively.
The setup provides a lock-in amplifier, so that we can extract the harmonics of the signal. The Self-Mixing fringes are detected by varying the length of the external cavity, determined from the distance between the output facet of the laser and the tip.

4.4.1 Reproduction of experimental fringes in the weak regime and retrieval of the C paramater

The first part of this work consists of the analysis, by using a a THz-QCL with emission frequency 2.7 THz, of a 75 nm thick gold film evaporated on a Si undoped substrate with a 300 nm SiO_2 top layer. Firstly interferometric fringes are extracted for a fixed position at gold marker, by placing the tip in proximity of the sample, in tapping mode, with oscillation amplitude 280nm. The plot of the harmonics is shown in Fig. 4.3. We can observe that the shape of the fringes is asymmetric, showing that the experiment have been performed in a feedback regime not corresponding to the very weak regime, where we could expect sinusoidal shape of the curve, but in the weak regime with a C-parameter which has order of magnitude 10^{-1}. In order to better quantify the feedback level of the experiment, we simulated a SD s-SNOM setup by using a proper numerical code exploiting the same parameters of the experiment, with the aim of determining the C-parameter and the α factor of the laser. In our code, which solves the steady state equations of the model by using the Kliese Algorithm [35], C and α are input parameters. Therefore, we tried to find the couple (C, α) that gives simulated fringes that best reproduce the experimental curves shown in Fig. 4.3. In Fig. 4.4 normalized ex-

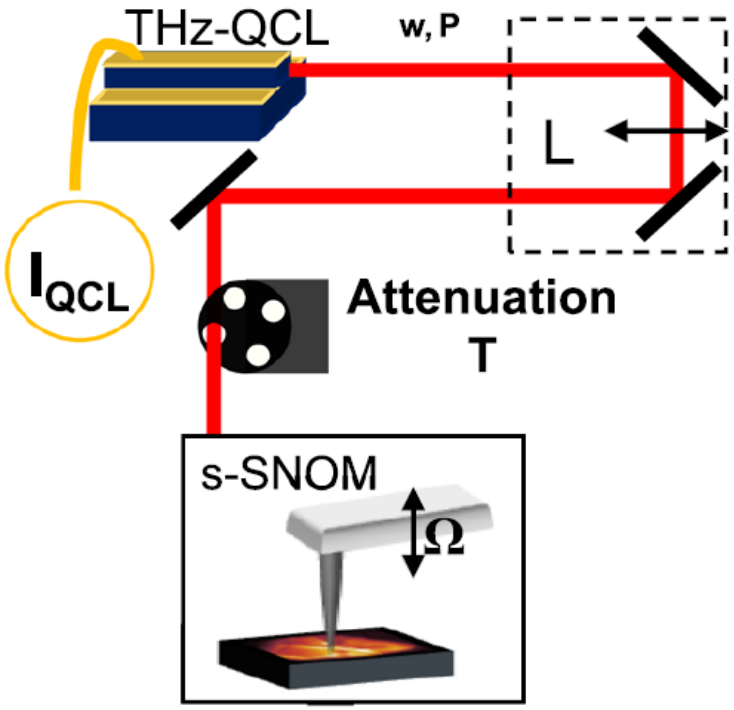

Figure 4.2: Sketch of the experimental setup exploited for the measurements analyzed and discussed in this chapter. A THz-QCL lasing emitting light at frequency ω, coupled to an s-SNOM providing an AFM tip oscillating at frequency Ω between 70 and 110 kHz. Parameters: P is the output power of the laser, I_{QCL} is the driving current, T is the transmission of the attenuators, and L is the variation of the optical path length achieved with an optical delay line. Reproduced from [54].

perimental (a) and simulated (b) harmonics at n=2,...,5 are shown. The curves in Fig. 4.4.b) have been obtained by setting C=0.5 and α =0.5. The extracted value of the C parameter confirms that we are in a weak regime and the value of the α = factor is in agreement with typical values of this parameters for THz QCLs.
Furthermore, we can notice that for harmonics orders n=2,...,5 the interferometric fringes present the same normalized shape, and this also occurs by looking at the simulated curves.

4.4.2 Dependence of the interferometric signal from injection current

By exploiting the same setup and the same sample of the previous subsection, we performed an investigation about the dependence of the SNOM signal on two

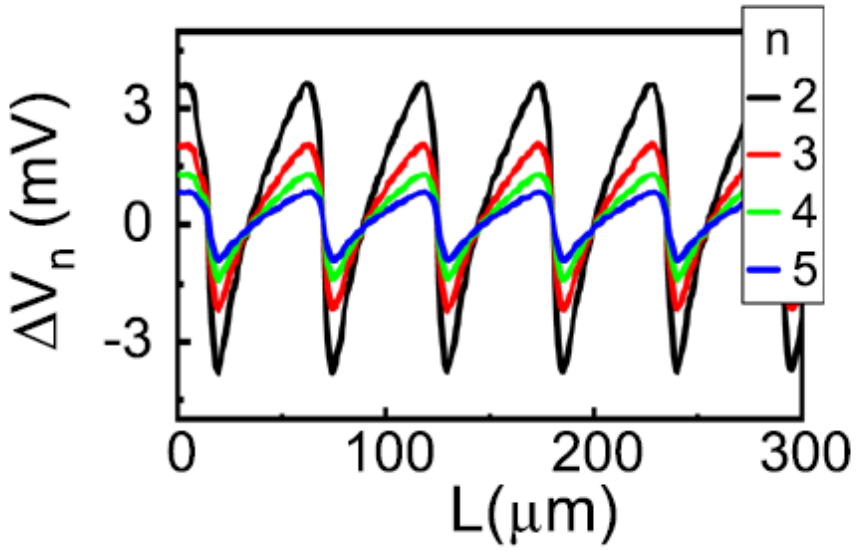

Figure 4.3: Harmonics of the signal extracted at a fixed position at gold marker, plotted as a function of the external cavity length variations at different demodulation orders n=2,...,5, obtained by exploiting a lock-in amplifier, at fixed values of transmissivity and injection current. Reproduced from [54].

key experimental parameters: the bias current of the QCL and the feedback intensity, i.e. the feedback transmissivity of the setup. The aim of this study is the identification of an operative regime which offers the best compromise of the SNR, phase sensitivity, and scan speed.
Two sets of measurements have been performed, by using two lasers with different emission frequency: 2.0 and 2.7 THz. We expect a reduction of the back-scattered field when the photon energy increases, considering the dependence of the scattering coefficient on the wavelength.

In Fig. 4.5.a) fringes at 2.7 THz are shown for different values of the current. The blue dots are the experimental points, while the red curves are the simulated ones, characterized by α=0.5 and C selected to best approximate each experimental curve. We chose to show the third harmonics because it results to be a good compromise between SNR and far-field background suppression. In Fig. 4.5.b) the same results are shown, but for frequency of the laser 2.0 THz.
The value of C as a function of the current for the two considered frequencies is shown in Fig. 4.6. At the lowest values of the current, near the laser threshold, for both the devices, the fringes have sinusoidal lineshape which is well-reproduced using a value of C<0.1, corresponding to very weak regime. At higher values of

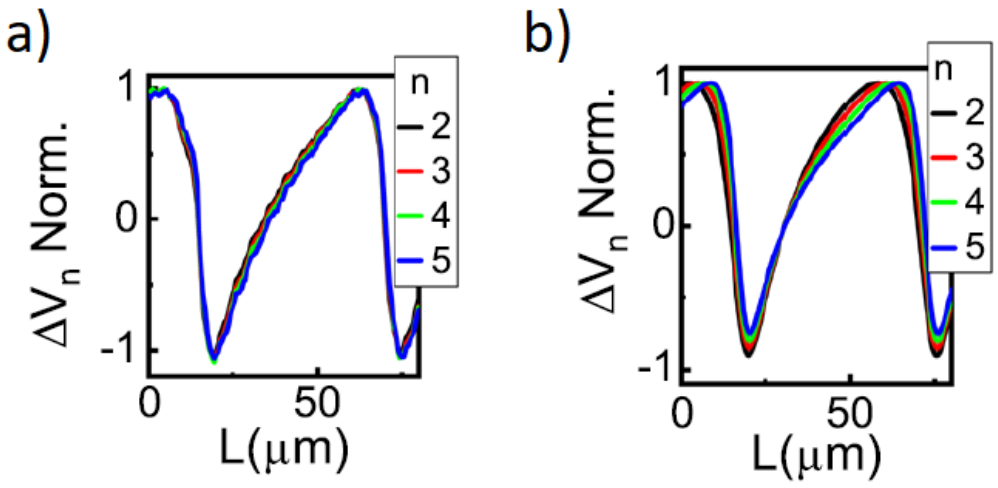

Figure 4.4: a) Normalized fringes of Fig. 4.3. b) Normalized fringes obtain by simulating a SD s-SNOM setup for C=0.5 and α =0.5. Reproduced from [54].

the bias current, the laser emitting at 2.7 THz presents asymmetric fringes and the values of the C are greater than 0.5, so that we can consider properly a weak regime.
The laser operating at 2.0 THz has a different behaviour. The fringes have a slight distortion by increasing the current, passing from C $<$ 0.05 to C=0.2 for the highest considered value.

4.4.3 Dependence of the interferometric signal from feedback intensity

In this subsection we study the behaviour of the laser in dependence on the feedback intensity, another key-parameter of our setup. We keep constant the bias current.
In Fig. 4.7 we show a set of interferometric fringes obtained by varying the transmission T of the attenuator placed in the setup, at the two considered values of the frequencies, 2.7 THz and 2 THz. T = 100 % corresponds to a situation where the filter wheel is removed from the optical path.
When we decrease the transmittance we report strong analogy with the behaviour observed by reducing the bias current (see Fig. 4.5. In fact the curves increase gradually their symmetry by reducing the feedback intensity until we have sinusoidal line shape in the very weak regime, achieved for T = 30% at both the values of the frequency.In Fig. 4.8 we can obserse a linear trend of the estimated C with the transmittance of the attenuator, as expected.

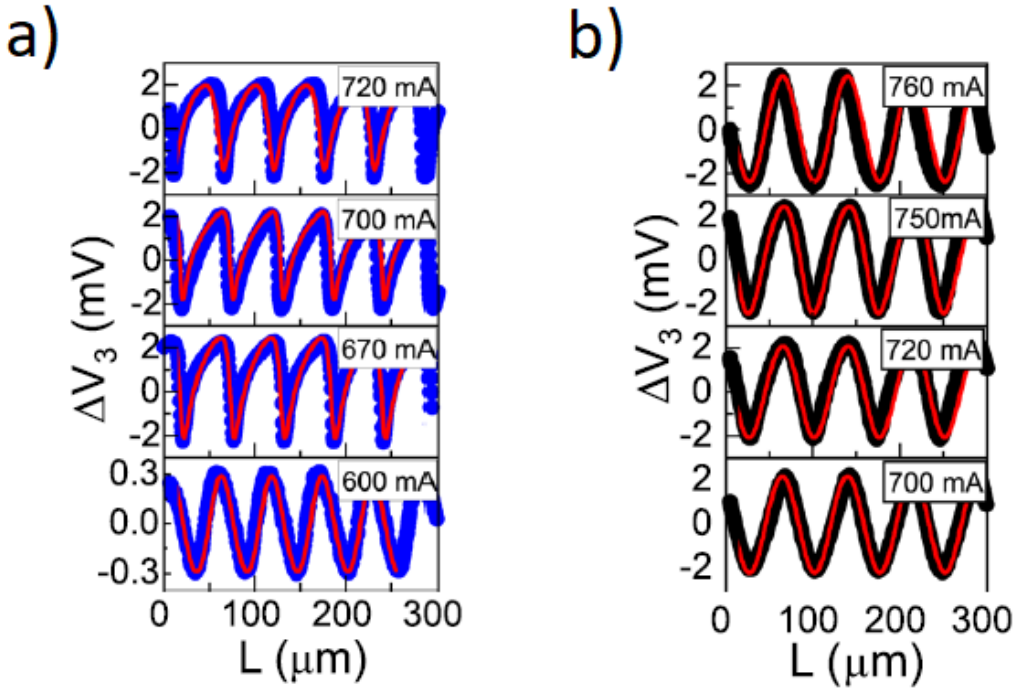

Figure 4.5: (a) and (b) interferometric fringes (third harmonic of the signal) at [blue dots, (a)] 2.7 THz and [black dots, (b)] 2.0 THz at different values of the bias current of the QCL together with the simulated curve (red solid lines) for $\alpha = 0.5$ and C parameter from bottom up equal to C = { 0.05, 0.5, 0.5, 0.63, 0.5} at 2.7 THz and C = $\{0.01, 0.05, 0.2, 0.5\}$ at 2.0 THz. Reproduced from [54].

4.4.4 Calculation of the scattering coefficient

In this part we want retrieve modulus and phase of the scattering coefficient harmonics σ_n by processing experimental measurements of interferometric signal, in order to explore the phase sentivity of a given material on the feedback. A sample of a topological insulator material named $Bi_2Te_{2.2}Se_{0.8}$ was used, since this material presents optical phonon resonances between 1.6 and 2.8 THz. We operate in this frequency range and we expect phase sensitivity in the measurements. The flake of $Bi_2Te_{2.2}Se_{0.8}$ is placed on an undoped silicon/silica substrate.
The measurement have been performed by moving on the sample along a line orthogonal to the flake/substrate interface, with steps of 30nm, acquiring at each position on the sample the interferometring fringes as a function of L. The fringe

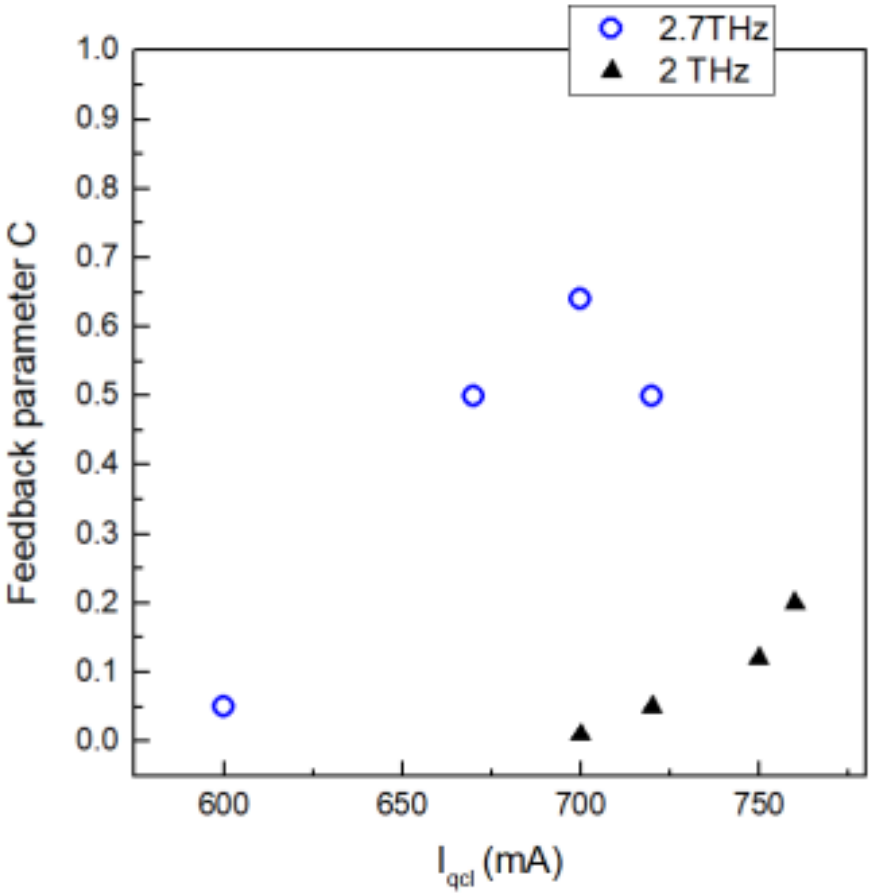

Figure 4.6: C-parameter selected to best reproduce the experimental SMI fringes, as a function of the current at 2.0 and 2.7 THz. Reproduced from [54].

maps as a function of L and X maps, acquired at 2.0 THz by setting the bias current at 700 mA and using a tip oscillation amplitude of 130 nm, are reported in [54] and [55].
An analysis of these fringes have been performed in order to retrieve the modulus and phase of the scattering coefficient harmonics, respectively s_n and ϕ_n, by using two methods. The first method is based on a fitting algorithm for each interferometric curve, based on the least squares method, by using a sinusoidal function. The second method exploits the first-order formulas retrieved in this chapter Eqs. D.44-D.45: for each value of X we select the third harmonic of signals at four different values of L, reciprocally phase shifted by $\pi/2$, corresponding to a displacement $\Delta L = \lambda/8$.

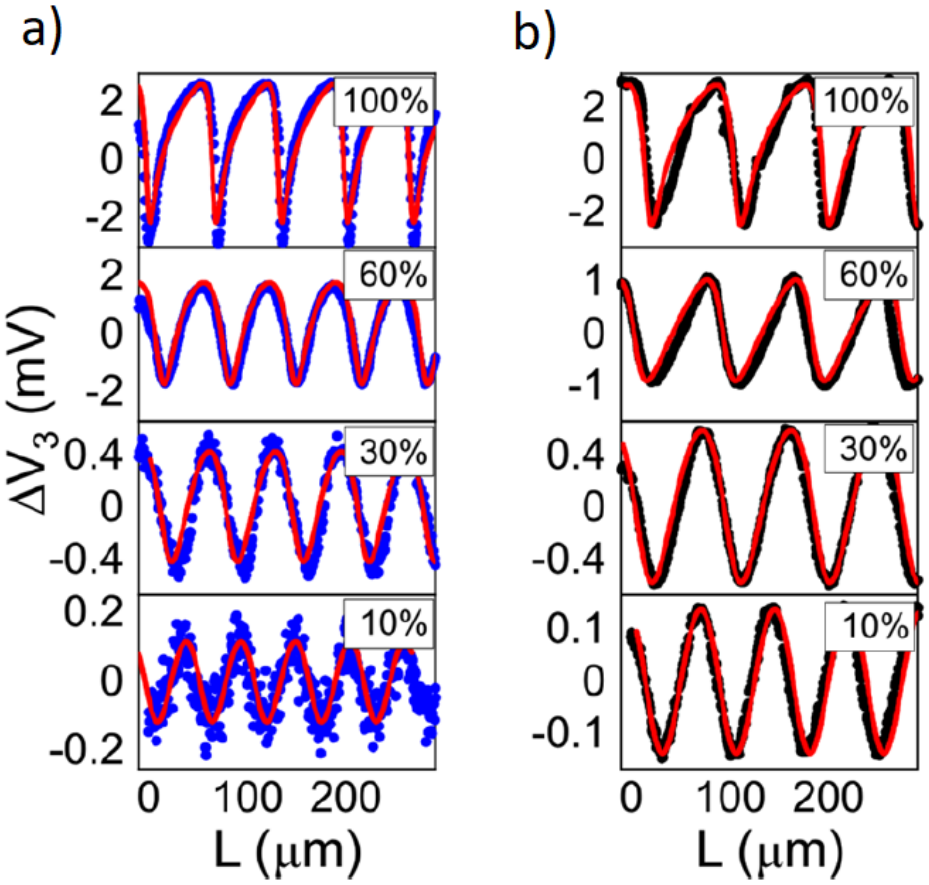

Figure 4.7: (a) and (b) interferometric fringes as a function of L, measured with attenuators of different transmission increasing from the lower to upper panels [blue dots, (a)] at 2.7 THz and [black dots, (b)] 2.0 THz together with the simulated curve (red solid lines) determined with $\alpha = 0.5$ and C parameters increasing linearly with the attenuator transmission. Reproduced from [54].

The amplitude and phase profiles obtained with the sinusoidal fit (dots) and first order formulas (solid lines) are shown in Fig. 4.9, showing a general agreement and equivalency between the two methods. The deviation observed for ϕ_3 at the lowest value of transmittance (T = 10%) can be related to the low SNR (<2) of the data, which affecting more the analysis with the approximated formula that exploits only four points in L. At the flake side, where the signal increases, we have total agreement between the two methods at T=10%.
We can conclude that for the analyzed case, the sinusoidal fit is an efficient method for the determination of modulus and phase of the scattering coefficient harmonic also in presence of a feedback level which we classify as weak regime, therefore

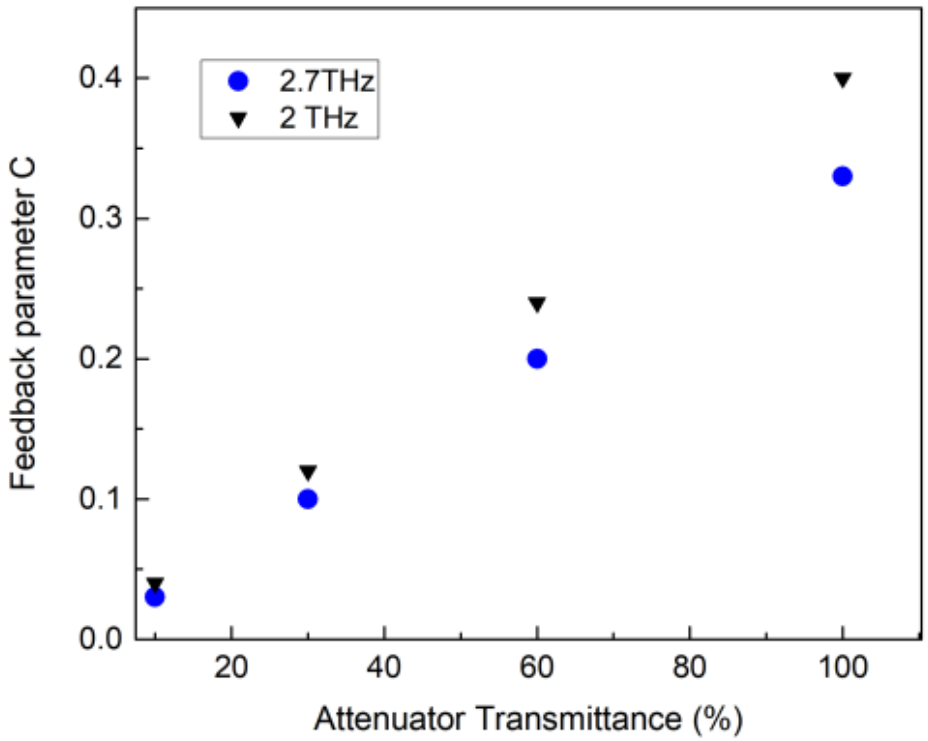

Figure 4.8: C-parameter selected to best reproduce the experimental SMI fringes, as a function of the attenuator transmittance at 2.0 and 2.7 THz. Reproduced from [54].

beyond the very weak regime, whose physical hypotheses have been exploited in the derivation of the method.

4.5 Conclusions

The study performed in this Chapter is based on a study of this configuration, which has been presented in Appendix C and D, by exploiting the LK model adapted for SD s-SNOM (with a complex scattering coefficient), and which has been applied for a numerical study and experimental data processing, with a particular focus on the weak regime. We found approximated expressions based on first order Taylor approximation, for the retrieval of the scattering coefficient valid in this regime, which allow us to have information about the optical susceptibility of the analyzed material. The comparison between the first order formulas and the zero order sinusoidal approximation of the sinusoidal fringes, both applied to

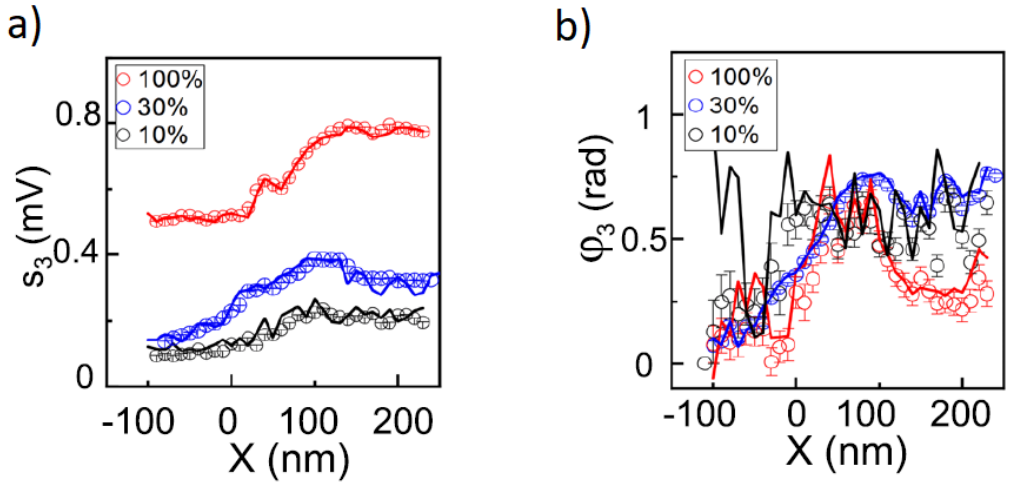

Figure 4.9: a) Modulus s_3 and b) phase of the third harmonic of the scattering coefficient for the considered $Bi_2Te_{2.2}Se_{0.8}$ flake placed on an undoped silicon/silica substrate, retrieved from the measured interferometric fringes by using sinusoidal fit (dots) and first-order Eqs. D.44-D.45 (solid lines), for three values of the attenuator transmittance: 10% (black), 30% (blue) and 100% (red). Reproduced from [54].

experimental data, did not highlight any relevant improvement in the passage from zero to first order, and therefore the sinusoidal fit can be an efficient method for the data analysis also in the weak regime. Furthermore, the numerical study performed on this configuration, allowed us to reproduce successfully experimental fringes in the weak regime and analyze their dependence on the bias current and the intensity of the feedback. We compared the numerical results with the experimental data, and we reproduce the measured curves. This showed the efficiency of the exploited numerical method.

Chapter 5

Conclusions

The purpose of this work was to study from a theoretical and numerical point of view the dynamics of QCLs in order to develop knowledge and methods useful for the design of device of this type suitable for applications in the field of photonics and material analysis. In particular two main topics have been object of study in this thesis: the self-generation of OFCs and the SD s-SNOM. In the first case we studied the dynamics of QCLs in absence of optical feedback; in the second case we analyzed a configuration where laser is subjected to optical feedback, which is exploited for the retrieval of the optical properties of a given material.
Firstly we considered the QCL with a FP cavity and we worked on the modeling of this configuration for its multi-mode emission, with the aim to investigate the spontaneous generation of OFCs. The result of this theoretical study is a full model named Effective Semiconductor Maxwell-Bloch Equations. This model consists of a nonlinear system of six equations: two for the electric field, two for the polarization terms, and two for the carrier density. This model, although it relies on the Maxwell-Bloch formalism, does not exploit the properties of a two level system, but is based on a dielectric susceptibility which reproduces the main characteristics of semiconductors, such as the existence of an alpha-factor, the asymmetric gain profile and the dependence of the gain/dispersion on the carrier density. Furthermore, the phenomenon of the Spatial-Hole burning, which characterizes the FP cavity, is introduced, and therefore backward and forward electric fields appear in the equations.
A numerical and simulation study of these equations has been performed, in order to investigate the multi-mode regimes of QCL and verify if this model is able to reproduce the main experimental results. In order to rigorously classify the different regimes obtained from the simulations, we introduced some indicators for phase and intensity noise, whose values under a certain threshold allow us to define a regime as an OFC. Also an indicator for the linear chirp has been introduced, motivated by the experimental evidence of this behaviour in the locked regimes of the laser. The simulations highlighted that this model is able to reproduce the alternance

between comb and no comb regimes which has been reported in the literature as a typical experimental feature of the QCL multi-mode dynamics. Furthermore, we also found out that the regimes characterized by high number of locked modes (approximately more than seven modes) present an instantaneous frequency with a linear chirp behaviour.
Moreover we investigated the role of some parameters appearing in the ESMBEs, such as the alpha-factor, the homogeneous gain bandwidth and carrier lifetime. It came out that a large alpha-factor increases the phase-amplitude correlation increases, as the modal competition, and therefore the possibility to have comb regimes decreases. Also, an increase of the gain/dispersion bandwith implies a higher number of modes in the optical spectrum and therefore, for suitable values of the bias current and of the other parameters, a higher number of locked modes. The carrier lifetime is also a relevant factor. In fact by reducing the carrier lifetimes, we report a relevant increase of the number of modes, an increase of the locking current interval and also a chirp behaviour closer to an ideal sawtooth signal (lower value of the chirp indicator).
In the following we worked on the multimode dynamics of QCL with a ring cavity. Also in this case we introduced a model based on ESMBEs and we performed a simulation study of such a nonlinear system, highlighting the reproduction of experimental findings such as the alternance between locked and unlocked states and the absence of linear chirp. Furthermore, we retrieved a reduced model for ring QCL consisting of a single master equation, valid in near threshold operation and fast carriers hypotheses. A linear stability analysis of this equation has been performed and we compared the stability scenario of the reduced model with the results of the full model (ESMBEs), finding out a general agreement between them also for values of the bias current considerably above the laser threshold.
We also studied the ring QCL in presence of optical injection. The main aim of this study was the description of a bistable regime of this configuration. We reproduced successfully some interesting regimes experimentally found in this scheme, such as cavity solitons and Turing rolls.
The last part of this work was dedicated to the dynamics of QCLs in presence of feedback. In particular, we studied the SD s-SNOM, which is a nanoscopy technique combining the SMI with the s-SNOM, and provides a material analysis with resolution on nanoscopic scale by exploiting an AFM tip and the near-field interaction mediated by evanescent waves between this probe and the material specimen. This technique is applied in the Terahertz region, and therefore allows the study of materials which have resonances (for instance phonon resonances) and interesting features in this spectral region. Firstly a theoretical study of this configuration has been performed, by analyzing and manipulating the LK equations adapted for this configuration. This theoretical study is mainly focused on the weak-feedback regime, which corresponds to the 10^{-1} order of magnitude for the values of the C parameter. We derived first order approximated expressions for the interferometric

signal and for the scattering coefficient valid in this regime, which allow us to retrieve the information about the optical properties of the analyzed material. These first order approximated formulas have been used for processing experimental data. We also performed a comparison with the results obtained by using zero order formulas based on sinusoidal approximation of fringes and from this study it came out that in the specific studied case, there is no relevant improvement passing from zero to first order, and therefore the sinusoidal fit is still an efficient method for the data analysis.
We also performed a numerical study on this configuration, successfully reproducing experimental fringes in the weak regime and retrieving the C parameter for each set of experimental data. Our algorithm for the simulation of SD s-SNOM was also applied in order to study the dependence on experimental fringes from two relevant parameters: the bias current and the intensity of the feedback. Also in this case we compared our results with the experimental data, and we were able to reproduce the measured curves, proving then the efficiency of the exploited numerical method.
Further steps can be done in the future to improve this study. Firstly a reduced model for the free running FP configuration can be introduced and numerically studied in order to have a broader understanding of the physics of this configuration. Furthermore, also the addition of the optical injection in the FP case can reveal interesting new properties and explain some experimental achievements.

Future perspectives

Several perspectives can be considered for future studies in the field of the QCL dynamics, considering the models and the results of this work as a starting point. In particular, the model of ESMBEs, introduced and used in this thesis for the modeling of the self-generation of OFCs in FP and ring QCLs, can also be exploited to study the behaviour of this laser in case of electrical injection, i.e. when an RF modulation of the bias current is performed. Furthermore, the study of a FP QCL in presence of optical injection by exploiting the full model of the ESMBEs, would be an interesting research topic that could be developed in future, with the initial aim to compare the simulation results with the available experimental evidences, and also to develop a further comparison with the behaviour of the ring QCL in the same configuration.
Regarding the study of the SD s-SNOM, in this work the very weak and the weak regime of feedback have been considered. The analysis of regimes with higher level of feedback, as the moderate regime, would be useful in order to exploit this setup with a higher SNR. A treatment of the LK model with complex scattering coefficient for the retrieval of approximated formulas in the moderate regime, therefore, would constitute a relevant improvement in terms of contrast, in order to perform

nanoscopic analysis of the dielectric properties of materials resonant in the THz region.

Appendix A

Reduced Model for the Fabry-Perot configuration

In the section 2.2 we derived the ESMBEs (2.22-2.27) with the proper boundary conditions (2.28)-(2.29). This model encompasses the full dynamics of field and medium and is characterized by a relevant number dynamical variables, implying that the time needed for completing a simulation is quite long. The order of magnitude of the simulation time is 10 hours for a 300ns simulation.
Another disadvantage of the full model is the difficulty to have an immediate outline of the physical meaning of the terms appearing in the equations, because we have six nonlinear equations in six variables.
For these reasons it is desirable to obtain a reduced model, valid under certain approximations, where the equations and the associated numerical load can be simplified. In this section we derive a reduced model for FP configuration composed by two master equations, for the forward and backward fields, valid under some approximation that will be specified in the following. The used approach is applied in the literature for lasers and for the description of active and passive optical systems, and exploits methods proposed for the simplification and treatment of FP resonator. Furthermore, it leads do describe this optical system by using the Lugiato-Lefever equation, that is a prototypical equation for describing structure localization in passive nonlinear optical resonators and has been recently extended to the description of soliton formation in QCL [38], [34], [10], [39].

A.1 Derivation of the reduced model in the Fabry-Perot configuration

We want to retrieve a reduced model for FP configuration, starting from the complete model and introducing some hypotheses. In particular, we assume fast dynamics of the carriers, which corresponds to the case of QCL, and near threshold

operation. Let us first consider the equation for the Forward field, Eq. 2.22. We multiply both sides of this equation by the group velocity v, obtaining:

$$v\frac{\partial E^+}{\partial z} + \frac{\partial E^+}{\partial t} = -v\frac{\alpha_L}{2}E^+ + vgP_0^+ \tag{A.1}$$

Then we define photon lifetime as:

$$\tau_p = (v\alpha_L/2)^{-1} \tag{A.2}$$

If we multiply both sides of Eq. A.1 by the polarization dephasing time τ_d and we introduce also the definition given by Eq. A.2 we have:

$$v\tau_d\frac{\partial E^+}{\partial z} + \tau_d\frac{\partial E^+}{\partial t} = -\frac{\tau_d}{\tau_p}E^+ + \tau_d vgP_0^+ \tag{A.3}$$

At this point we introduce the following dimensionless space and time variables:

$$\eta = \frac{z}{v\tau_d}, \tag{A.4}$$

$$t' = \frac{t}{\tau_d} \tag{A.5}$$

and the parameter:

$$\sigma = \frac{\tau_d}{\tau_p} \tag{A.6}$$

We obtain, then:

$$\frac{\partial E^+}{\partial \eta} + \frac{\partial E^+}{\partial t'} = \sigma\left[-E^+ + \tau_p vgP_0^+\right] \tag{A.7}$$

Now let us consider and manipulate the equations for polarization and carriers. First we consider Eq. 2.24, for the polarization envelope P_0^+. Let us multiply both the sides of this equation by τ_d. We obtain:

$$\frac{\partial P_0^+}{\partial t'} = \Gamma(1+i\alpha)\left[-P_0^+ + if_0\epsilon_0\epsilon_b(1+i\alpha)\left(N_0E^+ + N_1^+E^-\right)\right], \tag{A.8}$$

Then we consider Eq. 2.26, for the carrier envelope N_0, and also in this case we multiply both sides of this equation by τ_d:

$$\frac{\partial N_0}{\partial t'} = \frac{I\tau_d}{eV} - \frac{\tau_d N_0}{\tau_e} + \frac{i\tau_d}{4\hbar}\left[E^{+*}P_0^+ + E^{-*}P_0^- - E^+P_0^{+*} - E^-P_0^{-*}\right], \tag{A.9}$$

Let us define:

$$b = \frac{\tau_d}{\tau_e}, \tag{A.10}$$

$$n_0 = N_0V, \tag{A.11}$$

$$n_1 = N_1V. \tag{A.12}$$

Eq. A.9 becomes:

$$\frac{\partial n_0}{\partial t'} = b\left[\frac{I\tau_e}{e} - n_0 + \frac{iV\tau_e}{4\hbar}\left(E^{+*}P_0^+ + E^{-*}P_0^- - E^+P_0^{+*} - E^-P_0^{-*}\right)\right] \tag{A.13}$$

We consider now Eq. A.15 and we introduce:

$$f_0' = \frac{f_0}{V} \tag{A.14}$$

and we obtain:

$$\frac{\partial P_0^+}{\partial t'} = \Gamma(1+i\alpha)\left[-P_0^+ + if_0'\epsilon_0\epsilon_b\,(1+i\alpha)\left(N_0E^+ + N_1^+E^-\right)\right] \tag{A.15}$$

At this point we introduce the new dimensionless dynamical variables:

$$F^+ = \sqrt{\frac{V\tau_e f_0'\epsilon_0\epsilon_b}{4\hbar}}E^+, \tag{A.16}$$

$$F^- = \sqrt{\frac{V\tau_e f_0'\epsilon_0\epsilon_b}{4\hbar}}E^-, \tag{A.17}$$

$$p^+ = i\sqrt{\frac{V\tau_e f_0'\epsilon_0\epsilon_b}{4\hbar}}P_0^+, \tag{A.18}$$

$$p^- = i\sqrt{\frac{V\tau_e f_0'\epsilon_0\epsilon_b}{4\hbar}}P_0^-, \tag{A.19}$$

$$d_0 = f_0'\epsilon_0\epsilon_b n_0, \tag{A.20}$$

$$d_1^+ = f_0'\epsilon_0\epsilon_b n_1^+ \tag{A.21}$$

and the the pump parameter:

$$\mu = f_0'\epsilon_0\epsilon_b\frac{I\tau_e}{e} \tag{A.22}$$

We can write then the equations for p^+, d_0 and d_1^+:

$$\frac{\partial p^+}{\partial t'} = \Gamma(1+i\alpha)\left[-p^+ - (1+i\alpha)\left(d_0F^+ + d_1^+F^-\right)\right], \tag{A.23}$$

$$\frac{\partial d_0}{\partial t'} = b\left[\mu - d_0 + F^{+*}p^+ + F^{-*}p^- + F^+p^{+*} + F^-p^{-*}\right] \tag{A.24}$$

$$\frac{\partial d_1^+}{\partial t'} = b\left[-d_1^+ + F^{-*}p^- + F^+p^{-*}\right] \tag{A.25}$$

We introduce now quantity:

$$A = \frac{v\tau_p\omega_0N_P\Gamma_C}{2\epsilon_0nc} \tag{A.26}$$

and rewrite the equations for forward and backward field:

$$\frac{\partial F^+}{\partial \eta} + \frac{\partial F^+}{\partial t'} = \sigma\left[-F^+ - Ap^+\right] \tag{A.27}$$

$$-\frac{\partial F^-}{\partial \eta} + \frac{\partial F^-}{\partial t'} = \sigma\left[-F^- - Ap^-\right] \tag{A.28}$$

Finally, if we recall:

$$P^+ = Ap^+ \tag{A.29}$$

$$P^- = Ap^- \tag{A.30}$$

$$D_0 = Ad_0 \tag{A.31}$$

$$D_1^+ = Ad_1^+ \tag{A.32}$$

$$D_1^- = Ad_1^- \tag{A.33}$$

we can rewrite ESMBEs as:

$$\frac{\partial F^+}{\partial \eta} + \frac{\partial F^+}{\partial t'} = \sigma\left[-F^+ - p^+\right] \tag{A.34}$$

$$-\frac{\partial F^-}{\partial \eta} + \frac{\partial F^-}{\partial t'} = \sigma\left[-F^- - p^-\right] \tag{A.35}$$

$$\frac{\partial P^+}{\partial t'} = \Gamma(1+i\alpha)\left[-P^+ - (1+i\alpha)\left(D_0F^+ + D_1^+F^-\right)\right], \tag{A.36}$$

$$\frac{\partial P^-}{\partial t'} = \Gamma(1+i\alpha)\left[-P^- - (1+i\alpha)\left(D_0F^- + D_1^-F^+\right)\right], \tag{A.37}$$

$$\frac{\partial D_0}{\partial t'} = b\left[\mu - D_0 + F^{+*}p^+ + F^{-*}P^- + F^+P^{+*} + F^-P^{-*}\right] \tag{A.38}$$

$$\frac{\partial D_1^+}{\partial t'} = b\left[-D_1^+ + F^{-*}P^- + F^+P^{-*}\right] \tag{A.39}$$

The equation for D_1^- is the complex-conjugate of the equation A.39.
At this point we introduce the smallness parameter

$$\epsilon = \sqrt{\sigma} \tag{A.40}$$

and we assume fast carriers and near threshold operation. Therefore we can write:

$$F^\pm = \varepsilon\ F^{(1)\pm} + O(\varepsilon^2) \tag{A.41}$$

$$P^\pm = \varepsilon\ P^{(1)\pm} + O(\varepsilon^2) \tag{A.42}$$

$$D_0 = 1 + \varepsilon^2 D_0^{(2)} + O(\varepsilon^3) \tag{A.43}$$

$$D_1{}^\pm = \varepsilon^2\ D_1{}^{(2)\pm} + O(\varepsilon^3) \tag{A.44}$$

$$\mu = 1 + \varepsilon^2\mu^{(2)} + O(\varepsilon^3) \tag{A.45}$$

The expansion of μ in Eq. A.45 corresponds to the implementation of the hypothesis of near threshold operation. Furthermore, in order to have derivatives of order O(1), we assume that the following Taylor expansions hold:

$$\frac{\partial}{\partial t'} = \frac{\partial}{\partial t'^{(0)}} + \varepsilon^2 \frac{\partial}{\partial t'^{(2)}} + O(\varepsilon^3) \tag{A.46}$$

$$\frac{\partial}{\partial \eta} = \frac{\partial}{\partial \eta^{(0)}} + \varepsilon^2 \frac{\partial}{\partial \eta^{(2)}} + O(\varepsilon^3) \tag{A.47}$$

By introducing the expansion Eq. A.46, we can rewrite the equation Eq. A.34 for the forward field:

$$\varepsilon \frac{\partial F^{(1)+}}{\partial \eta^{(0)}} + \varepsilon^3 \frac{\partial F^{(1)+}}{\partial \eta^{(2)}} + \varepsilon \frac{\partial F^{(1)+}}{\partial t'^{(0)}} + \varepsilon^3 \frac{\partial F^{(1)+}}{\partial t'^{(2)}} = \varepsilon^2 \left[-\varepsilon\ F^{(1)+} - \varepsilon\ P^{(1)+} \right] \tag{A.48}$$

At first order in ϵ we have:

$$\frac{\partial F^{(1)+}}{\partial \eta^{(0)}} = -\frac{\partial F^{(1)+}}{\partial t'^{(0)}} \tag{A.49}$$

Now let us consider the equation for P^+, Eq. A.37 and let us introduce the expansions Eqs. A.46-A.47 into it. We have at first order in ϵ:

$$\varepsilon \frac{\partial P^{(1)+}}{\partial t'^{(0)}} = \Gamma(1+i\alpha) \left\{ -\varepsilon\ P^{(1)+} - (1+i\alpha)\, \varepsilon\ F^{(1)+} \right\} \tag{A.50}$$

and then:

$$\left[1 + \frac{1}{\Gamma(1+i\alpha)} \frac{\partial}{\partial t'^{(0)}} \right] \varepsilon P^{(1)+} = -\,(1+i\alpha)\, \varepsilon\ F^{(1)+} \tag{A.51}$$

If we solve Eq. A.51 in the Fourier domain we obtain:

$$\left[1 + \frac{i\omega}{\Gamma(1+i\alpha)} \right] \hat{P}^{(1)+} = -\,(1+i\alpha)\ \ \hat{F}^{(1)+} \tag{A.52}$$

By introducing the additional hypothesis that $\omega/\Gamma << 1$:

$$P^{(1)+} = -\,(1+i\alpha)\ \ F^{(1)+} \tag{A.53}$$

Using Eq. A.53 we get from Eqs. A.38-A.39:

$$D_1{}^{(2)\pm} = -2F^{(1)\mp *} F^{(1)\pm} \tag{A.54}$$

$$D_0 = \mu - 2\left(|F^+|^2 + |F^-|^2 \right) \tag{A.55}$$

By solving in the Fourier domain Eq. A.37:

$$\left[1+\frac{i\omega}{\Gamma(1+i\alpha)}\right]\hat{P}^{+}=-\left(1+i\alpha\right)\ \left(D_0F^{\pm}+D_1{}^{\pm}F^{\mp}\right) \tag{A.56}$$

and using the Taylor expansion of $(1+x)^{-1}$ truncated at the second order we have:

$$\begin{aligned}\hat{P}^{+}=&-\mathcal{F}\left[\left(1+i\alpha\right)\varepsilon F^{(1)+}\left[\mu-2\varepsilon^{2}\left[|F^{(1)+}|^{2}+|F^{(1)-}|^{2}\right]\right]\right.\\&\left.+\mathcal{F}\left(\varepsilon^{2}\left(1+i\alpha\right)\varepsilon^{2}F^{(1)+}|F^{(1)-}|^{2}\right)\left[1-\frac{i\omega}{\Gamma\left(1+i\alpha\right)}-\frac{\omega^{2}}{\Gamma^{2}\left(1+i\alpha\right)^{2}}\right]+O(\varepsilon^{4})\right.\end{aligned} \tag{A.57}$$

Where $\mathcal{F}$ denote here the Fourier transform. Anti-transforming both sides of Eq. A.57 and inserting into Eq. A.48 and using Eq. A.49, we obtain:

$$\begin{aligned}&\frac{\partial F^{+}}{\partial\eta}+\frac{\partial F^{+}}{\partial t'}\\&\quad=\sigma\left[\left(\mu-1+i\alpha\mu\right)F^{+}-2\left(1+i\alpha\right)\left(|F^{+}|^{2}+2|F^{-}|^{2}\right)+\left(\frac{1}{\Gamma^{2}\left(1+i\alpha\right)}\right)\frac{\partial^{2}F^{+}}{\partial\eta^{2}}\right]\end{aligned} \tag{A.58}$$

Following the same mathematical treatment also for the backward field we obtain

$$\begin{aligned}&-\frac{\partial F^{-}}{\partial\eta}+\frac{\partial F^{-}}{\partial t'}\\&\quad=\sigma\left[\left(\mu-1+i\alpha\mu\right)F^{-}-2\left(1+i\alpha\right)\left(|F^{-}|^{2}+2|F^{+}|^{2}\right)+\left(\frac{1}{\Gamma^{2}\left(1+i\alpha\right)}\right)\frac{\partial^{2}F^{+}}{\partial\eta^{2}}\right]\end{aligned} \tag{A.59}$$

Eqs. A.58-A.59 are the reduced model for the FP configuration, with boundary conditions:

$$F^{-}(L',t') = \sqrt{R}F^{+}(L',t'), \tag{A.60}$$

$$F^{+}(0,t') = \sqrt{R}F^{-}(0,t'), \tag{A.61}$$

where the boundaries of η are in agreement with Eq. A.4.

Appendix B

Lugiato-Lefever Equation for the Fabry-Perot configuration

In this subsection we want to unite equations for forward and backward fields in a single spatiotemporal equation. We will follow the approach of [11] which consists in the introduction of a cavity folding where an auxiliary field is defined with a consequent derivation of a single equation. In [11] this method is applied to the 2-level system. In our treatment we will apply the same procedure to the description of a FP-QCL.
Let us consider the Eq. A.58 and let us introduce the following modal expansion of the fields F^+ and F^-, with modal amplitudes $f_n\prime$:

$$F^+(\eta, t') = \sum_{n=-\infty}^{+\infty} f'_n(t)\, e^{i\alpha_n \eta} \tag{B.1}$$

$$F^-(\eta, t') = \sum_{n=-\infty}^{+\infty} f'_n(t)\, e^{-i\alpha_n \eta} \tag{B.2}$$

where $\alpha_n = n\pi v\tau_d/L$. By exploiting these expansions we can extend F^+ and F^- to the interval $\eta \in [-\frac{L}{v\tau_d}; \frac{L}{v\tau_d}]$, by using these definitions in the interval $[-\frac{L}{v\tau_d}; 0]$: $F^+(\eta, t') = F^-(-\eta, t')$ and $F^-(\eta, t') = F^+(-\eta, t')$.
Therefore the forward and backward field obey periodic boundary conditions in the interval $[-\frac{L}{v\tau_d}; 0]$.
We can obtain the modal amplitudes by using these formulas:

$$f'_n(t') = \frac{1}{2L'}\int_{-L'}^{L'} d\eta e^{-i\alpha_n\eta} F^+(\eta, t') = \frac{1}{2L'}\int_{-L'}^{L'} d\eta e^{i\alpha_n\eta} F^-(\eta, t') \tag{B.3}$$

where $L' = \frac{L}{v\tau_d}$.

If we use Eqs. B.1-B.3, Eq. A.58 becomes:

$$\begin{aligned}&\frac{1}{\sigma}\left[\frac{df'_n}{dt'}+i\alpha_n f'_n\right]=(\mu-1+i\alpha\mu)\,f'_n\\&-2\,(1+i\alpha)\sum_{n',n''}f'_{n'}f'^{*}_{n''}\left(f'_{n-n'+n''}+2f'_{-n+n'+n''}\right)+\left(\frac{-\alpha^2{}_n}{\Gamma^2\,(1+i\alpha)}\right)f'_n\end{aligned}\tag{B.4}$$

We now introduce the f_n defined by:

$$f_n=f\prime_n e^{+i\alpha_n t'}\tag{B.5}$$

Introducing Eq. B.5 in Eq. B.4 we have:

$$\begin{aligned}&\frac{1}{\sigma}\frac{df_n}{dt'}=(\mu-1+i\alpha\mu)\,f'_n\\&-2\,(1+i\alpha)\sum_{n',n''}f_{n'}f^{*}_{n''}\left(f_{n-n'+n''}+2f_{-n+n'+n''}e^{2i(\alpha_n-\alpha_{n'}t')}\right)+\left(\frac{-\alpha^2{}_n}{\Gamma^2\,(1+i\alpha)}\right)f_n\end{aligned}\tag{B.6}$$

If we average Eq. B.6 over a time interval longer than the cavity roundtrip and shorter than cavity decay time, we obtain (see [11]):

$$\begin{aligned}&\frac{1}{\sigma}\frac{df_n}{dt'}=(\mu-1+i\alpha\mu)\,f'_n\\&-2\,(1+i\alpha)\left[\sum_{n',n''}f_{n'}f^{*}_{n''}f_{n-n'+n''}+2\sum_{n'}f_{n'}f^{*}_{n'}\right]+\left(\frac{-\alpha^2{}_n}{\Gamma^2\,(1+i\alpha)}\right)f_n\end{aligned}\tag{B.7}$$

Equation B.7 is the LLE equation for a FP QCL.

Appendix C

Theoretical Study of the Very Weak Regime

C.1 Retrieval of the scattering coefficient

This Appendix is dedicated to the retrieval of the scattering coefficient in the very weak regime of feedback, i.e. for C <0.1. For further details about the theory in the very weak regime, see [21], where this theory has been developed and published for the first time for SD s-SNOM.
We will derive exact relations linking Modulus S and phase ϕ of the scattering coefficient σ with two independent measures of self-mixing signal, by using the fact that the perturbation of the laser frequency due to the presence of feedback is negligible in this regime. We underline again that the scattering coefficient is a quantity that contains the information about the optical properties of the analyzed material.
The Equations 4.20 and 4.22, i.e. the steady-state solutions of the LK model adapted for SD s-SNOM configuartion, are the starting point of the derivation.
As already mentioned, in presence of a very weak feedback, it is possible to assume that the emission frequency of the laser subject to optical feedback ω_F is approximately equal to the frequency of the unperturbed laser ω_0. This assumption is valid only in this regime, and allows to obtain in a straightforward manner an explicit dependence of S and ϕ on the voltage signal. According to this assumption, equations 4.20 and 4.22 become:

$$\Delta V \approx VScos(\Phi) \tag{C.1}$$

$$\omega_F \approx \omega_0 \tag{C.2}$$

where

$$\Phi = \omega_0 \tau - \phi \tag{C.3}$$

We remind that the external cavity roundtrip τ is in principle time-dependent, since it depends on the laser-tip distance L through the Equation 1.4 and tip is

oscillating. In this theory we assume to neglect the change of L due to the tip oscillation. In fact, while the laser-tip distance is on the scale of 10^1 cm in typical experiments (60 cm in [21]), the oscillation extension of the tip rarely exceeds a few hundreds of nanometers. So, in terms of phase change as given by C.3, the quantity L can be taken constant.
Considering Eq. C.1 we see that both S and ϕ appear in the right hand side, so that one measurement of ΔV is not enough to extract info about both.
Therefore it is necessary to introduce a distance variation ΔL so that Φ has a shift $\Delta\Phi$. If we now assume to perform two detections of the voltage signal, the first at L and the second at L+ΔL and taking ΔL so that ϕ=$\frac{\pi}{2}$, we can easily see that the shifted signal will be given by:

$$\Delta V_{\frac{\pi}{2}} = VScos\left(\Phi + \frac{\pi}{2}\right) = -VSsin\left(\Phi\right) \tag{C.4}$$

A phase shift of $\frac{\pi}{2}$ corresponds to a distance variation of $\frac{\lambda}{8}$.
By using fundamental trigonometry it is possible to straightforwardly retrieve the scattering coefficient modulus S:

$$S = \frac{1}{V}\sqrt{\Delta V^2 + \Delta V_{\frac{\pi}{2}}{}^2} \tag{C.5}$$

The explicit expression of S as a function of the signals is the first formula that we wanted to obtain by developing this theory. We pass now the retrieval of the phase. If S is known, also cos(Φ) and sin(Φ) can be retrieved respectively from equations C.1 and C.4, so that Φ is fully determined. It is also possible to express Φ:

$$\Phi = -atan\left[\frac{\Delta V_{\frac{\pi}{2}}}{\Delta V}\right] \tag{C.6}$$

where we consider the the extension of the arc tangent to the interval [0,2π], called arc tangent2 (atan2). Inverting the equation C.3, the phase ϕ of the scattering coefficient is finally found:

$$\phi = \omega_0\tau + atan\left[\frac{\Delta V_{\frac{\pi}{2}}}{\Delta V}\right] \tag{C.7}$$

Equations C.5 and C.7 correspond to Eqs. 4.24-4.25, presented in Chapter 4.

C.2 Retrieval of the scattering coefficient harmonics

Since in every SD s-SNOM experimental setup is always present a lock-in amplifier, the quantities that can be experimentally measured are not directly the signals

(voltage across the laser terminals), but their harmonics. Therefore, it is relevant to retrieve the the harmonics of interferometric signals, in order to reconstruct the information about the optical properties of the sample. More specifically, we want to find a relation linking the harmonics of the signals to σ_n, i.e. the harmonics of the scattering coefficient. In the mathematical treatment developed in this section, the near-field scattering is modeled according to the finite-dipole model.The tip-sample surface distance z(t) oscillates with frequency Ω between 0 and $2z_A$ as

$$z(t) = z_A(1 + cos\Omega t) \tag{C.8}$$

z(t) is then an even periodic function of the time, with period $\frac{2\pi}{\Omega}$.It is possible to demonstrate that also the scattering coefficient σ is an even periodic function of the time with the same period of z(t), so that it can be expressed in form of the Fourier series:

$$\begin{aligned} \sigma(t) &= \sum_{n=-\infty}^{\infty} \sigma_n e^{in\Omega t} = \\ &= \sum_{n=-\infty}^{\infty} s_n e^{i\phi_n} e^{in\Omega t} \end{aligned} \tag{C.9}$$

where σ_n is the generic complex Fourier coefficient of σ with modulus s_n and phase ϕ_n.
Let us consider the voltage signal ΔV, expressed by the equation 4.20. Since its dependence on the time occurs through S and τ, which are both even periodic functions of the time, then ΔV can be written as Fourier series:

$$\Delta V(t) = \sum_{n=-\infty}^{\infty} \Delta V_n e^{in\Omega t} \tag{C.10}$$

where ΔV_n are the harmonics of the signal. Let us show first that σ_n are complex quantities, while ΔV_n are real quantities. Using the definition of Fourier coefficients and considering tha $\sigma(t)$ is even:

$$\begin{aligned} \sigma_n &= \frac{1}{T}\int_{-\frac{T}{2}}^{\frac{T}{2}} \sigma(t) e^{-in\Omega t} dt = \\ &= \frac{1}{T}\int_{-\frac{T}{2}}^{\frac{T}{2}} \sigma(t) cos\left(n\Omega t\right) dt + i\frac{1}{T}\int_{-\frac{T}{2}}^{\frac{T}{2}} \sigma(t) sin\left(n\Omega t\right) dt = \\ &= \frac{1}{T}\int_{-\frac{T}{2}}^{\frac{T}{2}} \sigma(t) cos\left(n\Omega t\right) dt \end{aligned} \tag{C.11}$$

Since the scattering coefficient is complex, then also σ_n are complex-valued and we can write them separating modulus and phase. Similarly we can write:

$$\Delta V_n = \frac{1}{T}\int_{-\frac{T}{2}}^{\frac{T}{2}} \Delta V(t) cos\left(n\Omega t\right) dt \tag{C.12}$$

$\Delta V(t)$ is a real-valued function, therefore also the harmonics ΔV_n are real. At this point we want to find an equation linking ΔV_n and σ_n. Let us substitute into the scaled LK field equation 4.14 the expression of $\sigma(t)$ in form of the Fourier series given by the Equation C.9. We can write:

$$\frac{d\widetilde{E}(t)}{dt} = \frac{1}{2\tau_p}\left[\frac{1}{2}(1+i\alpha)\left(\widetilde{N}-1\right)\widetilde{E} + V\sum_{n=-\infty}^{\infty} s_n e^{i\phi_n} e^{in\Omega t}\widetilde{E}(t-\tau)e^{-i\omega_0\tau}\right] \quad \text{(C.13)}$$

Writing explicitly modulus and phase of the scaled field we have:

$$\frac{d\widetilde{E}_0(t)}{dt}e^{i\widetilde{\Phi}(t)} + \widetilde{E}_0(t)i\frac{d\widetilde{\Phi}(t)}{dt}e^{i\widetilde{\Phi}(t)} = \frac{1}{2\tau_p}\left[(1+i\alpha)\left(\widetilde{N}-1\right)\widetilde{E}_0(t)e^{i\widetilde{\Phi}(t)}\right] + \\ + \frac{V}{2\tau_p}\sum_{n=-\infty}^{\infty} s_n e^{i\phi_n} e^{in\Omega t}\widetilde{E}_0(t-\tau)e^{\widetilde{\Phi}(t-\tau)-i\omega_0\tau} \quad \text{(C.14)}$$

We can then separate the last complex equation in two real equations:

$$\begin{aligned}\frac{d\widetilde{E}_0(t)}{dt} &= \frac{1}{2\tau_p}\left[\left(\widetilde{N}-1\right)\widetilde{E}_0(t)\right] + \\ &+ \frac{V}{2\tau_p}\sum_{n=-\infty}^{\infty} s_n\widetilde{E}_0(t-\tau)cos\left[\widetilde{\Phi}(t-\tau)-\omega_0\tau+\phi_n+n\Omega t-\widetilde{\Phi}(t)\right]\end{aligned} \quad \text{(C.15)}$$

$$\begin{aligned}\frac{d\widetilde{\Phi}_0(t)}{dt} &= \frac{1}{2\tau_p}\left[\alpha\left(\widetilde{N}-1\right)\right] + \\ &+ \frac{V}{2\tau_p}\sum_{n=-\infty}^{\infty} s_n\frac{\widetilde{E}_0(t-\tau)}{\widetilde{E}_0(t)}sin\left[\widetilde{\Phi}(t-\tau)-\omega_0\tau+\phi_n+n\Omega t-\widetilde{\Phi}(t)\right]\end{aligned} \quad \text{(C.16)}$$

Imposing the steady-state conditions $\widetilde{E}(t)$=$\widetilde{E}(t-\tau)$=$\widetilde{E}_s$, $\widetilde{\Phi}(t)$=(ω_F-ω_0)t and $\widetilde{N}(t)$=$\widetilde{N}_s$ we have:

$$0 = \frac{1}{2}(\widetilde{N}_s-1) + \frac{V}{2}\sum_{n=-\infty}^{\infty} s_n cos\left(\omega_F\tau-\phi_n-\Omega_n t\right) \quad \text{(C.17)}$$

Imposing 1-$\widetilde{N}_s$=ΔV we obtain:

$$\Delta V = V\sum_{n=-\infty}^{\infty} s_n cos\left(\omega_F\tau-\phi_n-\Omega_n t\right) \quad \text{(C.18)}$$

where Ω_n=nΩt. Using the approximated equation $\omega_F \approx \omega_0$ valid in the very weak feedback regime we have:

$$\Delta V = V\sum_{n=-\infty}^{\infty} s_n cos\left(\omega_0\tau-\phi_n-\Omega_n t\right) \quad \text{(C.19)}$$

As ΔV is an even function, it can be straightforwardly shown that s_n=s_{-n} and ϕ_n=ϕ_{-n}. Therefore we can write:

$$\begin{aligned}
\Delta V &= V\sum_{n=-\infty}^{\infty} s_n cos\left(\omega_0\tau - \phi_n - \Omega_n t\right) = \\
&= V\left[s_0 cos\left(\omega_0\tau - \phi_0\right) + \sum_{n=1}^{\infty} s_n cos\left(\omega_0\tau - \phi_n - \Omega_n t\right) + s_{-n} cos\left(\omega_0\tau - \phi_{-n} - \Omega_{-n} t\right)\right] = \\
&= V\left[s_0 cos\left(\omega_0\tau - \phi_0\right) + \sum_{n=1}^{\infty} s_n cos\left(\omega_0\tau - \phi_n - \Omega_n t\right) + s_n cos\left(\omega_0\tau - \phi_n + \Omega_n t\right)\right] = \\
&= V\left[s_0 cos\left(\omega_0\tau - \phi_0\right) + 2\sum_{n=1}^{\infty} s_n cos\left(\omega_0\tau - \phi_n\right) cos\left(\Omega_n t\right)\right] \qquad \text{(C.20)}
\end{aligned}$$

Let us consider again the equation C.10 and, remembering that ΔV is an even function of the the time, we can straightforwardly rewrite it as:

$$\Delta V = V\left[\Delta V_0 + 2\sum_{n=1}^{\infty} \Delta V_n cos\left(\Omega_n t\right)\right] \qquad \text{(C.21)}$$

Comparing equations C.10 and C.21 we find that:

$$\Delta V_n = V s_n cos\left(\omega_0\tau - \phi_n\right) \qquad \text{(C.22)}$$

for n=0,1,2,... Equation C.22 links the harmonics of the signal ΔV to modulus and phase of the Fourier coefficients of the scattering coefficient σ. ΔV_n are quantities directly measurable through the lock-in amplifier present in each s-SNOM configuration, therefore we want to express s_n and ϕ_n as functions of the harmonics of one or more sets of detected signals, so that the information about optical properties of the material sample can be easily retrievable by exploiting experimentally measurable quantities.
By following a similar procedure developed in the previous subsection, we introduce the variation ΔL of the laser-tip distance L causing a phase shift ΔΦ into the Eq. C.22. For a phase shift $\Delta\Phi=\frac{\pi}{2}$, we can write:

$$(\Delta V_n)_{\frac{\pi}{2}} = -V s_n sin\left(\omega_0\tau - \phi_n\right) \qquad \text{(C.23)}$$

where $(\Delta V_n)_{\frac{\pi}{2}}$ is the $\frac{\pi}{2}$-shifted generic signal harmonic. Considering equation C.20 it can be straightforwardly shown that $(\Delta V_n)_{\frac{\pi}{2}}$=$(\Delta V_{\frac{\pi}{2}})_n$. We can now easily retrieve explicit expressions of s_n and ϕ_n, manipulating equations C.22 and C.23. We find:

$$s_n = \frac{1}{V}\sqrt{(\Delta V_n)^2 + (\Delta V_{\frac{\pi}{2}})_n{}^2} \qquad \text{(C.24)}$$

$$\phi_n = \omega_0\tau + atan\left[\frac{(\Delta V_{\frac{\pi}{2}})_n}{\Delta V_n}\right] \qquad \text{(C.25)}$$

Equations C.24 and C.25 provide a simple methode to obtain the harmonics of the scattering coefficient by measuring the harmonics of two signals, which are performed by varying the laser-tip distance by $\frac{\lambda}{8}$ to obtain the $\frac{\pi}{2}$ shift. These formulas are valid for a SD s-SNOM configuration, characterized by a complex scattering coefficient in the modelization through LK equations, in the very weak regime, and they are based on the assumptions of sinusoidal interferometric fringes and negligible perturbation of the emission frequency due to the feedback.

Appendix D

Theoretical Study of the Weak Regime

In Appendix D we have studied the LK model and its steady state solutions by exploiting a zero-order approximation of the so called phase excess equation, by assuming negligible the effect of the feedback in the very weak regime. We want to consider now the weak regime, characterized by a value of the parameter C of 10^{-1} order of magnitude. In this case the assumption of negligible feedback is not valid anymore and the interferometric fringes are not sinusoidal curves. Therefore the phase excess equation can not be approximated at zero order, but it needs also a definition of first order terms. In order to retrieve the correct equations in the weak regime we will exploit a theory based on Taylor expansions, which will conduct us to retrieve also approximated expression of the scattering coefficient in agreement with the hypotheses of the weak regime. The derivation presented in this Appendix has been developed in [62].

D.1 Approximated steady-state solutions of the Lang-Kobayashi model in the weak regime

Let us consider the Eqs. 4.20 and 4.22, i.e. the steady-state solutions of the LK model with the complex scattering coefficient σ inserted into the expression of $\widetilde{k}$. The coupling between these equations (ω_F appears into the argument of cosine present in the equation 4.20) and the fact that Eq. 4.22 is an implicit function of ω_F, make the retrieval of the the solutions of the system a complicated mathematical problem. We solve this problem by finding approximated solutions. In fact the theoretical study presented in this subsection is the derivation of approximated expressions of ω_F and ΔV using the hypothesis of operative weak feedback regime. In this regime it is reasonably possible to assume ϵ small, where ϵ is defined by the equation 4.23. Taylor series expansions are our tool in order to obtain an explicit

expression of ω_F, which we want to insert then into the signal equation and have also an explicit expression of ΔV. Being in the weak regime allows us to consider a monodromic behaviour for the laser frequency, as we already mentioned in the previous part of this chapter.
Let us assume this expression for the laser frequency modified by the feedback:

$$\omega_F\tau \approx \omega_0\tau + \epsilon\omega_1\tau + \epsilon^2\omega_2\tau \tag{D.1}$$

ω_1 and ω_2 are respectively the first and second order corrections to the solitary laser freq ω_0, due to the feedback in the equation D.1. We next substitute this expression of $\omega_F\tau$ into the phase excess equation, obtaining:

$$\omega_0\tau + \epsilon\omega_1\tau + \epsilon^2\omega_2\tau = \omega_0\tau - \epsilon S\sqrt{1+\alpha^2}sin(\omega_0\tau + \epsilon\omega_1\tau + \epsilon^2\omega_2\tau + \widetilde{\beta} - \phi) \tag{D.2}$$

where $\widetilde{\beta}$=atan(α). Then, simplifying:

$$\epsilon\omega_1\tau + \epsilon^2\omega_2\tau = -\epsilon S\sqrt{1+\alpha^2}sin(\omega_0\tau + \epsilon\omega_1\tau + \epsilon^2\omega_2\tau + \widetilde{\beta} - \phi) \tag{D.3}$$

Let us define:

$$\Phi_0 = \omega_0\tau - \phi \tag{D.4}$$
$$\Phi_0' = \omega_0\tau - \phi + \widetilde{\beta} \tag{D.5}$$

Introducing the definition D.5, using the trigonometric angle sum identity for sine and Taylor expansion for sine we have:

$$\begin{aligned}
\epsilon\omega_1\tau + \epsilon^2\omega_2\tau &= -\epsilon S\sqrt{1+\alpha^2}sin(\Phi_0' + \epsilon\omega_1\tau + \epsilon^2\omega_2\tau) = \\
&= -\epsilon S\sqrt{1+\alpha^2}\left[sin\Phi_0'cos(\epsilon\omega_1\tau + \epsilon^2\omega_2\tau) + cos\Phi_0'sin(\epsilon\omega_1\tau + \epsilon^2\omega_2\tau)\right] = \\
&\approx -\epsilon S\sqrt{1+\alpha^2}sin\Phi_0'(1 - \frac{1}{2}\epsilon^2(\omega_1\tau + \epsilon\omega_2\tau)^2) + \\
&- \epsilon S\sqrt{1+\alpha^2}cos\Phi_0'(\epsilon\omega_1\tau + \epsilon^2\omega_2\tau) = \\
&= -\epsilon S\sqrt{1+\alpha^2}sin\Phi_0' - S\sqrt{1+\alpha^2}\epsilon^2cos(\Phi_0')\omega_1\tau
\end{aligned} \tag{D.6}$$

Therefore, we obtain the first order and second order coefficients :

$$\omega_1\tau = -S\sqrt{1+\alpha^2}sin(\Phi_0') \tag{D.7}$$
$$\begin{aligned}\omega_2\tau &= -S\sqrt{1+\alpha^2}cos(\Phi_0')\omega_1\tau = \\ &= S^2(1+\alpha^2)sin(\Phi_0')cos(\Phi_0')\end{aligned} \tag{D.8}$$

We can finally write the approximated expression of $\omega_F\tau$ in the weak regime:

$$\omega_F\tau = \omega_0\tau - \epsilon S\sqrt{1+\alpha^2}sin(\Phi_0 + \widetilde{\beta}) + \epsilon^2S^2(1+\alpha^2)sin(\Phi_0 + \widetilde{\beta})cos(\Phi_0 + \widetilde{\beta}) \tag{D.9}$$

At this point we want to write the approximated expression of ΔV. First let us define:

$$S' = S\sqrt{1+\alpha^2} \tag{D.10}$$

Substituting the equation D.9 into the equation 4.20, using the trigonometric angle sum identities and the second-order Taylor expansions for sine and cosine, we have:

$$\begin{aligned}
\Delta V &= VScos\left[\Phi_0 - \epsilon S' sin(\Phi_0') + \epsilon^2 S^2(1+\alpha^2) sin(\Phi_0')cos(\Phi_0')\right] = \\
&= VS\{cos\Phi_0 cos\left[\epsilon(S' sin(\Phi_0') - \epsilon S'^2 sin(\Phi_0')cos(\Phi_0')\right] + \\
&+ sin\Phi_0 sin\left[\epsilon(S' sin(\Phi_0') - \epsilon S'^2 sin(\Phi_0')cos(\Phi_0')\right]\} = \\
&= VScos\Phi_0\left[1 - \frac{1}{2}(\epsilon(S' sin(\Phi_0') - \epsilon S'^2 sin(\Phi_0')cos(\Phi_0'))^2\right] + \\
&+ VSsin\Phi_0\left[\epsilon\left(S' sin(\Phi_0') - \epsilon S'^2 sin(\Phi_0')cos(\Phi_0')\right)\right] = \\
&= VScos\Phi_0 - \frac{1}{2}VScos\Phi_0\epsilon^2 S'^2 sin^2\Phi_0' + \\
&+ VSsin\Phi_0\epsilon S' sin\Phi_0' - VSsin\Phi_0\epsilon^2 S'^2 sin\Phi_0' cos\Phi_0'
\end{aligned} \tag{D.11}$$

We finally obtain the approximated expression of ΔV:

$$\Delta V = VS\{cos\Phi_0 + \epsilon S' sin\Phi_0 sin\Phi_0' - \epsilon^2 S'^2 sin\Phi_0'\left[\frac{1}{2}cos\Phi_0 sin\Phi_0' + sin\Phi_0 cos\Phi_0'\right]\} \tag{D.12}$$

Equation D.12 is the approximated expression of ΔV that we were looking for, in order to start for the mathematical treatment that will be presented in next sections, aimed to retrieve approximated expressions for modulus S and phase ϕ of the scattering coefficient σ in the weak feedback regime.

D.2 Retrieval of the scattering coefficient

In this section we derive and present a first order reconstruction for the scattering coefficient σ in the weak feedback regime. We remind that σ contains the information about the optical properties of the analyzed sample, so that the retrieval of this quantity allows us to determine them. Since the weak regime is characterized by a higher Signal to Noise Ratio compared with the very weak, the possibility to obtain these properties in this regime is relevant from the experimental point of view.
Let us consider the equation D.12. It is a second order approximated expression of the signal ΔV. Since we want to find a first order expression for modulus and phase of the scattering coefficient, we neglect the term in ϵ^2 in D.12, obtaining:

$$\Delta V = VS\{cos\Phi_0 + \epsilon S\sqrt{1+\alpha^2} sin\Phi_0 sin(\Phi_0 + \widetilde{\beta})\} \tag{D.13}$$

In the very weak regime we considered a shift of the quantity Φ_0, that can be experimentally introduced by changing the laser-tip distance L, according to the equation D.5 and the dependence of τ from L. In this case we want to introduce three specific values of shift for Φ_0: $\frac{\pi}{2}$, π and $\frac{3\pi}{2}$. By inserting these shift into Eq. D.13 we have:

$$\Delta V_{\frac{\pi}{2}} = VS\{-sin\Phi_0 + \epsilon S\sqrt{1+\alpha^2}cos\Phi_0 cos(\Phi_0 + \widetilde{\beta})\} \tag{D.14}$$

$$\Delta V_{\pi} = VS\{-cos\Phi_0 + \epsilon S\sqrt{1+\alpha^2}sin\Phi_0 sin(\Phi_0 + \widetilde{\beta})\} \tag{D.15}$$

$$\Delta V_{\frac{3\pi}{2}} = VS\{sin\Phi_0 + \epsilon S\sqrt{1+\alpha^2}cos\Phi_0 cos(\Phi_0 + \widetilde{\beta})\} \tag{D.16}$$

Starting from Eqs. D.13, D.14, D.15, D.16 we look for explicit expressions for S and ϕ. Let us consider the following differences:

$$\Delta V - \Delta V_{\pi} = 2VScos(\omega_0\tau - \phi) \tag{D.17}$$

$$\Delta V_{\frac{3\pi}{2}} - \Delta V_{\frac{\pi}{2}} = 2VSsin(\omega_0\tau - \phi) \tag{D.18}$$

Using the fundamental trigonometric identity we can straightforwardly retrieve an explicit expression for S:

$$S = \frac{1}{2V}\sqrt{(\Delta V - \Delta V_{\pi})^2 + \left(\Delta V_{\frac{3\pi}{2}} - \Delta V_{\frac{\pi}{2}}\right)^2} \tag{D.19}$$

Furthermore, dividing the equations D.17 and D.18 an expression of ϕ is found:

$$\phi = \omega_0\tau - atan\left(\frac{\Delta V_{\frac{3\pi}{2}} - \Delta V_{\frac{\pi}{2}}}{\Delta V - \Delta V_{\pi}}\right) \tag{D.20}$$

Equations D.19 and D.20 are first order reconstruction formulas for the modulus and phase of the scattering coefficient in the weak regime. Four signals in four different experimental configurations(i.e. four different values of the laser-tip distance) are needed to implement a retrieval of σ by using these formulas.

D.3 Retrieval of the scattering coefficient harmonics

As we mentioned in the section related to the very weak regime, the quantities that it is experimentally possible to retrieve with a SD s-SNOM setup are the signal harmonics. Therefore, in order to obtain the optical properties of a given material sample, we want to find approximated equations, valid in the weak feedback regime, that link modulus s_n and phase ϕ_n of the Fourier coefficients of σ with the harmonics of the signal. In the section C.2 we already found expressions for these quantities based on zero order approximation $\omega_F \approx \omega_0$. Here we want to find an extension to

the first order in ϵ.
Let us begin from the Eqs. C.15 and C.16. In this mathematical approach we assume that the oscillation frequency of the tip is Ω, so that we can write the scattering coefficient according to the Eq. C.9. We remind that we already inserted the steady-state conditions into the Eq. C.15 and we obtained the Eq. C.18, where the signal ΔV is expressed as a series.
At this point let us consider Eq. C.16 and let us use the steady state conditions $\widetilde{E}(t)=\widetilde{E}(t-\tau)=\widetilde{E}_s$, $\widetilde{\Phi}(t)=(\omega_F\text{-}\omega_0)$t and $\widetilde{N}(t)=\widetilde{N}_s$. We get:

$$\omega_F-\omega_0 = \frac{1}{2\tau_p}\left[\alpha\left(\widetilde{N}_s-1\right)-V\sum_{n=-\infty}^{\infty}s_n sin\left[\omega_F\tau-n\Omega t-\phi_n\right]\right] \quad (D.21)$$

By using the definition of ΔV and substituting Eq. C.18 into the previous equation we have:

$$\begin{aligned}\omega_F-\omega_0 &= -\frac{V}{2\tau_p}\{\alpha\sum_{n=-\infty}^{\infty}s_n cos\left[\omega_F\tau-n\Omega t-\phi_n\right]+\\ &+\sum_{n=-\infty}^{\infty}s_n sin\left[\omega_F\tau-n\Omega t-\phi_n\right]\}\end{aligned} \quad (D.22)$$

Multiplying by τ this equation and writing explicitly the expression V, we obtain:

$$\begin{aligned}\omega_F\tau &= \omega_0\tau-\frac{\tau}{\tau_c}\widetilde{a}\left(\frac{1-R}{\sqrt{R}}\right)\{\alpha\sum_{n=-\infty}^{\infty}s_n cos\left[\omega_F\tau-n\Omega t-\phi_n\right]+\\ &+\sum_{n=-\infty}^{\infty}s_n sin\left[\omega_F\tau-n\Omega t-\phi_n\right]\}\end{aligned} \quad (D.23)$$

Remembering the definition of ϵ given by Eq. 4.23 we rewrite as:

$$\begin{aligned}\omega_F\tau &= \omega_0\tau-\epsilon\{\alpha\sum_{n=-\infty}^{\infty}s_n cos\left[\omega_F\tau-n\Omega t-\phi_n\right]+\\ &+\sum_{n=-\infty}^{\infty}s_n sin\left[\omega_F\tau-n\Omega t-\phi_n\right]\}\end{aligned} \quad (D.24)$$

Using the definition of $\widetilde{\beta}$ the last equation can be straightforwardly written as:

$$\begin{aligned}\omega_F\tau &= \omega_0\tau-\epsilon\sqrt{1+\alpha^2}\{\sum_{n=-\infty}^{\infty}s_n cos(\widetilde{\beta})cos\left[\omega_F\tau-n\Omega t-\phi_n\right]+\\ &+\sum_{n=-\infty}^{\infty}s_n sin(\widetilde{\beta})sin\left[\omega_F\tau-n\Omega t-\phi_n\right]\}\end{aligned} \quad (D.25)$$

Using standard trigonometry we finally have:

$$\omega_F\tau = \omega_0\tau-\epsilon\sqrt{1+\alpha^2}\sum_{n=-\infty}^{\infty}s_n sin\left[\omega_F\tau-n\Omega t-\phi_n+\widetilde{\beta}\right] \quad (D.26)$$

This is an implicit equation with ω_F as unknown. Similarly to the previous section, we assume this expression for ω_F:

$$\omega_F \tau \approx \omega_0 \tau + \epsilon \widetilde{\omega}_1 \tau + \epsilon^2 \widetilde{\omega}_2 \tau \tag{D.27}$$

At this point we want to determine the first order and second order coefficients. Substituting Eq. D.27 into the Eq. D.26 we have:

$$\epsilon \widetilde{\omega}_1 \tau + \epsilon^2 \widetilde{\omega}_2 \tau = -\epsilon \sqrt{1+\alpha^2} \sum_{n=-\infty}^{\infty} s_n sin\left[\Phi_n + \epsilon \widetilde{\omega}_1 \tau + \epsilon^2 \widetilde{\omega}_2 \tau + \widetilde{\beta}\right] \tag{D.28}$$

where Φ_n is defined as:

$$\Phi_n = \omega_0 \tau - n\Omega t - \phi_n \tag{D.29}$$

Using the sum identity for the sine function and the second order Taylor expansion for sine and cosine we can write:

$$\begin{aligned}
\epsilon \widetilde{\omega}_1 \tau + \epsilon^2 \widetilde{\omega}_2 \tau &= -\epsilon \sqrt{1+\alpha^2} \sum_{n=-\infty}^{\infty} s_n \{sin(\Phi_n + \widetilde{\beta}) cos(\epsilon \widetilde{\omega}_1 \tau + \epsilon^2 \widetilde{\omega}_2 \tau) + \\
&+ cos(\Phi_n + \widetilde{\beta}) sin(\epsilon \widetilde{\omega}_1 \tau + \epsilon^2 \widetilde{\omega}_2 \tau)\} \approx \\
&\approx -\epsilon \sqrt{1+\alpha^2} \sum_{n=-\infty}^{\infty} s_n \{sin(\Phi_n + \widetilde{\beta})(1 - \frac{\epsilon^2}{2} \widetilde{\omega}_1^2 \tau^2) + \\
&+ cos(\Phi_n + \widetilde{\beta})(\epsilon \widetilde{\omega}_1 \tau + \epsilon^2 \widetilde{\omega}_2 \tau)\} \approx \\
&\approx -\epsilon \sqrt{1+\alpha^2} \sum_{n=-\infty}^{\infty} s_n \{sin(\Phi_n + \widetilde{\beta}) + \epsilon \widetilde{\omega}_1 \tau cos(\Phi_n + \widetilde{\beta})\} = \\
&= \epsilon \left[-\sqrt{1+\alpha^2} \sum_{n=-\infty}^{\infty} s_n sin(\Phi_n + \widetilde{\beta})\right] + \\
&+ \epsilon^2 \left[-\sqrt{1+\alpha^2} \widetilde{\omega}_1 \tau \sum_{n=-\infty}^{\infty} s_n cos(\Phi_n + \widetilde{\beta})\right]
\end{aligned} \tag{D.30}$$

We find then the expressions for the first order and second order coefficients:

$$\widetilde{\omega}_1 \tau = -\sqrt{1+\alpha^2} \sum_{n=-\infty}^{\infty} s_n sin(\Phi_n + \widetilde{\beta}) \tag{D.31}$$

$$\widetilde{\omega}_2 \tau = (1+\alpha^2) \sum_{n=-\infty}^{\infty} \sum_{m=-\infty}^{\infty} s_n s_m sin(\Phi_n + \widetilde{\beta}) cos(\Phi_m + \widetilde{\beta}) \tag{D.32}$$

It is evident that the correction at first order appears quite manageable, while the second one is more involved. For the rest of this derivation, we will assume a first order approximation and apply Eq. D.31 in the expansion D.27 of ω_F to derive simple analytical results for the hamonics of S and ϕ:

$$\omega_F \tau = \omega_0 \tau - \sqrt{1+\alpha^2} \sum_{n=-\infty}^{\infty} s_n sin(\Phi_n + \widetilde{\beta}) \tag{D.33}$$

We substitute it into the signal equation C.18 obtaining:

$$\begin{aligned}
\Delta V &= V\sum_{n=-\infty}^{\infty} s_n cos\left[\omega_0\tau - n\Omega t - \phi - \epsilon\sqrt{1+\alpha^2}\sum_{m=-\infty}^{\infty} s_m sin(\Phi_m + \widetilde{\beta})\right] = \\
&= V\sum_{n=-\infty}^{\infty} s_n cos\left[\Phi_n - \epsilon\sqrt{1+\alpha^2}\sum_{m=-\infty}^{\infty} s_m sin(\Phi_m + \widetilde{\beta})\right] = \\
&= V\sum_{n=-\infty}^{\infty} s_n\{cos\Phi_n cos(\epsilon\sqrt{1+\alpha^2}\sum_{m=-\infty}^{\infty} s_m sin(\Phi_m + \widetilde{\beta})) + \\
&+ sin\Phi_n sin(\epsilon\sqrt{1+\alpha^2}\sum_{m=-\infty}^{\infty} s_m sin(\Phi_m + \widetilde{\beta}))\} \approx \\
&\approx V\sum_{n=-\infty}^{\infty} s_n\{cos\Phi_n + sin\Phi_n\epsilon\sqrt{1+\alpha^2}\sum_{m=-\infty}^{\infty} s_m sin(\Phi_m + \widetilde{\beta})\} \qquad \text{(D.34)}
\end{aligned}$$

Similarly to the last section we can introduce a proper shift of the quantity Φ_n. For the particular values of shift $\frac{\pi}{2}$, π and $\frac{3\pi}{2}$ we have:

$$\Delta V_{\frac{\pi}{2}} = V\sum_{n=-\infty}^{\infty} s_n\{-sin\Phi_n + cos\Phi_n\epsilon\sqrt{1+\alpha^2}\sum_{m=-\infty}^{\infty} s_m cos(\Phi_m + \widetilde{\beta})\} \qquad \text{(D.35)}$$

$$\Delta V_{\pi} = V\sum_{n=-\infty}^{\infty} s_n\{-cos\Phi_n + sin\Phi_n\epsilon\sqrt{1+\alpha^2}\sum_{m=-\infty}^{\infty} s_m sin(\Phi_m + \widetilde{\beta})\} \qquad \text{(D.36)}$$

$$\Delta V_{\frac{\pi}{2}} = V\sum_{n=-\infty}^{\infty} s_n\{sin\Phi_n + cos\Phi_n\epsilon\sqrt{1+\alpha^2}\sum_{m=-\infty}^{\infty} s_m cos(\Phi_m + \widetilde{\beta})\} \qquad \text{(D.37)}$$

We want to calculate the difference between ΔV and ΔV_{π}, therefore we have:

$$\begin{aligned}
\Delta V - \Delta V_{\pi} &= 2V\sum_{n=-\infty}^{\infty} s_n cos\Phi_n = \\
&= Vs_0 cos(\omega_0\tau - \phi_0) + 2V\sum_{n=1}^{\infty} s_n cos(\omega_0\tau - \phi_n)cos(n\Omega t) \qquad \text{(D.38)}
\end{aligned}$$

We used the analytical property of ΔV, which is an even function. Then we can explicitly write the generic Fourier coefficient of the difference $\Delta V - \Delta V_{\pi}$:

$$(\Delta V - \Delta V_{\pi})_n = 2Vs_n cos(\omega_0\tau - \phi_n) \qquad \text{(D.39)}$$

Furthermore let us consider the the difference between $\Delta V_{\frac{3\pi}{2}}$ and $\Delta V_{\frac{\pi}{2}}$:

$$\begin{aligned}
\Delta V_{\frac{3\pi}{2}} - \Delta V_{\frac{\pi}{2}} &= 2V\sum_{n=-\infty}^{\infty} s_n sin\Phi_n = \\
&= Vs_0 sin(\omega_0\tau - \phi_0) + 2V\sum_{n=1}^{\infty} s_n sin(\omega_0\tau - \phi_n)cos(n\Omega t) \qquad \text{(D.40)}
\end{aligned}$$

Then we can write:

$$(\Delta V_{\frac{3\pi}{2}} - \Delta V_{\frac{\pi}{2}})_n = 2\,V s_n sin(\omega_0 \tau - \phi_n) \tag{D.41}$$

At this point we can easily retrieve an explicit expression for s_n and ϕ_n, manipulating the Eqs, D.39 and D.41:

$$s_n = \frac{1}{2\,V}\sqrt{((\Delta V_{\frac{3\pi}{2}} - \Delta V_{\frac{\pi}{2}})_n)^2 + ((\Delta V - \Delta V_\pi)_n)^2} \tag{D.42}$$

$$\phi_n = \omega_0 \tau - atan\left[\frac{(\Delta V_{\frac{3\pi}{2}} - \Delta V_{\frac{\pi}{2}})_n}{(\Delta V - \Delta V_\pi)_n}\right] \tag{D.43}$$

Using the property of linearity of the integrals we obtain:

$$s_n = \frac{1}{2\,V}\sqrt{((\Delta V_{\frac{3\pi}{2}})_n - (\Delta V_{\frac{\pi}{2}})_n)^2 + (\Delta V_n - (\Delta V_\pi)_n)^2} \tag{D.44}$$

$$\phi_n = \omega_0 \tau - atan\left[\frac{(\Delta V_{\frac{3\pi}{2}})_n - (\Delta V_{\frac{\pi}{2}})_n}{\Delta V_n - (\Delta V_\pi)_n}\right] \tag{D.45}$$

These formulas allow to retrieve the Fourier coefficients of σ in the weak regime, by using experimental measures of the harmonics of four signals, which is possible with a lock-in amplifier provided by every s-SNON setup. We can apply these formulas directly to experimental data, as it will be shown in the next part of this chapter. Furthermore it can be noticed that the Eqs. D.44 and D.45 have the same mathematical structure of the Eqs. D.19 and D.20, that relate the scattering coefficient to four signal measurement. Therefore in the first order approximation the relation linking s_n and ϕ_n with the harmonics of four signals is the same relation linking S and ϕ with the four considered signals.

Bibliography

[1] G. P. Agrawal. "Line narrowing in a single-mode injection laser due to external optical feedback". In: *IEEE Journal of Quantum Electronics* 20 (May 1984), pp. 468–471. DOI: 10.1109/JQE.1984.1072420.

[2] GEORGE ARFKEN. "14 - FOURIER SERIES". In: *Mathematical Methods for Physicists (Third Edition)*. Ed. by GEORGE ARFKEN. Third Edition. Academic Press, 1985, pp. 760–793. ISBN: 978-0-12-059820-5. DOI: https://doi.org/10.1016/B978-0-12-059820-5.50022-7. URL: https://www.sciencedirect.com/science/article/pii/B9780120598205500227.

[3] Paolo Bardella, Lorenzo Luigi Columbo, and Mariangela Gioannini. "Self-generation of optical frequency comb in single section quantum dot Fabry-Perot lasers: a theoretical study". In: *Opt. Express* 25.21 (Oct. 2017), pp. 26234–26252. DOI: 10.1364/OE.25.026234. URL: http://www.osapublishing.org/oe/abstract.cfm?URI=oe-25-21-26234.

[4] S. Bartalini et al. "Observing the Intrinsic Linewidth of a Quantum-Cascade Laser: Beyond the Schawlow-Townes Limit". In: *Phys. Rev. Lett.* 104 (8 Feb. 2010), p. 083904. DOI: 10.1103/PhysRevLett.104.083904. URL: https://link.aps.org/doi/10.1103/PhysRevLett.104.083904.

[5] Mattias Beck et al. "Continuous Wave Operation of a Mid-Infrared Semiconductor Laser at Room Temperature". In: *Science* 295.5553 (2002), pp. 301–305. DOI: 10.1126/science.1066408. eprint: https://www.science.org/doi/pdf/10.1126/science.1066408. URL: https://www.science.org/doi/abs/10.1126/science.1066408.

[6] Karl Bertling et al. "New Applications of THz Waves in Precision Agriculture". In: (2021).

[7] David Burghoff. "Unraveling the origin of frequency modulated combs using active cavity mean-field theory". In: *Optica* 7.12 (Dec. 2020), pp. 1781–1787. DOI: 10.1364/OPTICA.408917. URL: http://www.osapublishing.org/optica/abstract.cfm?URI=optica-7-12-1781.

[8] David Burghoff et al. "Evaluating the coherence and time-domain profile of quantum cascade laser frequency combs". In: *Opt. Express* 23.2 (Jan. 2015), pp. 1190–1202.

[9] Larry A. Coldren and Scott W. Corzine. *Semiconductor and Photonic Integrated Circuits*. John Wiley & Sons, Ltd, 1995.

[10] Daniel C. Cole et al. "Theory of Kerr frequency combs in Fabry-Perot resonators". In: *Phys. Rev. A* 98 (1 July 2018), p. 013831. DOI: 10.1103/PhysRevA.98.013831. URL: https://link.aps.org/doi/10.1103/PhysRevA.98.013831.

[11] Daniel C. Cole et al. "Theory of Kerr frequency combs in Fabry-Perot resonators". In: *Phys. Rev. A* 98 (1 July 2018), p. 013831. DOI: 10.1103/PhysRevA.98.013831. URL: https://link.aps.org/doi/10.1103/PhysRevA.98.013831.

[12] L. Columbo et al. "Unifying Frequency Combs in Active and Passive Cavities: Temporal Solitons in Externally Driven Ring Lasers". In: *Phys. Rev. Lett.* 126 (17 Apr. 2021), p. 173903. DOI: 10.1103/PhysRevLett.126.173903. URL: https://link.aps.org/doi/10.1103/PhysRevLett.126.173903.

[13] L. L. Columbo et al. "Dynamics of a broad-band quantum cascade laser: from chaos to coherent dynamics and mode-locking". In: *Opt. Express* 26.3 (Feb. 2018), pp. 2829–2847. DOI: 10.1364/OE.26.002829. URL: http://www.osapublishing.org/oe/abstract.cfm?URI=oe-26-3-2829.

[14] Luigi Consolino et al. "Quantum cascade laser based hybrid dual comb spectrometer". In: *Communications Physics* 3 (1 2020). DOI: 10.1038/s42005-020-0344-0.

[15] Nicola Corrias et al. "Analog FM free-space optical communication based on a mid-infrared quantum cascade laser frequency comb". In: *Opt. Express* 30.7 (Mar. 2022), pp. 10217–10228. DOI: 10.1364/OE.443483. URL: http://opg.optica.org/oe/abstract.cfm?URI=oe-30-7-10217.

[16] S.M. Cox and P.C. Matthews. "Exponential Time Differencing for Stiff Systems". In: *Journal of Computational Physics* 176.2 (2002), pp. 430–455. ISSN: 0021-9991. DOI: https://doi.org/10.1006/jcph.2002.6995. URL: https://www.sciencedirect.com/science/article/pii/S0021999102969950.

[17] J. Faist. "Singlemode quantum cascade lasers with power dissipation below 1W". English. In: *Electronics Letters* 48 (11 May 2012), 646–647(1). ISSN: 0013-5194. URL: https://digital-library.theiet.org/content/journals/10.1049/el.2012.1204.

[18] Jerome Faist et al. "Quantum Cascade Laser". In: *Science* 264.5158 (1994), pp. 553–556. DOI: 10.1126/science.264.5158.553. eprint: https://www.science.org/doi/pdf/10.1126/science.264.5158.553. URL: https://www.science.org/doi/abs/10.1126/science.264.5158.553.

[19] Jérôme Faist et al. "Quantum Cascade Laser Frequency Combs". In: *Nanophotonics* 5.2 (2016), pp. 272–291.

[20] Peter Friedli et al. “Four-wave mixing in a quantum cascade laser amplifier”. In: *Applied Physics Letters* 102.22 (2013), p. 222104. DOI: 10.1063/1.4807662. eprint: https://doi.org/10.1063/1.4807662. URL: https://doi.org/10.1063/1.4807662.

[21] Maria C. Giordano et al. “Phase-resolved terahertz self-detection near-field microscopy”. In: *Opt. Express* 26.14 (July 2018), pp. 18423–18435. DOI: 10.1364/OE.26.018423. URL: http://www.osapublishing.org/oe/abstract.cfm?URI=oe-26-14-18423.

[22] Guido Giuliani et al. “Laser diode self-mixing technique for sensing applications”. In: *Journal of Optics A: Pure and Applied Optics* 4.6 (Nov. 2002), S283–S294. DOI: 10.1088/1464-4258/4/6/371. URL: https://doi.org/10.1088/1464-4258/4/6/371.

[23] Ariel Gordon et al. “Multimode regimes in quantum cascade lasers: From coherent instabilities to spatial hole burning”. In: *Phys. Rev. A* 77 (5 May 2008), p. 053804. DOI: 10.1103/PhysRevA.77.053804. URL: https://link.aps.org/doi/10.1103/PhysRevA.77.053804.

[24] Richard P. Green et al. “Linewidth enhancement factor of terahertz quantum cascade lasers”. In: *Applied Physics Letters* 92.7 (2008), p. 071106. DOI: 10.1063/1.2883950. eprint: https://doi.org/10.1063/1.2883950. URL: https://doi.org/10.1063/1.2883950.

[25] Xiao Guo, Karl Bertling, and Aleksandar D. Rakić. “Optical constants from scattering-type scanning near-field optical microscope”. In: *Applied Physics Letters* 118.4 (2021), p. 041103. DOI: 10.1063/5.0036872. eprint: https://doi.org/10.1063/5.0036872. URL: https://doi.org/10.1063/5.0036872.

[26] C. Henry. “Theory of the linewidth of semiconductor lasers”. In: *IEEE Journal of Quantum Electronics* 18.2 (1982), pp. 259–264. DOI: 10.1109/JQE.1982.1071522.

[27] Nathan Henry et al. “Study of Spatio-Temporal Character of Frequency Combs Generated by Quantum Cascade Lasers”. In: *IEEE Journal of Selected Topics in Quantum Electronics* 25.6 (2019), pp. 1–9. DOI: 10.1109/JSTQE.2019.2929222.

[28] Nathan Henry et al. “Temporal characteristics of quantum cascade laser frequency modulated combs in long wave infrared and THz regions”. In: *Opt. Express* 26.11 (May 2018), pp. 14201–14212. DOI: 10.1364/OE.26.014201. URL: http://www.osapublishing.org/oe/abstract.cfm?URI=oe-26-11-14201.

[29] Andreas Hugi et al. “Mid-infrared frequency comb based on a quantum cascade laser”. In: *Nature* 492.1 (Dec. 2012), pp. 229–233.

[30] M. Jaidl et al. “Comb operation in terahertz quantum cascade ring lasers”. In: *Optica* 8.6 (June 2021), pp. 780–787. DOI: 10.1364/OPTICA.420674. URL: http://www.osapublishing.org/optica/abstract.cfm?URI=optica-8-6-780.

[31] Deborah M. Kane and K. Alan Shore, eds. *Unlocking Dynamical Diversity: Optical Feedback Effects on Semiconductor Lasers*. English. United States: John Wiley Sons, Dec. 2005. ISBN: 047085619X. DOI: 10.1002/0470856211.

[32] Dmitry Kazakov et al. “Defect-engineered ring laser harmonic frequency combs”. In: *Optica* 8.10 (Oct. 2021), pp. 1277–1280. DOI: 10.1364/OPTICA.430896. URL: http://www.osapublishing.org/optica/abstract.cfm?URI=optica-8-10-1277.

[33] J. B. Khurgin et al. “Coherent frequency combs produced by self frequency modulation in quantum cascade lasers”. In: *Applied Physics Letters* 104.8 (2014), p. 081118. DOI: 10.1063/1.4866868. eprint: https://doi.org/10.1063/1.4866868. URL: https://doi.org/10.1063/1.4866868.

[34] Tobias J. Kippenberg et al. “Dissipative Kerr solitons in optical microresonators”. In: *Science* 361.6402 (2018), eaan8083. DOI: 10.1126/science.aan8083. eprint: https://www.science.org/doi/pdf/10.1126/science.aan8083. URL: https://www.science.org/doi/abs/10.1126/science.aan8083.

[35] Russell Kliese et al. “Solving self-mixing equations for arbitrary feedback levels: a concise algorithm”. In: *Appl. Opt.* 53.17 (June 2014), pp. 3723–3736. DOI: 10.1364/AO.53.003723. URL: http://www.osapublishing.org/ao/abstract.cfm?URI=ao-53-17-3723.

[36] R. Lang and K. Kobayashi. “External optical feedback effects on semiconductor injection laser properties”. In: *IEEE Journal of Quantum Electronics* 16.3 (1980), pp. 347–355. DOI: 10.1109/JQE.1980.1070479.

[37] Hua Li et al. “Dynamics of ultra-broadband terahertz quantum cascade lasers for comb operation”. In: *Opt. Express* 23.26 (Dec. 2015), pp. 33270–33294.

[38] Luigi Lugiato, Franco Prati, and Massimo Brambilla. *Nonlinear Optical Systems*. Cambridge University Press, 2015. DOI: 10.1017/CBO9781107477254.

[39] Luigi A Lugiato and Franco Prati. “Traveling wave formalism for the dynamics of optical systems in nonlinear Fabry–Perot cavities”. In: 93.12 (Oct. 2018), p. 124001. DOI: 10.1088/1402-4896/aadec2. URL: https://doi.org/10.1088/1402-4896/aadec2.

[40] W. Maineult et al. “Microwave modulation of terahertz quantum cascade lasers: a transmission-line approach”. In: *Applied Physics Letters* 96.2 (2010), p. 021108. DOI: 10.1063/1.3284518. eprint: https://doi.org/10.1063/1.3284518. URL: https://doi.org/10.1063/1.3284518.

[41] R. Martini and E. A. Whittaker. "Quantum cascade laser-based free space optical communications". In: *Free-Space Laser Communications: Principles and Advances*. New York, NY: Springer New York, 2008, pp. 393–406. ISBN: 978-0-387-28677-8. DOI: 10.1007/978-0-387-28677-8_9. URL: https://doi.org/10.1007/978-0-387-28677-8_9.

[42] Bo Meng et al. "Dissipative Kerr solitons in semiconductor ring lasers". In: *Nature Photonics* 16 (2 2022), pp. 142–147. DOI: 10.1038/s41566-021-00927-3. URL: https://doi.org/10.1038/s41566-021-00927-3.

[43] Bo Meng et al. "Mid-infrared frequency comb from a ring quantum cascade laser". In: *Optica* 7.2 (Feb. 2020), pp. 162–167. DOI: 10.1364/OPTICA.377755. URL: http://www.osapublishing.org/optica/abstract.cfm?URI=optica-7-2-162.

[44] Francesco P. Mezzapesa et al. "Tunable and compact dispersion compensation of broadband THz quantum cascade laser frequency combs". In: *Opt. Express* 27.15 (July 2019), pp. 20231–20240. DOI: 10.1364/OE.27.020231. URL: http://www.osapublishing.org/oe/abstract.cfm?URI=oe-27-15-20231.

[45] Francesco P. Mezzapesa et al. "Tunable and compact dispersion compensation of broadband THz quantum cascade laser frequency combs". In: *Opt. Express* 27.15 (July 2019), pp. 20231–20240. DOI: 10.1364/OE.27.020231. URL: http://www.osapublishing.org/oe/abstract.cfm?URI=oe-27-15-20231.

[46] E. Mujagić et al. "Low divergence single-mode surface emitting quantum cascade ring lasers". In: *Applied Physics Letters* 93.16 (2008), p. 161101. DOI: 10.1063/1.3000630. eprint: https://doi.org/10.1063/1.3000630. URL: https://doi.org/10.1063/1.3000630.

[47] Opacak Nikola and Schwarz Benedikt. "Theory of Frequency-Modulated Combs in Lasers with Spatial Hole Burning, Dispersion, and Kerr Nonlinearity". In: *Phys. Rev. Lett.* 123 (24 Dec. 2019), p. 243902. DOI: 10.1103/PhysRevLett.123.243902. URL: https://link.aps.org/doi/10.1103/PhysRevLett.123.243902.

[48] N. Ocelic. *Quantitative Near-field Phonon-polariton Spectroscopy*. Doctoral Thesis, 2007.

[49] Marco Piccardo and Federico Capasso. "Laser Frequency Combs with Fast Gain Recovery: Physics and Applications". In: *Laser & Photonics Reviews* 16.2 (2022), p. 2100403. DOI: https://doi.org/10.1002/lpor.202100403. eprint: https://onlinelibrary.wiley.com/doi/pdf/10.1002/lpor.202100403. URL: https://onlinelibrary.wiley.com/doi/abs/10.1002/lpor.202100403.

[50] Marco Piccardo et al. "Frequency combs induced by phase turbulence". In: *Nature* 582 (2020), p. 360. DOI: 10.1038/s41586-020-2386-6. URL: https://doi.org/10.1038/s41586-020-2386-6.

[51] Marco Piccardo et al. "Nonlinear Dynamics in Semiconductor Ring Lasers: From Phase Turbulence to Solitons". In: *2021 Conference on Lasers and Electro-Optics Europe and European Quantum Electronics Conference*. Optica Publishing Group, 2021, ef_{25}. URL: http://opg.optica.org/abstract.cfm?URI=EQEC-2021-ef_2_5.

[52] Marco Piccardo et al. "Time-dependent population inversion gratings in laser frequency combs". In: *Optica* 5.4 (Apr. 2018), pp. 475–478.

[53] Marco Piccardo et al. "Widely tunable harmonic frequency comb in a quantum cascade laser". In: *Applied Physics Letters* 113 (July 2018), p. 031104. DOI: 10.1063/1.5039611.

[54] Eva A. A. Pogna et al. "Terahertz near-field nanoscopy based on detectorless laser feedback interferometry under different feedback regimes". In: *APL Photonics* 6.6 (2021), p. 061302. DOI: 10.1063/5.0048099. eprint: https://doi.org/10.1063/5.0048099. URL: https://doi.org/10.1063/5.0048099.

[55] Eva A. A. Pogna et al. "Terahertz Near-field Nanoscopy Based on Self-mixing Interferometry with Quantum Cascade Resonators". In: *2021 Conference on Lasers and Electro-Optics Europe European Quantum Electronics Conference (CLEO/Europe-EQEC)*. 2021, pp. 1–1. DOI: 10.1109/CLEO/Europe-EQEC52157.2021.9542282.

[56] F. Prati et al. "Global and localised temporal structures in driven ring quantum cascade lasers". In: *Chaos, Solitons Fractals* 153 (2021), p. 111537. ISSN: 0960-0779. DOI: https://doi.org/10.1016/j.chaos.2021.111537. URL: https://www.sciencedirect.com/science/article/pii/S0960077921008912.

[57] Franco Prati et al. "Soliton dynamics of ring quantum cascade lasers with injected signal". In: *Frontiers in Optics and Photonics*. Ed. by Federico Capasso and Dennis Couwenberg. De Gruyter, 2021, pp. 197–210. DOI: doi:10.1515/9783110710687-018. URL: https://doi.org/10.1515/9783110710687-018.

[58] Michele De Regis et al. "Terahertz frequency metrology". In: *Terahertz Emitters, Receivers, and Applications X*. Ed. by Manijeh Razeghi, Alexei N. Baranov, and Miriam S. Vitiello. Vol. 11124. International Society for Optics and Photonics. SPIE, 2019, pp. 58–67. DOI: 10.1117/12.2529347. URL: https://doi.org/10.1117/12.2529347.

[59] D. G. Revin et al. “Active mode locking of quantum cascade lasers in an external ring cavity”. In: *Nature Communications* 7 (2013), p. 231102. DOI: 10.1038/ncomms11440. eprint: https://doi.org/10.1038/ncomms11440. URL: https://doi.org/10.1038/ncomms11440.

[60] H. Risken and K. Nummedal. “Self-Pulsing in Lasers”. In: *Journal of Applied Physics* 39.10 (1968), pp. 4662–4672. DOI: 10.1063/1.1655817. eprint: https://doi.org/10.1063/1.1655817. URL: https://doi.org/10.1063/1.1655817.

[61] Markus Rösch et al. “Heterogeneous terahertz quantum cascade lasers exceeding 1.9 THz spectral bandwidth and featuring dual comb operation”. In: *Nanophotonics* 7.1 (2018), pp. 237–242.

[62] Carlo Silvestri. *Study of resonant materials’ optical properties via THz near eld optical microscopy and self-mixing interferometry*. Master of Science Thesis, Università degli Studi di Bari, 2018.

[63] Carlo Silvestri et al. “Coherent multi-mode dynamics in a quantum cascade laser: amplitude- and frequency-modulated optical frequency combs”. In: *Opt. Express* 28.16 (Aug. 2020), pp. 23846–23861. DOI: 10.1364/OE.396481. URL: http://www.osapublishing.org/oe/abstract.cfm?URI=oe-28-16-23846.

[64] Carlo Silvestri et al. “Dynamics of Optical Frequency Combs in Ring and Fabry-Perot Quantum Cascade Lasers”. In: *2021 Conference on Lasers and Electro-Optics Europe European Quantum Electronics Conference (CLEO/Europe-EQEC)*. 2021, pp. 1–1. DOI: 10.1109/CLEO/Europe-EQEC52157.2021.9541633.

[65] Matthew Singleton et al. “Evidence of linear chirp in mid-infrared quantum cascade lasers”. In: *Optica* 5.8 (Aug. 2018), pp. 948–953.

[66] Olivier Spitz et al. “Free-Space Communication With Directly Modulated Mid-Infrared Quantum Cascade Devices”. In: *IEEE Journal of Selected Topics in Quantum Electronics* 28.1 (2022), pp. 1–9. DOI: 10.1109/JSTQE.2021.3096316.

[67] Olivier Spitz et al. “Private communication with quantum cascade laser photonic chaos”. In: *Nature Communications* 12 (1 June 2021). DOI: 10.1038/s41467-021-23527-9. URL: https://doi.org/10.1038/s41467-021-23527-9.

[68] Jens von Staden et al. “Measurements of the α factor of a distributed-feedback quantum cascade laser by an optical feedback self-mixing technique”. In: *Opt. Lett.* 31.17 (Sept. 2006), pp. 2574–2576. DOI: 10.1364/OL.31.002574. URL: http://opg.optica.org/ol/abstract.cfm?URI=ol-31-17-2574.

[69] Stefan Stanciu et al. “Towards imaging skin cancer by apertureless scanning near-field optical microscopy”. In: *University Politehnica of Bucharest Scientific Bulletin-Series A-Applied Mathematics and Physics* 78 (2 2016), pp. 235–244.

[70] Thomas Taimre et al. “Laser feedback interferometry: a tutorial on the self-mixing effect for coherent sensing”. In: *Adv. Opt. Photon.* 7.3 (Sept. 2015), pp. 570–631. DOI: 10.1364/AOP.7.000570. URL: http://www.osapublishing.org/aop/abstract.cfm?URI=aop-7-3-570.

[71] Petar Tzenov et al. “Time domain modeling of terahertz quantum cascade lasers for frequency comb generation”. In: *Opt. Express* 24.20 (Oct. 2016), pp. 23232–23247. DOI: 10.1364/OE.24.023232. URL: http://www.osapublishing.org/oe/abstract.cfm?URI=oe-24-20-23232.

[72] Gustavo Villares and Jérôme Faist. “Quantum cascade laser combs: effects of modulation and dispersion”. In: *Opt. Express* 23.2 (Jan. 2015), pp. 1651–1669. DOI: 10.1364/OE.23.001651. URL: http://www.osapublishing.org/oe/abstract.cfm?URI=oe-23-2-1651.

[73] Gustavo Villares et al. “Dispersion engineering of quantum cascade laser frequency combs”. In: *Optica* 3.3 (Mar. 2016), pp. 252–258. DOI: 10.1364/OPTICA.3.000252. URL: http://www.osapublishing.org/optica/abstract.cfm?URI=optica-3-3-252.

[74] Miriam S. Vitiello et al. “Quantum-limited frequency fluctuations in a terahertz laser”. In: *Nature Photonics* 6.8 (2012), pp. 525–528. DOI: 10.1038/nphoton.2012.145.

[75] Miriam S. Vitiello et al. “Toward new frontiers for terahertz quantum cascade laser frequency combs”. In: *Nanophotonics* 10.1 (2021), pp. 187–194. DOI: doi:10.1515/nanoph-2020-0429. URL: https://doi.org/10.1515/nanoph-2020-0429.

[76] Miriam Serena Vitiello and Paolo De Natale. “Terahertz Quantum Cascade Lasers as Enabling Quantum Technology”. In: *Advanced Quantum Technologies* 5.1 (2022), p. 2100082. DOI: https://doi.org/10.1002/qute.202100082. eprint: https://onlinelibrary.wiley.com/doi/pdf/10.1002/qute.202100082. URL: https://onlinelibrary.wiley.com/doi/abs/10.1002/qute.202100082.

[77] Miriam Serena Vitiello et al. “Quantum cascade lasers: 20 years of challenges”. In: *Opt. Express* 23.4 (Feb. 2015), pp. 5167–5182. DOI: 10.1364/OE.23.005167. URL: http://opg.optica.org/oe/abstract.cfm?URI=oe-23-4-5167.

[78] N. Vukovic et al. “Analytical expression for Risken-Nummedal-Graham-Haken instability threshold in quantum cascade lasers”. In: *Opt. Express* 24.23 (Nov. 2016), pp. 26911–26929. DOI: 10.1364/OE.24.026911. URL: http://www.osapublishing.org/oe/abstract.cfm?URI=oe-24-23-26911.

[79] Christine Y. Wang et al. “Mode-locked pulses from mid-infrared Quantum Cascade Lasers”. In: *Opt. Express* 17.15 (July 2009), pp. 12929–12943. DOI: 10.1364/OE.17.012929. URL: http://www.osapublishing.org/oe/abstract.cfm?URI=oe-17-15-12929.

[80] Yongrui Wang and Alexey Belyanin. “Active mode-locking of mid-infrared quantum cascade lasers with short gain recovery time”. In: *Opt. Express* 23.4 (Feb. 2015), pp. 4173–4185. DOI: 10.1364/OE.23.004173. URL: http://www.osapublishing.org/oe/abstract.cfm?URI=oe-23-4-4173.

[81] M. Wienold et al. “Evidence for frequency comb emission from a Fabry-Pérot terahertz quantum-cascade laser”. In: *Opt. Express* 22.25 (Dec. 2014), pp. 30410–30424.

[82] Aleksander K. Wójcik et al. “Generation of picosecond pulses and frequency combs in actively mode locked external ring cavity quantum cascade lasers”. In: *Applied Physics Letters* 103.23 (2013), p. 231102. DOI: 10.1063/1.4838275. eprint: https://doi.org/10.1063/1.4838275. URL: https://doi.org/10.1063/1.4838275.

[83] Masamichi Yamanishi et al. “Theory of the Intrinsic Linewidth of Quantum-Cascade Lasers: Hidden Reason for the Narrow Linewidth and Line-Broadening by Thermal Photons”. In: *IEEE Journal of Quantum Electronics* 44.1 (2008), pp. 12–29. DOI: 10.1109/JQE.2007.907563.

This Ph.D. thesis has been typeset by means of the TEX-system facilities. The typesetting engine was pdfLATEX. The document class was `toptesi`, by Claudio Beccari, with option `tipotesi=scudo`. This class is available in every up-to-date and complete TEX-system installation.